論文 / 著書情報
Article / Book Information

題目(和文)	多孔質内における混和性流体の重力不安定対流の三次元フィンガー構造
Title(English)	Three-dimensional fingering structure of gravitationally unstable convection between miscible fluids in a porous medium
著者(和文)	Wang Lei
Author(English)	Lei Wang
出典(和文)	学位:博士(工学), 学位授与機関:東京工業大学, 報告番号:甲第10852号, 授与年月日:2018年3月26日, 学位の種別:課程博士, 審査員:末包 哲也,奥野 喜裕,岡村 哲至,長﨑 孝夫,肖 鋒
Citation(English)	Degree:Doctor (Engineering), Conferring organization: Tokyo Institute of Technology, Report number:甲第10852号, Conferred date:2018/3/26, Degree Type:Course doctor, Examiner:,,,,
学位種別(和文)	博士論文
Type(English)	Doctoral Thesis

Three-dimensional fingering structure of gravitationally unstable convection between miscible fluids in a porous medium

Lei WANG

A dissertation

submitted to the Department of Energy Sciences

and the committee of graduate studies of Tokyo Institute of Technology

in partial fulfillment of the requirements for the degree of Doctor of Engineering

Supervisor: Prof. Tetsuya SUEKANE

March 2018

Contents

Abstract 1

Chapter 1: Introduction 1
1.1 General information of geological storage of CO_2 1
1.1.1 Modes of CO_2 storage formation 2
1.1.2 Trapping mechanism 3
1.1.3 Global geological storage of CO_2 5
1.2 CO_2 dissolved into deep saline formation 6
1.3 CO_2 in Enhanced Oil Recovery 8
1.4 Research objectives 11

Chapter 2: Miscible fluids with nonlinear density property modelling density-driven convection 13
2.1 Design of the laboratory experiments 14
2.1.1 Miscible fluid pair with nonlinear density property 15
2.1.2 Particle properties 16
2.2 Measurement and Image processing 17

Chapter 3: Three-dimensional fingering structure of density-driven natural convection 19
3.1 Experimental setup and procedures 19
3.2 Development of convective fingers 20
3.3 Finger-extension velocity 21
3.4 Finger-number density 22
3.5 Effect of dispersion on the fingering structure 26
3.6 Mass flux 32
3.7 Summary 35

Chapter 4: Effect of layered heterogeneity on fingering structure 37
4.1 Experimental setup and procedures 37
4.2 Changing of fingering structure at different permeability layers 38
4.3 Finger-extension velocity 40

4.5 Summary 44

Chapter 5: Gravitational fingering due to density increase by mixing at a vertical displacing 45

5.1 Experimental method 45

5.2 Three-dimensional finger structure during injection process 48

5.3 Finger-extension velocity 49

5.4 Distribution of NaI concentration in fingers 50

5.5 Mixing layer 55

5.6 Finger-number density 57

5.7 Mixing length 58

5.8 Evolution of the relative volume V of the mixing fingers 61

5.9 Dispersion 63

5.10 Summary 64

Chapter 6: Conclusions and outlook 66

6.1 Conclusions 66

6.2 Outlook 68

References 70

Acknowledgements 81

Appendix 83

Abstract

The storage of carbon dioxide (CO_2) in geological formations has attracted increasing attention because it represents one of the most promising solutions for reducing greenhouse gas emissions. CO_2 dissolves into saline formations or oil, creating a gravitationally unstable layer due to density increase and leads to convective mixing that promotes stable long-term storage or improves oil recovery.

In this work, the three-dimensional fingering structure of gravitationally unstable convective flows in a porous medium was investigated using a micro-focused X-ray computer tomography (CT). A miscible fluid pair with nonlinear density properties (a sodium chloride solution and a mixture of methanol and ethylene glycol doped with sodium iodide) was used to model the density increase from mixing upon CO_2 injection into the reservoir. A series of laboratory experiments with different combinations of Rayleigh number and Péclet number have been carried out in a porous medium.

In density-driven natural convection, slight fluctuations that appeared at the interface grew into large "fingers," which interacted and merged with the neighboring fingers. The fingers extended vertically downward without changing their locations, forming a columnar structure. The finger-extension velocity increased in line with the Rayleigh number. The three-dimensional images captured the local concentration of fingers in the course of convective mixing. It is found that the decrease in finger-number density was not only related to the Rayleigh number but was also affected by transverse dispersion between the downward- and upward-flow regions. Transverse dispersion caused broadening of the fingers and reduction in the finger-number density because of the interaction and merging of fingers. The mass transfer rate was related to Rayleigh number following the power law relationship. Additionally, the layered heterogeneous structure hinders the development of natural convection.

During the displacement process, with increasing Péclet number, the density difference between the downward-moving fingers and upward-moving surroundings increased, resulting in increases of the finger extension velocity and the velocity of the upward flow. Furthermore, the mixing near the interface became stronger. Over time, the mixing length and relative volume of the fingers increased. The growth of the mixing length of the fingers was proportional to time with a smaller slope at early times and switched to a larger slope growth at later times. A rapid increase of the relative volume of fingers was observed with increasing Péclet number. In the fingers, the local NaI concentration

decreased linearly and the initial interface traveled downward as a result of the enhanced interaction of the fingers during the injection process. The enhanced dispersion with increasing Péclet number affected the broadening of the fingers and reduced the finger number density.

In CO_2 geological storage applications, the transverse dispersion influences the long-term-dissolution process of CO_2 injected into aquifers. The investigation of the effect of the injection process on the fingering structure provides insights into the mixing mechanism and recovery performance of CO_2 injection into oil reservoirs.

Nomenclature

U	Darcy velocity, $U = \Delta\rho g k / \mu$ (m/s)
U^*	Dimensionless Darcy velocity
P	Pressure (Pa)
P^*	Dimensionless pressure
$\vec{z}$	A unit vector pointing in the direction of gravity
C	NaI concentration (kg/m^3)
C^*	Dimensionless concentration
C_w	Average concentration of NaI (kg/m^3)
Ra	Rayleigh number, $Ra = (\Delta\rho g k H)/(\varphi\mu D_m)$
Ra_c	Critical Rayleigh number
k	Permeability (m^2)
φ	Porosity
ρ	Density (kg/m^3)
μ	Viscosity of NaCl solution (mPa·s)
$\Delta\rho$	Typical density difference between two miscible fluids (g/cm^3)
$\Delta\rho'$	Initial density difference between MEG-NaI and NaCl solutions (g/cm^3)
g	Gravitational acceleration (m^2/s)
H	Height of porous media (m)
h_0	Deformation of the interface (m)
D_m	Diffusivity of iodide ions (m^2/s)
d_p	Average particle diameter (μm)
v	Finger extension velocity (m/s)
v_D	Velocity of downward-moving fingers, $v_D = v$ (m/s)
v_U	Velocity of upward-moving plumes (m/s)
v_m	Velocity of horizontal flows (m/s)
v_0	Injection speed (m/s)
c	Coefficient
N	Finger number density (/cm^2)
N_m	Maximum Finger number density (/cm^2)
z	Distance from the initial interface (mm)
z'	Distance of the travelling interface (mm), $z' = (v_0/\varphi)t$
z_f	Position of the maximum finger-number density (mm)
t	Time (s)
t^*	Dimensionless time, $t^* = tU/H$

c_0	Coefficient
r	Radius of the finger (mm)
R	Radius of the packed bed (mm)
D_T	Transverse dispersion coefficient (m^2/s)
V	Control volume
S	The end surface area of the control volume (m^2), $S = \pi r_f^2$
S'	The side area of the control volume, (m^2), $S' = 2\pi r_f$
r_f	The radius of the control volume (mm)
Pe	Péclet number, $Pe = (v_0 d_p)/(\varphi D_m)$
Pe^*	Péclet number, $Pe^* = (v d_p)/(\varphi D_m)$
α	Decay coefficient (s^{-1})
F	Mass flux ($mg/s \cdot m^2$)
Sh	Sherwood number, $Sh = F/(\varphi \Delta c D_m/H)$
Δc	Concentration difference of iodide between MEG-NaI mixture and NaCl solution (Δc = 110 kg/m^3)
λ_c	Critical wavelength (m)
c_f	NaI concentration in downward fingers (kg/m^3)
c_s	Solubility of CO_2 in brine (kg/m^3)
A_D	Area of fingers (m^2)
A_U	Area of NaCl flows (m^2)
δ_m	Thickness of the mixing layer (mm)
P_i	Perimeter of the fingers (mm)
n	Number of fingers
l_m	Mixing length (mm)
V	Relative volume of fingers (%)
σ	Growth rate of relative volume of fingers (/s)

Chapter 1: Introduction

Carbon dioxide (CO_2) Capture and Storage (CCS) is defined as a systematic process that integrates three stages: CO_2 capture, transport and geologic storage. It has been proposed as one of the key technologies for dealing with the adverse effects of climate change. CCS offers a tangible means to deal with large volumes of CO_2 emissions securely and cost-effectively.

International Energy Agency (IEA) has report that CCS is estimated to contribute 14% of total emissions reductions through 2050 needed to progress from the 6 degree scenario to the 2 degree scenario (IEA, 2014). The Intergovernmental Panel on Climate Change (IPCC) considers that CCS will provide 15 % to 55 % of the cumulative mitigation effort up to 2100 (IPCC, 2005). CCS is also an important part of the lowest-cost greenhouse gas mitigation portfolio. The overall cost to achieve a 50 % reduction in CO_2 emissions by 2050 will increase by 70 % without CCS (IEA, 2009).

CO_2 Geological storage is a key part in the whole CCS process because of the large capacity of CO_2 storage, which make a significant contribution to emissions reduction.

1.1 General information of geological storage of CO_2

The challenge of CO_2 geological storage projects is to separate CO_2 at a low cost and continuously isolate safely and securely over the long term. To geologically store CO_2, it is injected into the pore space of rocks deep in the Earth's subsurface, at depths typically greater than 1000 metres. The density of CO_2 will increase with injection depth until at about 800 m or greater, the injected CO_2 will be in a dense supercritical state. Supercritical CO_2 takes up much less space than gases, as shown in Fig. 1-1. Its volume would be dramatically reduced from 100 m^3 at the surface to only 0.27 m^3 at 2500 m depth. This is one of the factors that makes the geological storage of large quantities of CO_2 attractive.

After CO_2 is injected into a reservoir, supercritical CO_2 of density 600–700 kg/m^3 (lighter than ambient groundwater) will rise because of buoyancy until it encounters an impermeable rock and is structurally trapped beneath it (Arts et al., 2008). The potential risk of CO_2 leakage because of buoyancy could degrade the quality of groundwater, damage some mineral resources, and have lethal effects on plants and subsoil animals. Therefore, the safety of CO_2 geological storage is of prime importance in dealing with carbon sequestration on a large scale.

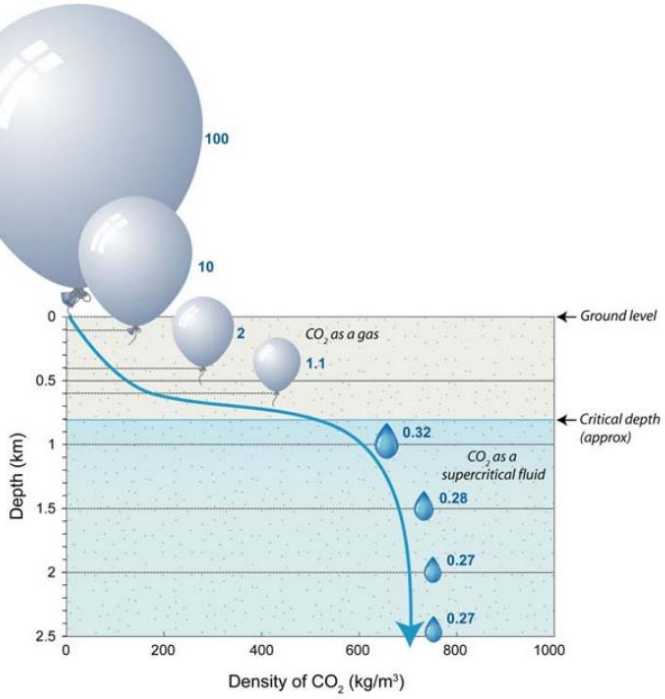

Fig. 1-1. CO_2-density and volume as a function of depth
Image Source: CO_2CRC

1.1.1 Modes of CO_2 storage formation

Geological storage of CO_2 can be undertaken in a variety of geological settings in sedimentary basins, including depleted oil and gas fields, deep saline formations and deep unmineable coal seams (Fig. 1-2).

Depleted reservoirs provide one of the most readily available storage solutions. In some cases, the injected CO_2 could give rise to a greater oil or natural gas production. This practice is known as Enhanced Oil Recovery (EOR) or Enhanced Gas Recovery (EGR). CO_2 has been used for EOR for decades, with an increase in oil recovery by 7 % - 23 % of the original oil in place. In other cases, the CO_2 may be injected into the pores of rocks where the oil or gas has been already produced, which is eventually retained within the reservoir.

Deep saline formation offers promising storage opportunities due to their wider regional coverage and potential proximity to CO_2 capture sites. Injected CO_2 adds to fluid already trapped in the pore spaces, then dissolves in the saline water, and extends downward by convection because of the density increase. Deep saline formations contain most of the global geologic storage capacity and are available for the long-term and safe CO_2 geological storage.

Deep unmineable coal seams are also possible sites. Injected CO_2 is to a large extent adsorbed to the coal matrix, preferentially replacing methane molecules. This type production is called Enhanced Coal Bed Methane. However, the chemical reactions and physical processes could occur during CO_2 injection into coal seams, and their impact on the integrity of the coal seams, which are not well understood.

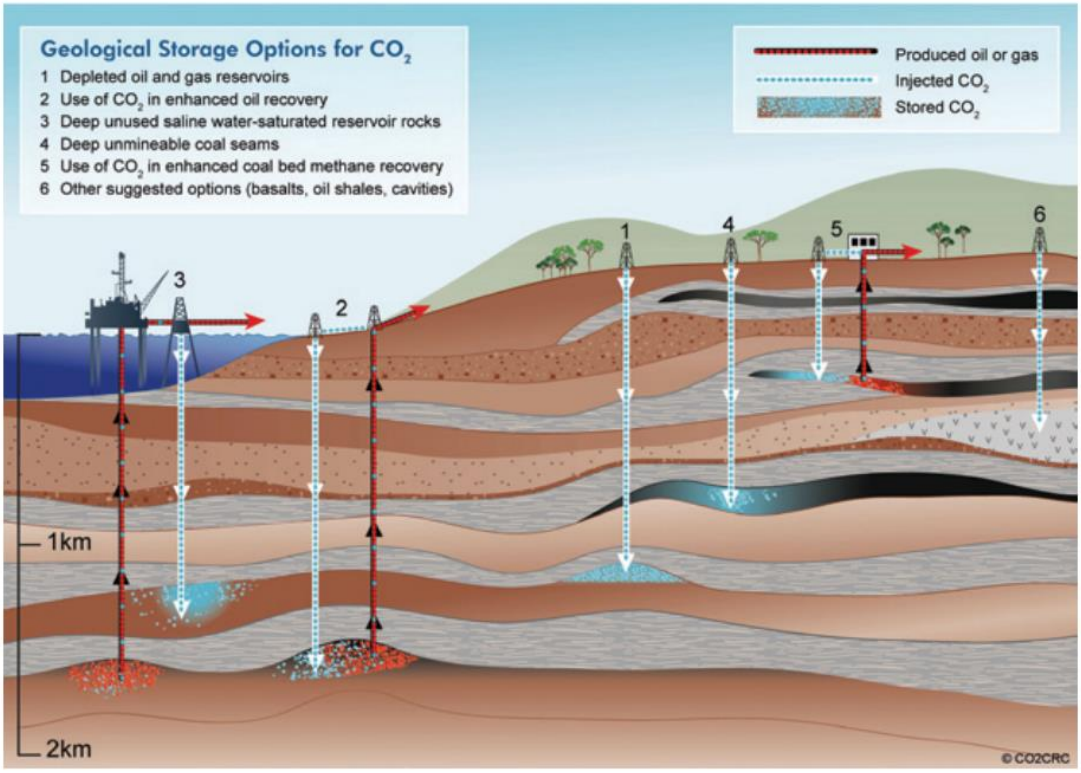

Fig. 1-2. Different kinds of geological formations suitable for geological storage of CO_2
Image Source: IPCC special report on carbon dioxide capture and storage (2005)

1.1.2 Trapping mechanism

There are four kinds of trapping mechanism (Huppert & Neufeld, 2014) that retained the injected CO_2 in reservoir, namely (a) structural or stratigraphic trapping, (b) capillary trapping (Bandara et al., 2011; Chaudhary et al., 2013; Jiang & Tsuji, 2016;Iglauer, 2011; Li et al., 2014; Pentland et al. 2011; Suekane at al., 2008; Taku Ide et al., 2007), (c) solubility trapping (Gilfillan et al., 2009; Iglauer, 2011; Erik Lindeberg & Wessel-Berg, 1997; E Lindeberg & Begmo, 2003; Riaz & Cinar, 2014) and (d) mineral trapping (Gaus, 2010; Klein et al., 2013; Xu et al., 2017) (Fig. 1-3). As time goes on, the physical process of residual CO_2 trapping decrease and the geochemical process of solubility trapping and mineral trapping increase (Fig. 1-4).

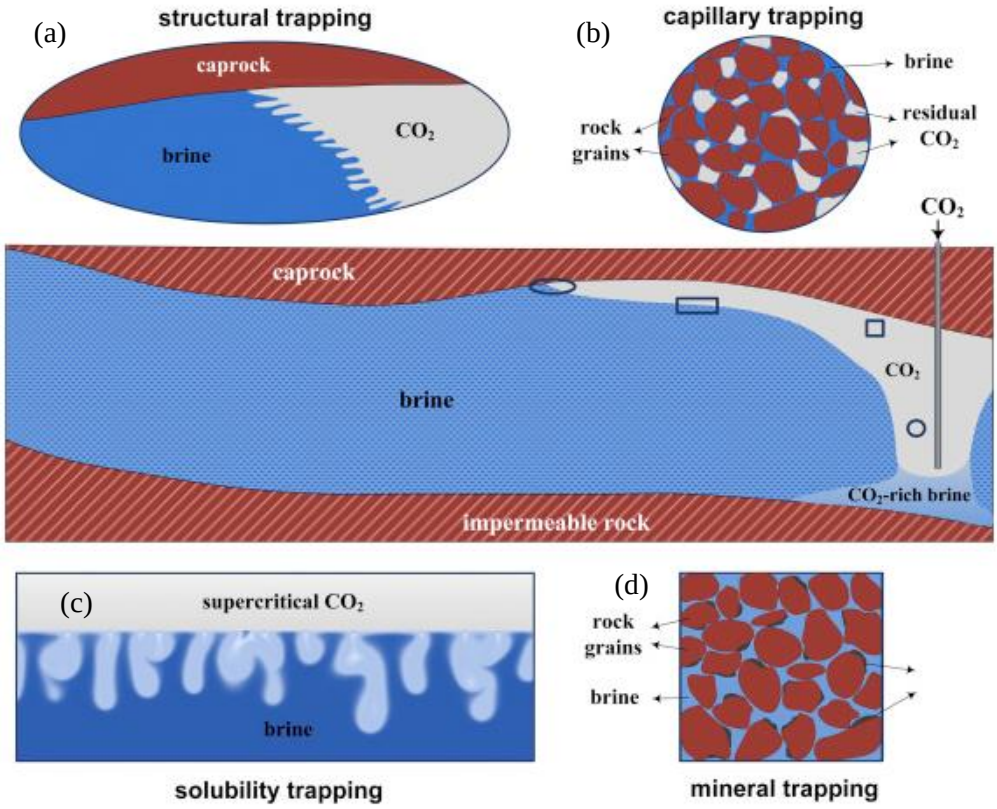

Fig. 1-3. Trapping mechanism

Source: Emami-Meybodi,et al., 2015

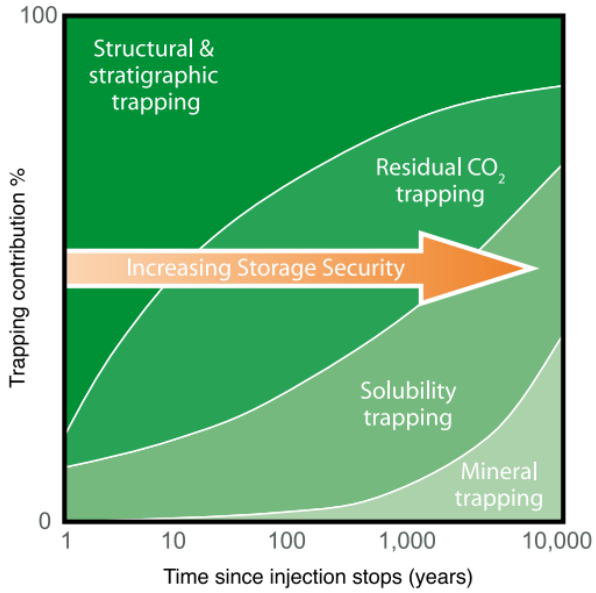

Fig. 1-4. Storage security depends on the combination of physical and geochemical trapping.

Image Source: IPCC special report on carbon dioxide capture and storage (2005)

Structural and stratigraphic trapping is shown in Fig. 1-3 (a). When CO_2 is injected into a reservoir, it displaces saline formation water and fills the rock's pore spaces. Then, supercritical CO_2 migrates buoyantly upwards, because it is less dense than the water. This movement is stopped when the CO_2 encounters a rock layer with a low permeability. The cap rock acts as a vertical barrier, preventing the CO_2 from rising any farther, and leading to its accumulation directly beneath. In Fig. 1-3 (b), Capillary trapping occurs when the pore spaces in the reservoir are so narrow that the CO_2 can no longer move upwards, trapped as a separate phase by capillary force, despite the difference in density with the surrounding water. In the longer time, CO_2 is dissolves in the formation water and then migrate with the groundwater, a process commonly called solubility trapping occurs, as shown in Fig. 1-3 (c). A consequence of dissolution is that the water with dissolved CO_2 is heavier than the CO_2-free water, and it trends move downwards to the bottom of the reservoir. Mineral trapping [Fig, 1-3 (d)] is the most permanent and safe form of geological storage. Dissolved CO_2 can react with the minerals comprising the storage formation. Some fraction may be converted to stable carbonate minerals. Mineral trapping is believed to be comparatively slow, potentially taking a thousand years or longer.

1.1.3 Global geological storage of CO_2

The engineered injection of CO_2 into subsurface geological formations was first undertaken for EOR projects in Texas, USA, in the early 1970s. Geological storage of anthropogenic CO_2 as a greenhouse gas mitigation option was first proposed in the 1970s, but little research was done until the early 1990s. In 1996, the world's first large-scale storage project was initiated by Statoil and its partners at the Sleipner Gas Field in the North Sea. 5 million tonnes of CO_2 from the Sleipner gas field has been injected into the Utsira formation in the North Sea and eventually 25 million tonnes will be injected before the gas production has ceased (Lindeberg & Begmo, 2003). From 1990s, in a little over a decade, geological storage of CO_2 has grown from a concept of limited interest to one that is quite widely regarded as a potentially important mitigation option (Fig. 1-5) (IPCC, 2005). The Global CCS Institute reported that there were 74 large-scale integrated projects around world on 2011, including eight projects in operation and six projects under construction, with a total CO_2 storage capacity over 33 million tonnes injected per year (Global CCS Institute, 2011). IEA proposed the target of cumulative CO_2 storage of around 145 Gt CO_2 from 2010 to 2050, to meet the target of reducing greenhouse gas

emissions by 50 % by 2050. This requires more than 3400 CO_2 geological storage projects by 2050 (IEA, 2009).

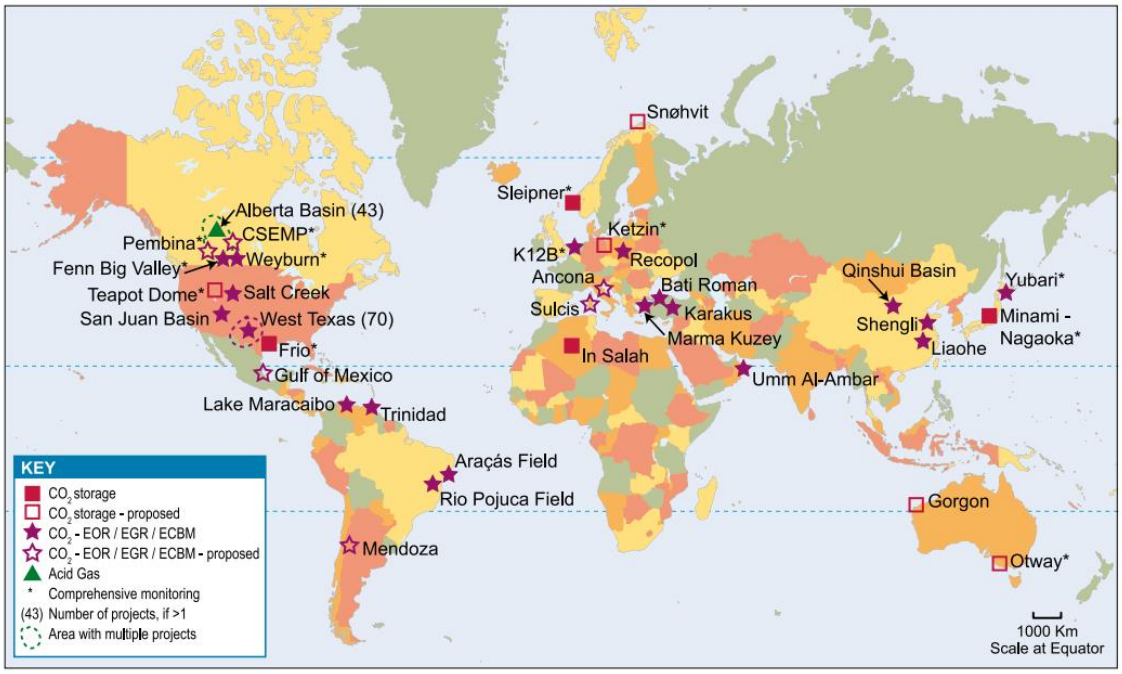

Fig. 1-5. Location of sites where activities relevant to CO_2 storage are planned or under way
Image Source: IPCC special report on carbon dioxide capture and storage (2005)

1.2 CO_2 dissolved into deep saline formation

Dissolution of CO_2 into brine formations considerably improves the security of the storage, since CO_2 dissolved in brine is no longer buoyant.

After CO_2 is injected into a reservoir, the supercritical CO_2 will move upwards because of buoyancy, then accumulate under an impermeable rock. (Fig. 1-6 a). During the migration, some fraction of CO_2 is disconnected from a CO_2 plume and is trapped in porous rock by capillary force. Then, CO_2 dissolves into brine (Fig. 1-6 b), but the thickness of CO_2-saturated brine layer is limited in thin distance because the diffusion of CO_2 molecules in brine is very slow. With the dissolution of CO_2 into the brine, the density of the brine will increase. Since CO_2-saturated brine is 1%–2% denser than groundwater (Yang & Gu, 2006), depending on CO_2 concentration, instability is induced between the two miscible fluids of CO_2-saturated brine and CO_2-free brine because of the differences in density. The density increase induces a convective flow in which heavier CO_2-saturated brine sinks downward while light CO_2-free brine floats upward in the form

of downward convective fingers (Fig. 1-6 c), which accelerates CO_2 dissolution and provides a more secure mechanism of CO_2 storage. Density-driven natural convection governs the rate of CO_2 mass transfer into the brine, leading to a huge impact on the deep carbon cycle that governs the long-term fate of CO_2 in geological storage.

Recently, the density-driven natural convection in porous media has been intensively investigations with implications for CO_2 geological sequestration to access the transition to solubility trapping. In North Sea reservoir conditions, the Rayleigh number is very large, Ra ~ 10^3–10^4 (Erik Lindeberg & Wessel-Berg, 1997; Neufeld et al., 2010; Xu et al. 2006). The onset of natural convection and the mass transport of dissolved CO_2 molecules significantly impact the long-term behaviour of CO_2 injected into geological formations. To this end, the convection process has been investigated by numerical simulations (Chevalier et al. 2015; Ennis-King & Paterson, 2005; Ghesmat et al., 2011; Hidalgo & Carrera, 2009; Xie, at al., 2011). Recently, rapid improvement in computer performance has facilitated three-dimensional numerical simulations at high Rayleigh numbers as well as with the flat finger structure (Pau et al., 2010) and the strong scaling of the wavenumber (Hewitt et al., 2013), which are particular to three-dimensional natural convection. Pau et al. (2010) revealed the differences between two- and three-dimensional fingering structures when CO_2 was dissolved into saline formation.

On the other hand, experimental research has also been conducted by utilizing two-dimensional porous media (Cooper et al., 2014; MacMinn at al., 2012;Touvet at al., 2011). including Hele–Shaw cells (Ehyaei & Kiger, 2014; Faisal et al., 2015; Faisal et al., 2013; Slim et al., 2013), because of the opaque property of porous materials, but not magnetic resonance imaging (MRI) (Johannsen et al., 2006). To model the density-driven natural convection, the nonlinear density profile of a mixture of miscible fluids, of which the details are to be mentioned in chapter 2, is utilized in two-dimensional experimental studies (Backhaus et al., 2011; Huppert et al., 1986; Neufeld et al., 2010). Neufeld et al. (2010) reproduced the convective behavior of CO_2-enriched brine by applying a fluid system comprising solutions of methanol and ethylene-glycol (MEG) mixed with water. Two-dimensional laboratory experiments at a relatively high Rayleigh number and high-resolution numeral simulations at lower Rayleigh number have been conducted. Nakanishi et al. (2016) presented Rayleigh–Taylor convection in three dimensions, demonstrating that the onset time and mass transfer rate are related to the Rayleigh number as well as mechanical dispersion.

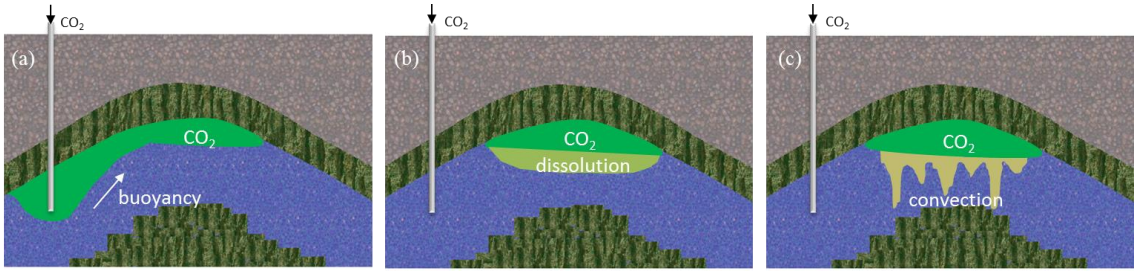

Fig. 1-6. Schematic illustration of the process of CO_2 dissolved into deep saline formation

1.3 CO_2 in Enhanced Oil Recovery

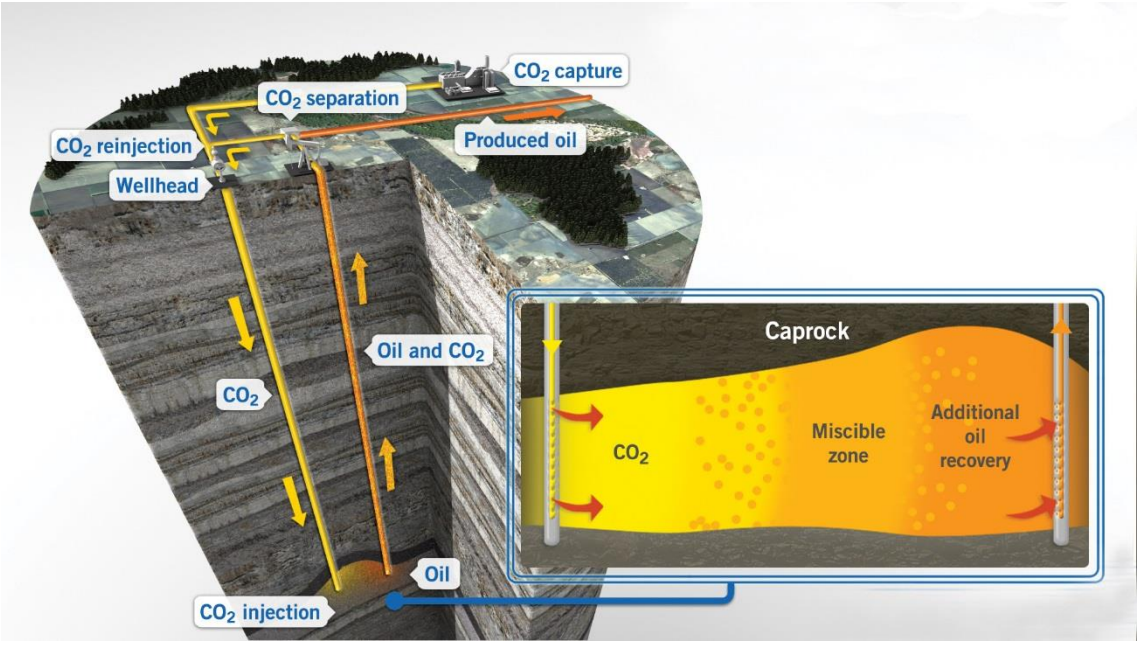

Fig. 1-7. Schematic illustration of the process of CO_2 injection into oil reservoir
Source: Global CCS Institute

Crude oil is extracted by creating pressure gradients within the reservoir that causes the oil to flow through the interconnected porous network to production wells. The production period of the most oil field can be divided into three different stages, including primary, secondary and tertiary recovery. During the primary recovery, only 10-25 % of the reservoir original oil is produced by the natural pressure of the reservoir.

In secondary stage, in most oil field, the pressure gradients are maintained by injecting another fluid (usually water and termed “water flooding”) into reservoir through injection wells when the reservoir pressure could not drive more oil towards production wells.

Typically, the secondary water flooding methods yield oil recovery of respectively additional 30% of the reservoir, leaving more than 50% of original oil in place remaining unrecovered (Pope, 2011), which also gives the tertiary recovery methods huge potential. Crude oil which is not produced by primary or secondary production can be produced by enhanced oil recovery (EOR) methods, such as miscible or partially miscible gas flooding, thermal stimulation, surfactant flooding or polymer flooding.

The use of gas injection, particularly of CO_2, is considered as one of the most promising and attractive methods for improving oil recovery (Alam, et al., 2014; Bayat et al., 2016; Gong & Gu, 2015; Ju et al., 2013; Lei et al., 2016; Olea, 2015; Zheng et al., 2013). The properties of CO_2 and the global concern over the greenhouse gas effect on global warming makes CO_2 as an appropriate injection agent for improving oil recovery, which provides benefits from the view of CO_2 storage (Hussen et al., 2012; Jensen et al., 2013; Karimnezhad et al., 2014). Fig.1-7 is a conceptual image of the CO_2 injection processes for enhanced oil recovery.

When CO_2 is injected into a reservoir, it reaches a supercritical state at depths higher than 800 m (IEA, 2008). For temperatures greater than 31.1 °C and pressures greater than 7.38 MPa, CO_2 is in a supercritical state (Bachu, 2003). At the depth of 3000 m, for the temperature of 85 °C and the pressure of 31.6 MPa, the density and viscosity of supercritical CO_2 are approximately 733 kg/m^3 and 0.06 mPa·s, respectively, both of which vary with pressure and temperature (Nordbotten et al., 2005). The criteria for screening reservoirs to verify CO_2-EOR suitability is that the oil density and viscosity should be less than 825 to 892 kg/m^3 and less than 2 to 15 mPa·s, respectively (Gozalpour at al., 2005), for the conditions of temperatures lower than 90 °C, pressures greater than 103 MPa, and depths in a range from 700 to 3000 m. Thus, the density of CO_2 is estimated to be less than the density of oil, having a variation ranging from 92 to 159 kg/m^3. Viscosity contrasts, expressed as the ratio of CO_2 viscosity to that of oil, range from 0.004 to 0.03. Downward (Shahraeeni et al., 2015; Li & Firoozabadi, 2009) displacement of oil by CO_2 results in potentially high oil production, since CO_2 displacement is unstable due to viscosity contrast, but is stabilized in vertical injection due to gravity. When a low viscousity fluid displaces a high viscousity fluid, viscous fingering could occur. Therefore, this condition (viscosity ratio < 1) is referred to as an "unstable" condition. Conversely, viscous fingering may not occur under a "stable" condition (viscosity ratio > 1). Additionally, when the Darcy velocity of the interface is higher than the critical velocity (Chuoke et al., 1959; Saffman et al., 1958), i.e., the displacement front is stable. When the Darcy velocity of the displacement front is lower than the critical velocity, the induced

fingers on the interface grow with increased buoyancy because the density of CO_2 was lower than that of oil. The supercritical state will allow the CO_2 to come in contact with the oil, keeping the pressure above the minimum miscibility pressure which is in a range from 11.1 to 26.8 MPa varying with temperature (Bon et al., 2006; Bon & Sarma, 2005; Zhang et al., 2015), to improve the displacement of the fluid from the injection well to the direction of the production well (Lashkarbolooki et al., 2016; Rao et al., 2004).

The effect of CO_2 dissolution on oil viscosity has been investigated in many previous studies (Hoteit, 2009; Jadhawar & Sarma, 2010; Rao et al., 2004; Wo et al., 2008). The dissolution of CO_2 in oil increases the density of the CO_2–oil mixture and affects the flow path of CO_2 and recovery performance. Bangia et al. (1993) presented an early breakthrough and high CO_2 production in a vertical-gravity-stable CO_2 flood. Immediately after injection, the interface between the CO_2 and oil was stable because CO_2 is less dense than oil. However, when CO_2 was mixed with the oil, under certain conditions, the density of CO_2-oil mixture increased. Lansangan and Smith (1993) performed experiments and measured the viscosity and density in CO_2/west Texas oil systems. They observed that a monotonic viscosity decrease and a density increase appeared with continued dilution of the oil with CO_2. Grigg (1995) measured the density of a west Texas oil system during the injection of high-pressure CO_2 and observed a 2% increase in the oil density after CO_2 injection before the injected CO_2 reached its saturation point in oil. Ahmed et al. (2012) performed a simulation in a slim tube for CO_2 injection in a two-dimensional vertical cross-section with density increase by dissolution. The results indicated that the density increase had a significant effect on the CO_2 flow path and recovery performance. Without the density effect, there was no fingering. With an appropriate density effect, CO_2 injection from the top resulted in unstable gravity drainage, affecting the breakthrough time and recovery. Shahraeeni et al. (2015) performed two- and three-dimensional numerical simulations of CO_2 injection from the top into the oil phase with density difference. They reported that the fluid system was unstable and observed the formation of gravitational fingers during the injection process.

As mentioned above, after CO_2 injection into oil reservoir, CO_2 and oil could be miscible under certain temperature and pressure conditions. CO_2 dissolution into oil reduces the viscosity of oil, which contributes to oil production. On the other hand, it also leads to an increase in density of CO_2 and oil mixture, resulting in gravitational fingering, which has a negative effect on breakthrough time and oil recovery. In vertical CO_2 displacement, the gravity fingers typically can sink further down to a certain depth due to density increase, which would make production uneconomic. However, details about the

formation and development of gravity fingers, which results from the density effect during the injection process, have not been discussed. Besides, the mixing mechanism between CO_2 dissolved denser oil and CO_2-free light oil is not clear yet.

1.4 Research objectives

The main questions in gravitationally unstable convection are:

1. How fast high-density fingers extend downward?
2. What about the mass transfer during natural convection process?
3. What is the mixing mechanism in the process of convection?
4. How does the heterogeneity of the porous media influence the process of the finger extension?
5. How does the injection speed influence the development of the gravitational fingers during the vertical displacement?

To answer these questions, a new experimental analogue fluid model that allows three-dimensional imaging of the development of gravitational unstable convection flows in a porous medium through micro-focused X-ray computed tomography (CT) is presented here.

In chapter 2, the design of the laboratory experiments was presented. A mixture of miscible fluids, methanol and ethylene-glycol (MEG) doped with sodium iodide (MEG-NaI) and a sodium chloride (NaCl) solution, exhibits a nonlinear density profile, such that the density of intermediate mixtures of these fluids is higher than either pure fluid. Herein, these fluid pairs were used to model the process of the density increase when CO_2 dissolve into the aquifer or oil reservoir.

In chapter 3, the process of CO_2 dissolution in deep saline formation had been modelled using the mixtures of MEG-NaI and NaCl solutions. The three-dimensional structure of extending fingers associated with density-driven natural convection was observed. Three-dimensional CT images provided the local concentration in fingers, which was critical for discussing the effect of Taylor dispersion on the structure of the fingers. The key questions of the finger-extension velocity, the mass transfer rate, and, the effect of transverse dispersion on the finger structure, give insight into understanding the mixing mechanism and evaluating the long-term fate of the injected CO_2 in deep saline aquifers.

The homogeneous pore structure has been assumed to simplify the model. However, in reservoir, stratigraphic structure has a heterogeneity, which is composed of alternating layers, such as sandstone and shale, reflecting an isotropic property in the horizontal direction and different permeability in the vertical direction. In chapter 4, density-driven natural convection also was conducted in a porous medium with layered structure. The influence of heterogeneity on the fingering structure and finger velocity during the convection process was discussed.

In chapter 5, the miscible fluid pair with nonlinear density property, mentioned in chapter 2, was used to model the density increase due to CO_2 dissolution in oil. The development of three-dimensional gravitational fingering in a packed bed during the injection process was observed. The characteristics of fingering associated with an increase in density by mixing in gravitationally stabilized displacements were presented quantitatively. The local concentration distribution in fingers for each unit of time during the injection process was estimated based on CT images, which is critical to discuss the mixing mechanism and the effect of Péclet number on fingering behavior. The key measures of gravitation fingering during the injection process — the finger extension velocity, finger number density, mixing length of fingers, and relative volume of fingers — were compared at different Péclet numbers by changing the permeability of the porous media and the injection speed. The investigation of the effect of the injection process on the fingering structure provides insights into the mixing mechanism and recovery performance of CO_2 injection into oil reservoirs.

Chapter 2: Miscible fluids with nonlinear density property modelling density-driven convection

Rayleigh-Bénard model (Cross & Hohenberg, 1993; Riaz et al., 2006; Hidalgo at al., 2012; Hewitt et al., 2012; Hewitt et al., 2014) and Rayleigh-Taylor model (Wooding, 1969; Sharp, 1984; Heller, 1966; Kolditz et al., 1998; Gopalakrishnan et al., 2017) are two models for describing the natural convection in a porous medium induced due to density difference which leads to the slight fluctuations appeared on the interface then grow into descending fingers. High concentration fingers extend vertical downward with interacting and merging with neighboring. In Rayleigh-Bénard convection, where a porous medium has a finite height, the boundary conditions (show in Fig. 2-1a) at the top boundary are the constant concentration ($C = C_0$) and no flow through the boundary ($u = 0$), namely, the solid wall boundary condition. On the other hand, Rayleigh-Taylor convection (Fig. 2-1b) is an ideal situation with respect to Rayleigh-Bénard convection. The Rayleigh-Taylor instability is induced on the interface between dense fluid (CO_2 saturated brine layer) on the top and light layers (no CO_2 brine layer), and miscible unstable front forms and fluids convectively mix each other. It is assumed that the boundary where no fluid flow locates at the infinite far from the initial interface ($u = 0$, at $z = \pm\infty$). There is no constant interface in Rayleigh-Taylor system.

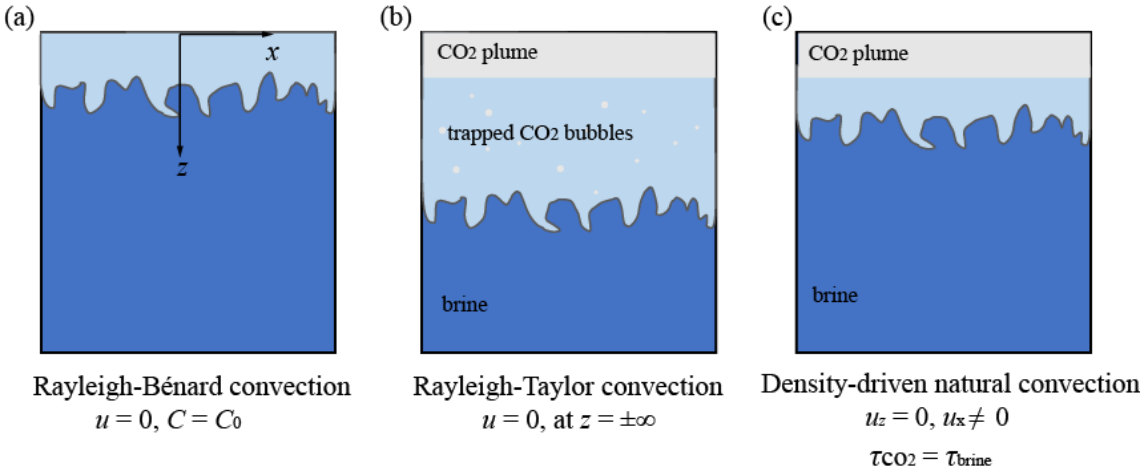

Fig. 2-1. The schematic of different convective mixing patterns

With respect to the these two extreme conditions, the density-driven natural convection, Fig.2-1 (c) depicts the CO_2-brine system, where the dissolved CO_2 is denser than the resident brine and forms an unstable diffusive boundary layer between CO_2 and resident

Note: This chapter has been published as: Wang Lei, Hyodo A., Sakai, S., Suekane, T., Three-dimensional visualization of natural convection in porous media, Energy Procedia, Vol. 86 (2016), 460-468.

brine, resulting in convective mixing due to density difference. There is a state interface between CO_2 and brine established by dissolved CO_2 where the boundary condition of no fluid flow is not imposed ($u_x \neq 0$) but the shear stress should be continuous across the boundary ($\tau_{CO2} = \tau_{brine}$). During the convective mixing process no flow through the interface.

2.1 Design of the laboratory experiments

Huppert et al. (1986) performed the laboratory experiments to model the convective mixing of air and hot ash in the pyroclastic flow, using the nonlinear property of the density between a mixture of MEG and water. Neufeld et al. (2010) utilized the mixture of MEG and water for a two-dimensional experimental study on density-driven natural convection. I propose to expand the experimental scheme into three-dimensions by doping the fluids with NaI and/or NaCl for visualization using an X-ray CT scanner. Because the salts (NaI and NaCl) are highly soluble in each phase, the density contrast and the X-ray attenuation contrast can be adjusted through their doping concentrations. After trial of several pairs of concentrations of NaI in MEG and NaCl in water, it is found that the concentrations shown in Fig. 2-2 are best for modeling the conditions at high Rayleigh numbers.

The dimensionless equations expressing the Boussinesq-type flow and concentration fields are given by (Ouakad, 2013; Ruith & Meiburg, 2000)

$$\nabla^* U^* = 0, \tag{2-1}$$

$$U^* = -(\nabla^* P^* - C^* \vec{z}), \tag{2-1}$$

$$\frac{\partial C^*}{\partial t^*} = -U^* \cdot \nabla^* C^* + \frac{1}{Ra} \nabla^{*2} C^*, \tag{2-3}$$

Equation 2-1 is the incompressibility constraint, equation 2-2 is Darcy's law, and equation 2-3 is the convection-diffusion equation governing solute transport. In equation (2-1)-(2-3), U is Darcy velocity, representing the ideal Darcy velocity driven by gravity force with an initial density difference between CO_2-saturated water and CO_2-free water, C is the concentration of the dissolved CO_2, P is pressure with respect to hydrostatic datum, $\vec{z}$ is a unit vector pointing in the direction of gravity. In these equation, the superscript "*" indicates dimensionless variables. Darcy velocity (U), pressure (P), time (t), and height (h) are scaled by using the following appropriate dimensional reference quantities:

$$U^* = \frac{U}{\frac{k\Delta\rho g}{\mu}},\ P^* = \frac{P}{\frac{\varphi D_m \mu}{k}},\ t^* = \frac{D_m t}{H^2},\ h^* = \frac{h}{H} \tag{2-4}$$

The Rayleigh number is defined as the strength of convection relative to the diffusion as

$$Ra = \frac{kgH\Delta\rho}{\varphi\mu D_m} \quad , \tag{2-5}$$

where H is the characteristic macroscopic length, in this study, the height of the packed bed is defined as the characteristic macroscopic length, which are constant throughout the experiments for each part. k is the permeability, g is the gravitational acceleration, Δρ is the density difference between the mixture (MEG-NaI and NaCl solutions) and NaCl solution, φ is the porosity, D_m is molecular diffusion coefficient, and μ is the viscosity of NaCl solution. The molecular diffusion coefficient of iodide ion in water depends on temperature as well as concentration (J. H. Wang & Kennedy, 1950). In this study, a constant value of 2×10^{-9} m^2/s was used. The Rayleigh number is the single parameter characterizing the convective flow in a porous medium.

2.1.1 Miscible fluid pair with nonlinear density property

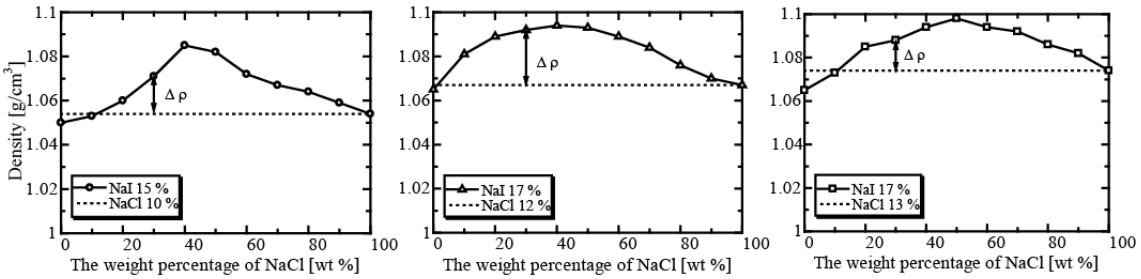

Fig. 2-2. The density profiles of a mixture of MEG-NaI and NaCl solutions for various NaCl concentrations of (a) 10, (b) 12, and (c) 13 wt%. The representative density difference (Δρ) between MEG-NaI and NaCl solution is defined at NaCl concentrations of 30 wt%.

Table 2-1. Properties of fluids.

Fluid pair	MEG-NaI density [g/cm^3]	NaCl density [g/cm^3]	NaCl viscosity μ, [mPa·s]	Typical density difference $\Delta\rho$ [g/cm^3]
A	1.064	1.067	1.065	0.025
B	1.050	1.054	1.049	0.017
C	1.065	1.074	1.113	0.014

The mixing of NaCl solution and MEG-NaI models CO_2 dissolution into brine. Initially, MEG-NaI is less dense than the NaCl solution; however, with mixing, the density of the mixture increases and exceeds that of the NaCl solution, and the degree to which it exceeds that of NaCl solution depends on the fraction of MEG-NaI, as shown in Fig. 2-2. The increase in density causes an unstable stratification that drives convective flow in the form of descending fingers. A representative density difference defined at 70 wt% of MEG-NaI, denoted with arrows in Fig. 2-2, is used to evaluate the Rayleigh number, since the weight percentage of MEG-NaI in the fingers formed at the interface rages from 64 to 72 wt%. The details of the fluid pairs are shown in Table 2-1.

2.1.2 Particle properties

A packed bed of plastic beads was employed as a porous medium. Four average-diameter plastic beads were used, d_p = 1410 μm (Ube Sand Engineering Co. Ltd., XH series), d_p = 975 μm, d_p = 780 μm, and d_p = 647 μm (a mixture of particles with average diameters of 513 μm and 780 μm), to vary the permeability related to the Rayleigh number. The permeability of the packed bed was estimated by measuring the pressure drop for various flow rates in water flooding. The porosity was measured by determining the weight change before and after saturation with the NaCl solution. The properties of the porous medium are summarized in Table 2-2.

Table 2-2. Properties of the porous medium.

Average particle diameter d_p (μm)	Permeability k (m^2)	Porosity φ (-)
647 (400–625) and (530–1030)	9.51×10^{-11}	0.49 ± 0.021
780 (530–1030)	2.63×10^{-10}	0.49 ± 0.025
975 (760–1190)	4.87×10^{-10}	0.49 ± 0.014
1410 (1140–1680)	8.24×10^{-10}	0.48 ± 0.018

For all experiments in this study, the Rayleigh number was in a range of 1060 to 16000. For the geological projects of CO_2 injection into deep saline formation, at Sleipner in North Sea, Rayleigh number is 12000 (Neufeld et al, 2010), which is a relative large value. However, at Alberta Basin in Canada, Rayleigh number is in a relative small range from 0 to 1359 (Hassanzadeh et al., 2007). The critical Rayleigh number (Ra_c) is defined as

$Ra_c = 4\pi^2 \approx 39$. When $Ra < Ra_c$, only pure diffusion occurs without convective mixing. In this research, the range of the Rayleigh number covered the reservoir conditions of CO_2 injection project.

For the experiments, on one hand, the Rayleigh number could be reduced by decrease the density different and permeability. However, the scale of packed bed limited the reduction of Rayleigh number. When Rayleigh number was less than 1000, only few finger occurred and extended downward slowly because of the effect of the cylindrical wall. On the other hand, when Rayleigh number was larger than 16000, the development of high-density fingers occurred too fast to investigate. The time of 70 s required for one CT scan had a significant effect on experimental results. The time for one CT scan limited the increase in Rayleigh number.

2.2 Measurement and Image processing

The experiments were conducted at room temperature and atmospheric pressure. The detailed experimental setup and procedures will be presented later for each chapter.

A micro focused X-ray CT scanner (Comscantecho Co., ScanXmate-RB090SS) which allows pore-scale observation of phenomena in a porous medium is employed in this study. For each part of the experiments, the entire bed of packed beads was scanned with the X-ray CT scanner. The reconstructed images comprised 496 image slices of 496 × 496 pixels with a resolution in a range of 171–201 μm/pixel. It takes approximately 70 s (10 frame/s) to scan 496 images of the entire packed bed from all directions by using a flat-panel detector. The scans were repeated at a certain time interval until the extended fingers reached the bottom of the packed bed.

The images produced by an X-ray CT scanner are in gray-scale. The brightness of the reconstructed images is determined by the object's attenuation of X-ray. Further, gray value is an indicator of brightness. Image processing was performed with the free software Image J to select the cylindrical area where the dynamics occurs. As depicted in Fig. 2-3(a), on the left are the reconstructed original images. NaI has a better attenuation than NaCl. Therefore, NaI in fingers looks brighter in the image and has a higher CT value.

During reconstruction, noise removal, ring artifact reduction, and beam hardening reduction filters were applied to images. Further image enhancement involving Gaussian filters was performed to reduce the noise associated with impurities of particles and to smooth the gray-level images. Fig. 2-3(b) is an example of such a process. The CT values

were transformed into NaI concentrations using calibration curves (Fig. 2-4) that were obtained in preliminary experiments. Fig. 2-3(c) depicts the local concentration distribution in fingers, which illustrates higher CT values.

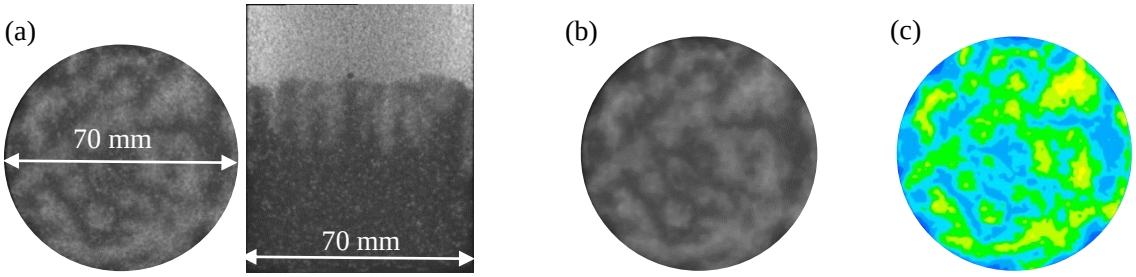

Fig. 2-3. (a) Original images having a resolution of 193 μm/pixel (horizontal image, left; vertical image, right), (b) the image after performing noise removal and applying Gaussian filter, (c) the CT value were transformed into NaI concentration.

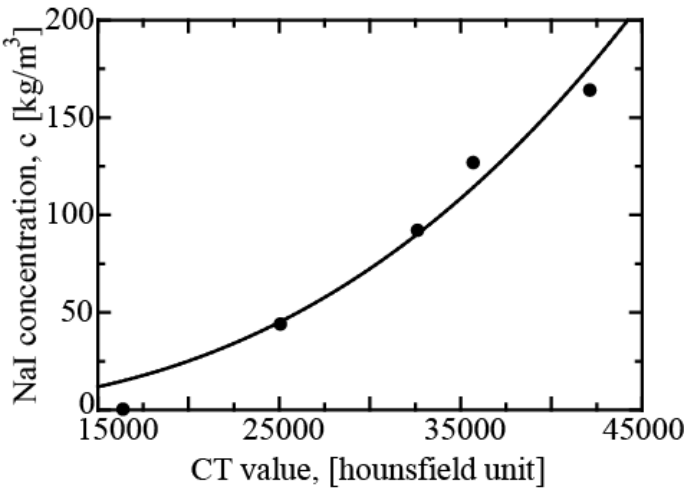

Fig. 2-4. Calibration curve

Chapter 3: Three-dimensional fingering structure of density-driven natural convection

In this chapter, three-dimensional visualizations of a density-driven natural convection process were performed using micro-focused X-ray CT technology. Nonlinear density profiles of MEG-NaI and NaCl solutions were utilized to model the convection process of CO_2 dissolution in saline formation in a porous medium. The development of convective fingering, finger-extension velocity, finger-number density, mass transfer rate, and the effect of the transverse dispersion on finger structure were investigated.

3.1 Experimental setup and procedures

In these experiments, NaCl solution was used to model the saline formation at the bottom, and the MEG-NaI solution was used to model less dense CO_2 at the top. The experiments were conducted using the following procedures. First, the NaCl solution was pulled into the packed bed by using a vacuum chamber. Next, in order to reduce the disturbance on the initial interface, after removing the top part of the packed bed, the particles saturated with a MEG-NaI solution (30 mm in height) were put manually above the particles saturated with a NaCl solution (50 mm in height) (Fig. 3-1). Then, the whole packed bed was scanned by an X-ray CT scanner.

The reconstructed images consist of 496 slice images of 496 × 496 pixels at a resolution of 193 μm/pixel in all directions. The scan was repeated every 120 s until natural convection was completed. The local concentration in the porous medium was obtained from three-dimensional CT images, which was defined as the NaI concentration in each location.

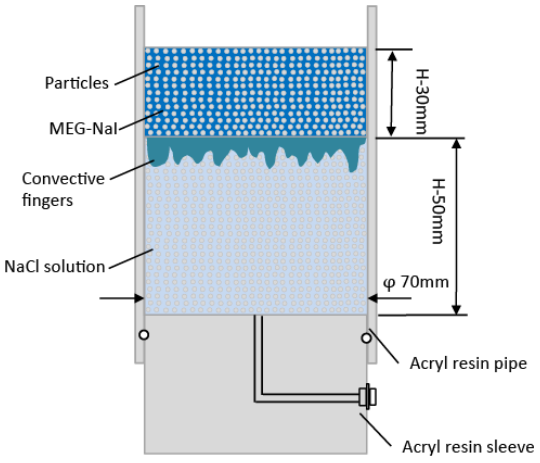

Fig. 3-1. Packed bed of melamine resin particles.

Note: This chapter has been published as: Wang Lei, Nakanishi Y., Hyodo A., Suekane, T., Three-dimensional structure of natural convection in a porous medium: Effect of dispersion on finger structure, Int. J. Greenhouse Gas Control., Vol. 53 (2016), 274-283.

The details of three fluid pairs were mentioned before in Table 2-1. Nine experimental runs were conducted for the combination of three fluids pairs and three particle diameters in a *Ra* range between 2600 and 16000, as shown in Table 3-1.

Table 3-1. Range of the Rayleigh number in experiments.

Run #	Average particle diameter d_p, [μm]	Fluid pair	Rayleigh number *Ra* [−]
1 A	780	A	5010
1 B		B	3360
1 C		C	2600
2 A	975	A	9290
2 B		B	6220
2 C		C	4810
3 A	1410	A	16037
3 B		B	10739
3 C		C	8315

3.2 Development of convective fingers

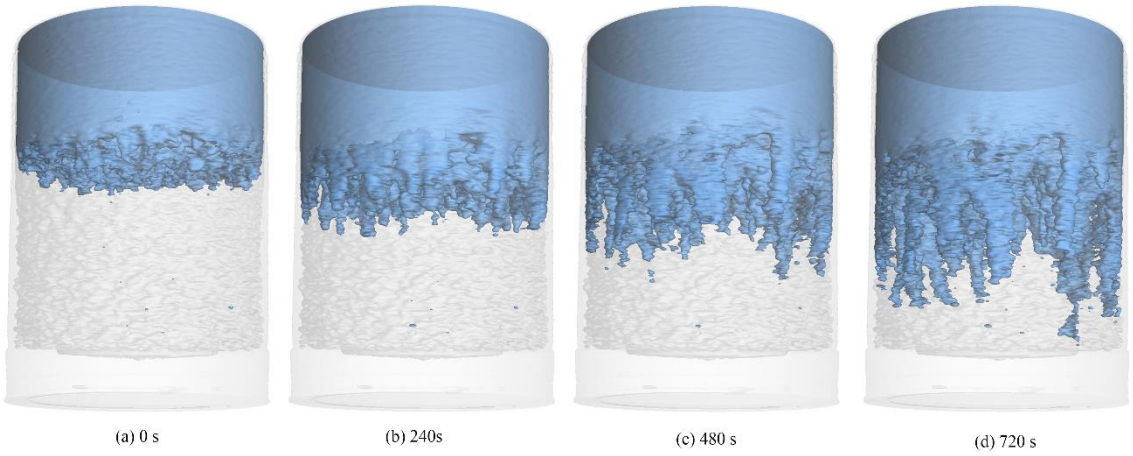

Fig. 3-2. Structure and development of fingers in the three-dimensional porous medium with permeability $k = 4.87 \times 10^{-10}$ m^2 at a Rayleigh number of 6220. The blue indicates the iso-contour surface of MEG-NaI concentration of 24.8 kg/m^3. The times shown on the bottom are all the starting time of each scan for different time step.

The sequence of time-lapse images of convective fingers in three dimensions is given in Fig. 3-2. It shows the development of density-driven fingers in the transition from a

diffusion-dominated flow to a convection-dominated flow. Slight fluctuations at the interface between the MEG-NaI and NaCl solutions, shown in Fig. 3-2(a), developed into a dense concentration of fingers. These subsequently merged to form larger fingers, developing a complex convective flow. The fingers coalesced with neighboring fingers, growing in diameter, extending vertically downwards (Figs. 3-2b–d), and eventually reaching the bottom of the packed bed. The heavier mixture of the MEG-NaI and NaCl solutions moved downward in the fingers, while lighter fluid around the fingers moved upward. Numerical simulation results (Fu et al., 2013; Neufeld et al., 2010; Pau et al., 2010) have shown that the upwardly moving fluid forces nascent fingers at the top interface to move horizontally and merge with an adjacent, extended finger that has a larger extension velocity. This accelerates the rate at which MEG-NaI is removed from the top boundary by the downward extension of the fingers.

3.3 Finger-extension velocity

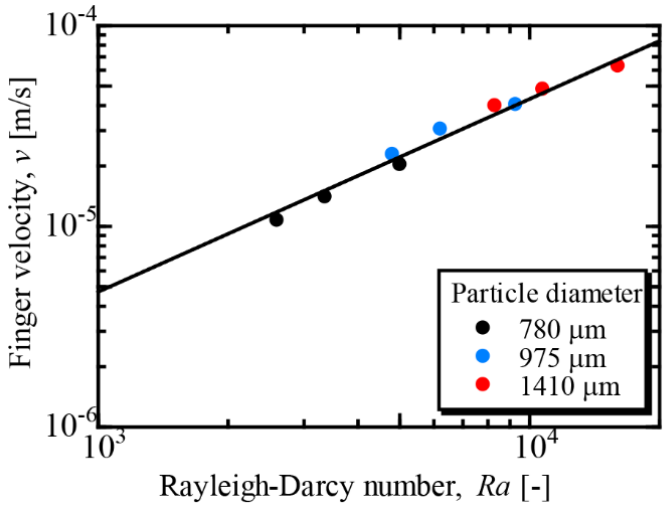

Fig. 3-3. Finger-extension velocity versus the Rayleigh number. A least squares fitting is provided by $v = cU$ (solid line) for $c = 0.35$ and $r^2 = 0.98$.

The finger-extension velocity (v) is the key factor in evaluating the intensity of convective mixing. Because the fingers extend directly downward, as seen in Fig. 3-2, the finger-extension velocity can be estimated from the change in the position of the tip over a certain time interval. Fig. 3-3 plots the finger-extension velocity against the Rayleigh number. The velocity increased as the Rayleigh number increased. A characteristic velocity U was defined by

$$U = \frac{k}{\mu}\Delta\rho g \ , \tag{3-1}$$

representing the ideal Darcy velocity driven by gravitational force with an initial density difference of $\Delta\rho$ between the MEG-NaI and NaCl solutions. The finger-extension velocity was in good agreement with this characteristic velocity, with a correlation coefficient of 0.35 ($|r|$ = 0.99).

3.4 Finger-number density

In three-dimensional convection, the distance between fingers depends on the selection of neighboring fingers. This cannot be determined uniquely without taking into account the cell structure of the convection. To analyze the structure of the fingers quantitatively, therefore, the finger-number density was evaluated, which was defined as the concentration of fingers on a horizontal surface. This density was computed from horizontal cross-sectional images, as shown in the inset of Fig. 3-4. In the image processing procedure, high-concentration pixels with a radius below a certain value (specific to the particles) were assumed to be noise associated with the impurity of the packed particles, and were discarded. A Gaussian blur filter was then applied to the image. Finally, an MEG-NaI concentration 2% higher than its surroundings was identified as a finger using the Local Maxima command in the Image J analysis software.

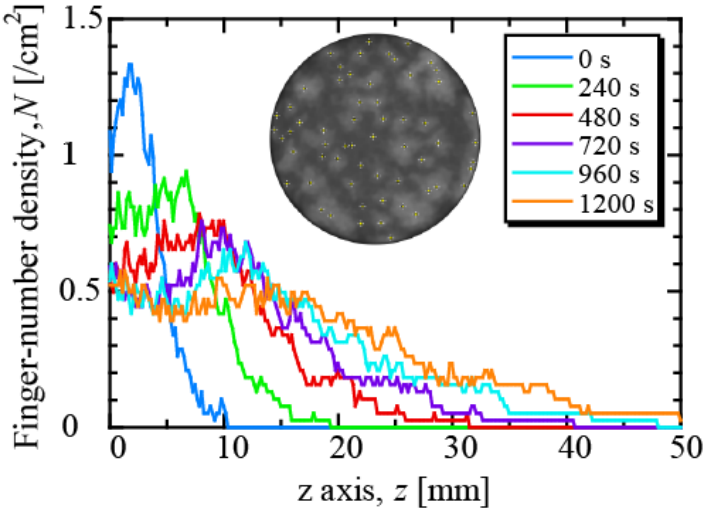

Fig. 3-4. Time evaluation of finger-number density at Ra = 3360 (Run # 1B) in a porous medium with an average particle diameter of 780 μm. The initial interface is located at a height of 0 mm (z = 0 mm) at time 0 s. The time for the curves in different color are the starting time of the scan for different time steps. The inset shows the peak concentration detected as fingers in a horizontal cross-sectional image.

Figure 3-4 illustrates the distribution of the finger-number density at different time steps with *Ra* = 3360 (Run # 1B). Here, the *z*-axis runs in the direction of gravitational acceleration and *z* = 0 mm is the initial interface between the MEG-NaI and NaCl solutions. The fluctuations arose from the impurity of the particles and the noise removal bias. In the early stage of convective finger formation, a maximum finger-number density of 1.3 /cm^2 appeared at the interface (*z* = 0 mm). The nascent fingers occupied a relatively small region and produced a sharp peak as the finger-number density reached its maximum value. The fingers then began to extend downward while merging with neighboring fingers. This caused the maximum finger-number density to decrease, flattening the peak compared with comparable prior time steps. The finger-number density at the fixed position *z* = 0 mm decreased over time, as discussed below. At *t* = 1200 s, a plateau extended across the range *z* = 0–15 mm, with vertical columnar fingers.

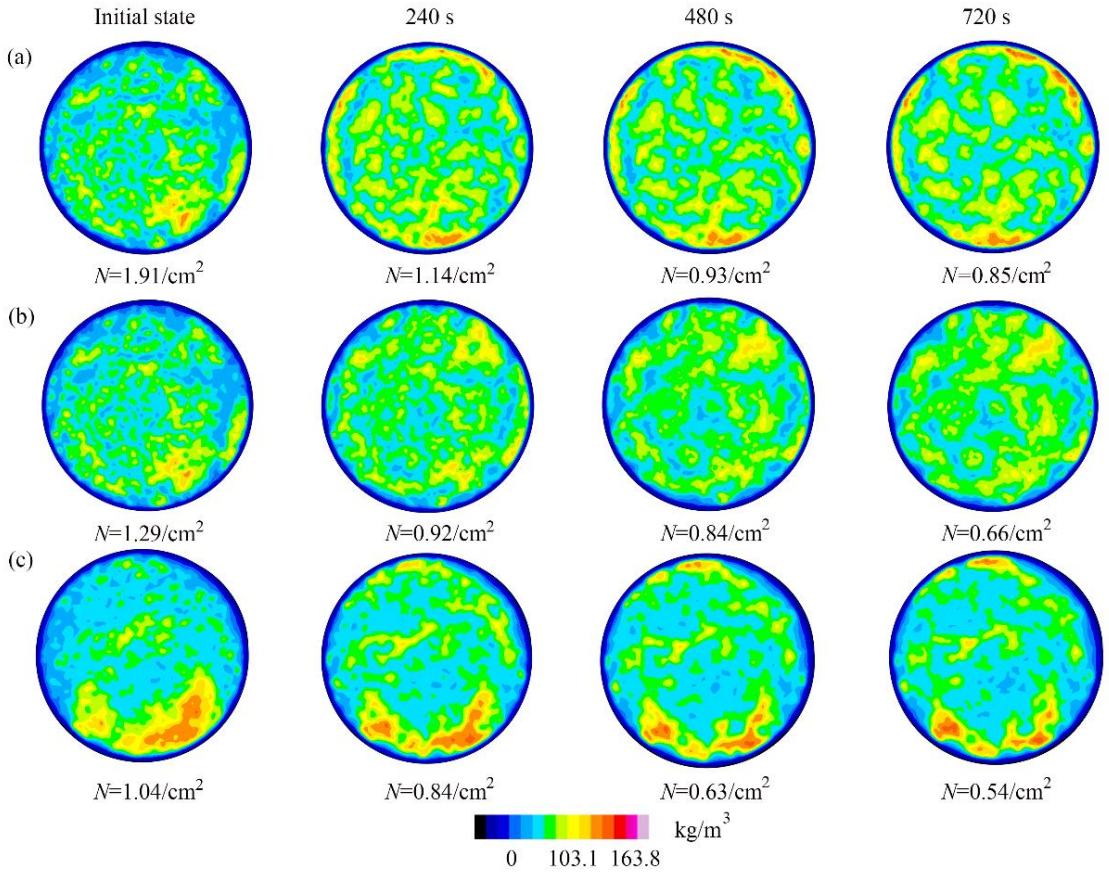

Fig. 3-5. Distribution of fingers in a horizontal cross-section (*z* = 0) in a porous medium with permeability $k = 2.63 \times 10^{-10}$ m^2 for (a) *Ra* = 5010 (Run # 1A); (b) *Ra* = 3360 (Run # 1B); and (c) *Ra* = 2600 (Run # 1C). *N* denotes the finger-number density for each time step. The inner diameter of the tube is 70 mm.

The distribution of fingers in the horizontal cross-section at the initial interface for different Rayleigh numbers and time steps is shown in Fig. 3-5. In this experiment, the Rayleigh number could be varied by changing the permeability or the density difference. When the permeability was fixed, the density difference was used to change the Rayleigh number. A comparison of the image series with a higher Rayleigh number [Fig. 3-5(a)] and the image series with a lower Rayleigh number [Fig. 3-5(c)] shows that the finger-number density decreased as the Rayleigh number decreased, whereas the finger diameter increased. In the time interval from 240 to 720 s, the fingers remained at the same horizontal location and their structure was unchanged, while the finger-number density gradually decreased with respect to the vertical direction as adjacent fingers coalesced.

Three-dimensional numerical simulations by Fu et al. (2013) for free convection at *Ra* = 6400, by Hewitt et al. (2014) for thermal convection at *Ra* = 4000, 8000, and 16000, and by Pau et al. (2010) for natural convection at *Ra* = 9184 all identified a flow region inside the boundary dominated by the growth and interaction of long, thin, sheet-like finger structures. The horizontal images from these studies are consistent with the three-dimensional experimental results shown in Fig. 3-5. Shahraeeni et al. (2015) and Pau et al. (2010) performed numerical simulations in two- and three-dimensions, demonstrating significant differences between the two-dimensional and three-dimensional finger structures, while Shahraeeni et al. (2015) reported that the finger number at the early stage was similar in the two-dimensional and three-dimensional cases. In the longer term, the three-dimensional simulations produced thinner, straighter fingers that extended downward more quickly, taking on a pencil-like shape, whereas the two-dimensional fingers had a folded-sheet configuration. This is consistent with the finger structures found in the present study.

Figure 3-6 shows the finger-number density at various time steps plotted against the dimensionless time t^* defined by

$$t^* = tU / H , \tag{3-2}$$

where t is a dimensional measurement time. Because the velocity of finger extension correlated with the characteristic velocity U at a coefficient of 0.35, as reported above, the fingers almost reached the bottom of the packed bed at t^* = 2.9. The finger-number density was evaluated on horizontal cross-sections 2.5 mm [Fig. 3-6(a)], 5.0 mm [Fig. 3-6(b)], and 8.0 mm [Fig. 3-6(c)] below the initial interface that the fingers reached simultaneously following the onset of convection.

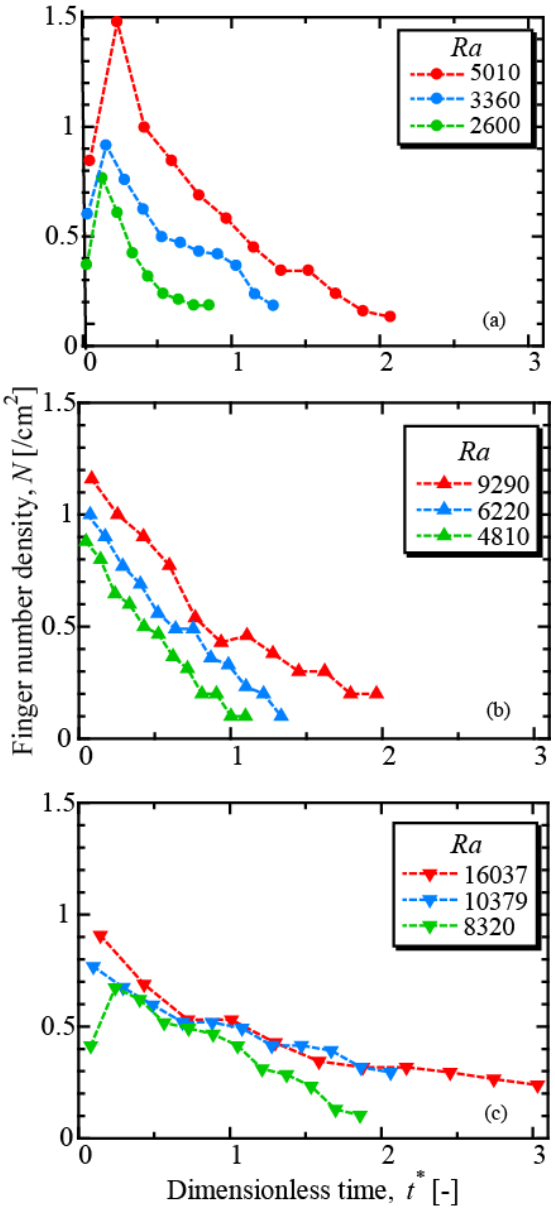

Fig. 3-6. Relationship between finger-number density and dimensionless time for the porous medium at (a) d_p = 780 μm, $k = 2.63 \times 10^{-10}$ m^2; (b) d_p = 975 μm, $k = 4.87 \times 10^{-10}$ m^2; and (c) d_p = 1410 μm, $k = 8.24 \times 10^{-10}$ m^2. The fluid pair or density difference is the same for the same legend of the same color. The finger number-density is evaluated in the horizontal cross-section (a) 2.5 mm, (b) 5.0 mm, and (c) 8.0 mm below the initial interface that all the fingers reach at the same time, following the onset of convective mixing.

When the permeability was constant, the finger-number density increased in line with the Rayleigh number at all times. However, when the Rayleigh number was increased while the permeability was fixed at a constant density difference, the finger-number density decreased in the early stage of convection ($t^* < 1$). Over a longer time scale ($t^* > 2$), the

finger-number density increased in line with an increase in the Rayleigh number. As discussed below, the increased finger-extension velocity at higher Rayleigh numbers and higher permeability increases dispersion between the descending fingers and ascending flows, steeply reducing the finger-number density at the early stages of convection.

Note that Fig. 3-6(a) does not indicate an increase in the onset time with an increase in the Rayleigh number. Linear stability analysis (Ennis-King & Paterson, 2005) suggests that the onset time is related to the properties of the fluid system, given by the following relation:

$$t_{onset} = c_0 \left(\frac{\mu\varphi}{k\Delta\rho g} \right)^2 D \,. \tag{3}$$

The magnitude of c_0 covers wide range of values (Pau et al., 2010) in the literature. Linear stability analysis (Ennis-King & Paterson, 2005; Xu et al., 2006) has identified c_0 values in the range 75–78. The onset time is produced by minimizing the wave numbers at the point at which infinitesimal disturbances form. Under the experimental conditions in this study, the onset time fell in the range 1–35.48 s (c_0 = 75), which is shorter than the 60 s required to complete a CT scan, making it impractical to study the effect of onset time.

3.5 Effect of dispersion on the fingering structure

Dispersion reflects the superficial diffusion associated with the complicated structure of porous media. Far from the interface, convective fingers extend at a velocity reflecting the density difference between the NaI-enriched downward moving fingers and the upward flows of NaCl solution. The shear layer established between the counter flows may induce a Taylor dispersion of the concentration in the radial direction around the finger. Hidalgo and Carrera (2009) posited that this Taylor dispersion is a major factor in the reduction of the onset time. In two-dimensional numerical simulations, the growth of transverse dispersion has been shown to strengthen the vertical spread of the solute, making the fingers balloon shaped and dispersive (Xie et al., 2011) and slow down convection (Chevalier et al., 2015; Xie et al., 2011). The dispersion induced by free convection flow at *Ra* = 500 and 1000 was demonstrated by Ghesmat et al. (2011), with dramatic changes in the finger pattern as dispersion became enhanced. The number of fingers increased and highly nonlinear interactions, including merging and slitting, were identified as dispersion strengthened. Numerical simulations by Xie et al. (2011) showed

that a reduction in transverse dispersion weakened the lateral dissipation, causing narrower fingers to be formed.

In 2D porous media, Sahimi (2011) describes transverse dispersion (D_T) as a function of Péclet number (*Pe*) in four regimes as follows: (1) *Pe* < 0.3, $\frac{D_T}{D_m} = \frac{1}{F\varphi}$, defines the diffusion regime in which convection is so slow that molecular diffusion controls the mixing. *F* is formation factor and φ is the porosity of the porous medium; (2) 0.3 <*Pe* < 5 defines the transition zone in which convection contributes to dispersion, but the diffusion still effects the dispersion strongly; (3) 5 <*Pe* < 300, $\frac{D_T}{D_m} = \frac{1}{F\varphi} + \alpha Pe^{\beta}$, defines the power-law regime. Convection contributes dominantly, but the effect of diffusion cannot be neglected. The values of coefficient are α ≈ 0.01-0.05 and β ≈ 0.9; (4) 300 <*Pe* < 10^5, $\frac{D_T}{D_m} \sim Pe$, defines the purely convective regime. This type of dispersion is also called mechanical dispersion. Bijeljic and Blunt (2007) presented the network model results for transverse dispersion coefficients. They estimated D_T by $D_T = \frac{1}{2}\frac{d\sigma_T^2}{dt}$, calculating the variance of the distance travelled by particles in time. σ_T is the variance of the solute position in transverse direction.

However, in 3D experiments, it is necessary to define a new model to describe the relation between the transverse dispersion and Péclet number.

In the present study, it was able to evaluate the dispersion coefficient from the three-dimensional distribution of NaI concentration in the porous medium derived from the CT images (Fig. 3-7). To the best of my knowledge, no experimental estimation has been made of the dispersion coefficient for the shear flows established between the counter flows. Because the fingers extended straight downward, convective flow in the horizontal direction can be neglected. The direction of the descending fingers was defined as the *z*-axis and the line perpendicular to this (transverse) as the *r*-axis, as shown at the bottom left of Fig. 3-7.

The dispersion coefficient in the *r*-direction D_T was evaluated using fine fingers with a relatively high extension velocity to reduce the influence of the merging and interaction of the adjacent fingers, as shown by the red box in Fig. 3-7(a). The average concentration over the area occupied by a single finger was estimated from the horizontal cross-sectional image. The concentration distribution in the *z*-direction of a finger at different time steps is shown in Fig. 3-7(b). The concentration of NaI decreased along the finger,

whereas the gradient remained constant in the time range between 240 and 1200 s. As time progressed, the tip of the finger descended downward, while the initial interface moved upward. The finger-extension velocity v was estimated from the distance traveled by the tip of the finger, as shown in Fig. 3-7 and Table 3-2. Figure 3-7(d) shows the distribution of NaI concentration in the r-direction along the red bar crossing the center of the developing fingers in Fig. 3-7(c). The half-value width and gradient of the linear approximation of this profile were used to estimate the r_f and the r-direction concentration gradient $\partial C/\partial r$, respectively.

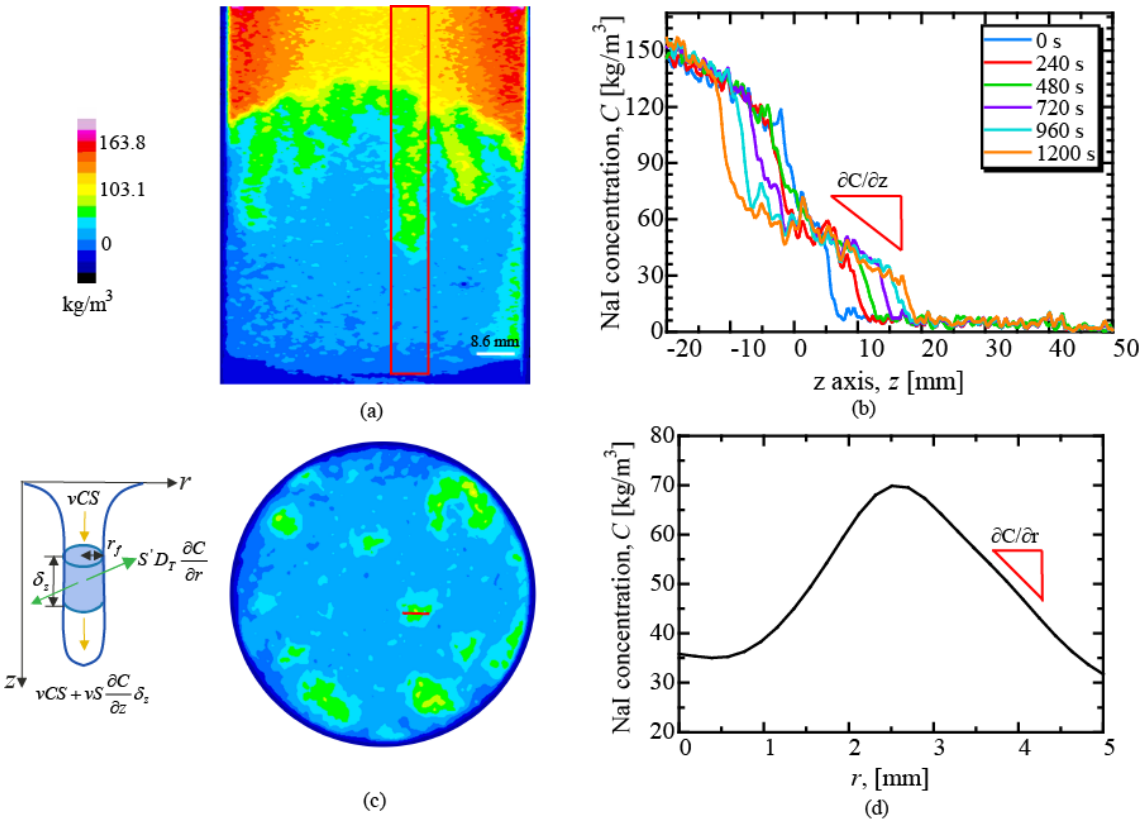

Fig. 3-7. MEG-NaI concentration distribution in a finger of Ra = 3360. (a) and (c) are vertical and horizontal cross sectional images, respectively, while (b) and (d) show MEG-NaI concentration distribution in longitudinal direction and transverse direction, respectively.

Mass conservation for a finger with a cylindrical shape is described by the balance of convection in the z-direction and dispersion in r-direction, as follows:

$$\frac{\partial VC}{\partial t} + \delta_z \frac{\partial (vCS)}{\partial z} = S' D_T \frac{\partial C}{\partial r}, \tag{3-4}$$

where $V = S\delta_z$ is the control volume (CV), $S = \pi r_f^2$ and $S' = 2\pi r_f$ are the end surface area and the side area of the disk-shaped CV, respectively, and r_f is the radius of the CV. The

first term on the left hand side denotes the change in mass with time in the CV, the second term denotes the net increase in mass by convection in the *z*-direction, and the right hand side denotes a decrease in mass crossing the cylindrical wall due to dispersion. Some fraction of the mass supplied through the top surface of the CV is lost by dispersion through the side-wall.

Figure 3-7(b) shows that the concentration of NaI in the finger at a particular location was constant over time, for example at z = 4 mm in the time range between 0 and 1200 s and at z = 10 mm in the time range between 480 and 1200 s. With the assumption of a steady state ($\partial/\partial t = 0$), equation (3-4) can be put into the following form:

$$v r_f \frac{\partial C}{\partial z} = 2 D_T \frac{\partial C}{\partial r} . \tag{3-5}$$

This allows the D_T of the shear flow between the descending fingers and the ascending NaCl flow to be estimated. Figures 3-7(b) and 3-7(d) provide the *z*-direction concentration gradient $\partial C/\partial z = -2.43$ kg/m^4 and the *r*-direction concentration gradient $\partial C/\partial r = -19.12$ kg/m^4, respectively. The transverse dispersion coefficients at all *Ra* values are shown in Fig. 3-8 and Table 3-2. The concentration gradient in the *r*-direction was 6–10 times (on average 8 times) higher than that in the *z*-direction. Both concentration gradients decreased slightly in line with *Ra*.

Table 3-2. Gradients in the concentration were evaluated with the local NaI concentrations, as shown in Fig. 3-7. The finger extension velocity (v) was evaluated using the migration distance of the tip of the finger. The transverse dispersion coefficient D_T and Péclet number Pe^* were evaluated using equations (3-5) and (3-6), respectively.

Ra [−]	$-\partial C/\partial z$ [kg/m^4]	$-\partial C/\partial r$ [kg/m^4]	v [m/s]	D_T [m^2/s]	Pe^* [−]
2600	1.94	18.18	1.07×10^{-5}	1.83×10^{-9}	8.51
3360	2.43	19.12	1.40×10^{-5}	2.22×10^{-9}	11.10
5010	2.65	18.69	2.03×10^{-5}	5.33×10^{-9}	16.16
4810	2.22	14.85	2.28×10^{-5}	4.72×10^{-9}	22.68
6220	2.28	14.38	3.05×10^{-5}	6.30×10^{-9}	30.34
9290	1.67	15.16	4.04×10^{-5}	7.79×10^{-9}	40.19
8315	1.63	15.41	3.99×10^{-5}	6.82×10^{-9}	57.41
10739	1.51	11.35	4.82×10^{-5}	1.09×10^{-8}	69.34
16037	1.35	11.90	6.29×10^{-5}	1.36×10^{-8}	90.50

D_T is usually estimated in a uniform flow of forced convection, so that it is correlated with the Péclet number (*Pe*), as shown in Fig. 3-8. *Pe* is defined in equation (3-6) as the ratio between the time required for the fluid to traverse a characteristic length by diffusion and the time needed to traverse the same length by advection:

$$Pe^* = \frac{v d_P}{\varphi D_m} \cong c \frac{d_P}{H} Ra\,, \tag{3-6}$$

where v/φ is the interstitial velocity, derived from the finger-extension velocity. As *Ra* increased from 2000 to 16000, the Péclet number increased from 8.51 to 90.5 because the finger-extension velocity *v* is proportional to *Ra* (Fig. 3-3). The transverse dispersion coefficient increased with Pe^*, indicating a higher dispersion in the *r*-direction and a reduced NaI concentration gradient in the *r*-direction at higher *Ra* values. This is because transverse dispersion between the downward high-concentration fingers and the upward NaCl flows dampens the finger shape as the *Ra* increases. Figure 3-8 shows that the effect of the dispersion is non-negligible at high Rayleigh numbers. The plot of the estimated transverse dispersion coefficients (D_T/D_m) against the Péclet number shown in Fig. 3-8 suggests the following relationship between D_T and the Péclet number:

$$D_T / D_m = 0.211 Pe^{*0.76},\ r^2 = 0.90\ . \tag{3-7}$$

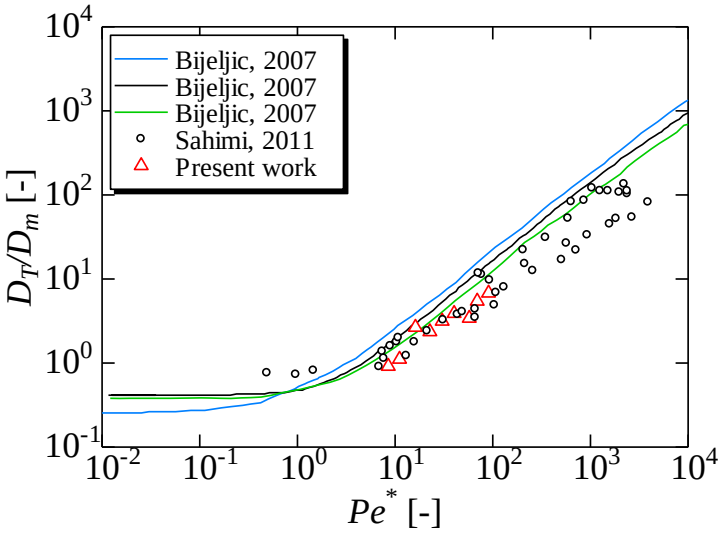

Fig. 3-8. Comparison of previous research results (Bijeljic & Blunt, 2007) (the solid lines) and Sahimi (2011) (round dots) and experimental results (red triangle) of the transverse dispersion coefficient (D_T/D_m) versus the Péclet number.

This suggests that the transverse dispersion is enhanced by an increase in the strength of density-driven natural convection. Our experimental results, evaluated in the shear layer, were in good agreement qualitatively with the D_T previously reported in uniform flows (Bijeljic & Blunt, 2007; Sahimi, 2011). In a uniform flow, the dispersion obeys a power-law dispersion, with both convection and diffusion contributing to the dispersion. In the present study, the finger structure was both related to the Rayleigh number and affected by transverse dispersion. The transverse dispersion between the downward and upward flow regions led to the interaction and merging of the adjacent fingers. This strongly affected the decay of the finger-number density.

From the profiles of the finger-number density shown in Fig. 3-6, we assumed the following exponential decay of finger-number density with time:

$$-\frac{dN}{dt} = \alpha N\,, \tag{3-8}$$

where the decay coefficient α ($\alpha = -\partial(\ln N)/\partial t$) was evaluated by fitting the plot of ln N against t. The α has units of s^{-1} in equation (3-8) under appropriate dimensional consideration; thus, $\alpha = cD_T/H^2$ was assumed, where c is a dimensionless coefficient, which can be estimated by fitting the plot in Fig. 3-9. As shown in Fig. 3-9, the decrease in the rate of finger-number density (α) increased linearly with the transverse dispersion coefficient. The finger-number density is in an exponential relationship with the transverse dispersion coefficient:

$$N \propto \exp(-369.74\frac{D_T}{H^2}t),\ r^2 = 0.90\ . \tag{3-9}$$

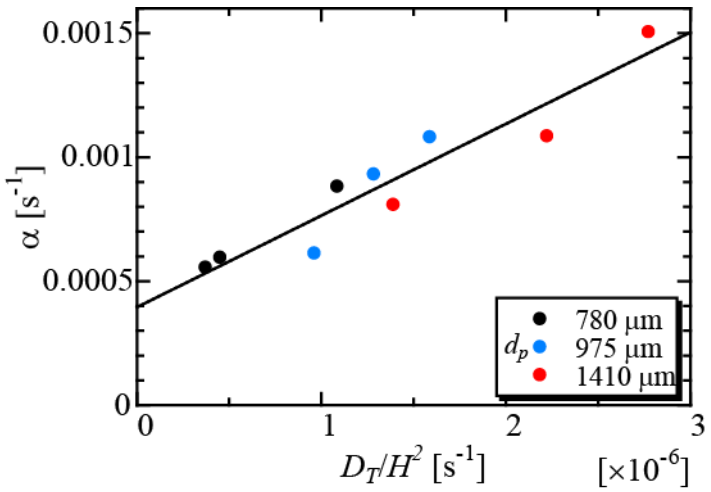

Fig. 3-9. Effect of transverse dispersion on the decay in finger number density. α is defined as the rate of the decrease in finger-number density.

In the course of convective mixing, high concentration fingers interact and merge with neighboring fingers (Fig. 3-2). The dispersion between the upward and downward flows causes an increase in finger diameter and prompts the coalescence of fingers, decreasing the finger-number density. The enhanced transverse dispersion at higher convection speeds increases the rate of decay of the finger-number density.

Nakanishi et al. (2016) performed the density-driven natural convection associated with Rayleigh-Taylor instabilities in three-dimensional porous media and presented that, for similar *Ra*, increased transverse dispersion enhances the broadening of the finger diameters and increases the coalescence of the fingers. Moreover, with transverse dispersion, the fingertips reach the bottom of the packed bed faster compared to cases without transverse dispersion. According to their experimental results, when $Pe < 10$, the effect of the transverse dispersion on fingering behaviors was negligible. The finger extension velocity, mass transfer rate and onset time scales with *Ra* with a characteristic length of *H* which is the height of the porous media. When $Pe > 10$, transverse dispersion affects the finger structures significantly. The fingering behavior is not only related to *Ra* with *H* as the characteristic length, but also affected by *Pe* with d_p as the characteristic length, which is consistent with the results in present study.

In addition, Heller (1966) demonstrated that the amplification factor decreased with Rayleigh number with the thickness of interface as characteristic length by a Linear Stability Analysis (LSA) for porous media. Using LSA, Graf et al. (2002) showed that the amplification factor (the maximum eigenvalue) for a Hele-Shaw cell decreased with increasing interface thickness. Wang et al. (2018) performed some experiments in Rayleigh-Taylor convection between NaI brine and water to investigate the effects of the thickness of the interface (δ) on the onset time. The results illustrated that the increasing the interface thickness delayed the onset of convection, while the finger extension velocity remained the same. Therefore, the onset time of natural convection is related to *Ra* with a characteristic length of the interface thickness.

3.6 Mass flux

To calculate mass transfer, a cylindrical control volume was added to the porous medium below the plane of the initial interface. Based on the local concentration of NaI, the mass of NaI in the control volume was evaluated at each time step. From the change in the mass, the mass flux *F* was estimated for each Rayleigh number. When the fingers reached the bottom surface of the porous medium, the maximum mass flux was observed for

porous media with permeability values k = 2.63 × 10^{-10} and 4.87 × 10^{-10} m^2. After this point, the intensity of the convention slowed. In the case of the porous medium with a permeability of k = 8.24 × 10^{-10} m^2, the mass flux showed no clear peak until the interface between the MEG-NaI and NaCl solutions collapsed. For reference, the mass flux can be estimated using the time taken for the fingers to reach the bottom surface of the porous medium. The dimensionless flux, i.e., the Sherwood number, is defined as a ratio of the mass transfer rate enhanced by convection to the mass transfer rate enhanced by diffusion:

$$Sh = \frac{F}{\varphi \Delta c D_m / H}, \tag{3-10}$$

where Δc is the concentration difference of iodide between the MEG-NaI mixture and NaCl solution at representative density levels (Fig. 2-1). We used a constant value of Δc = 110 kg/m^3 for simplicity.

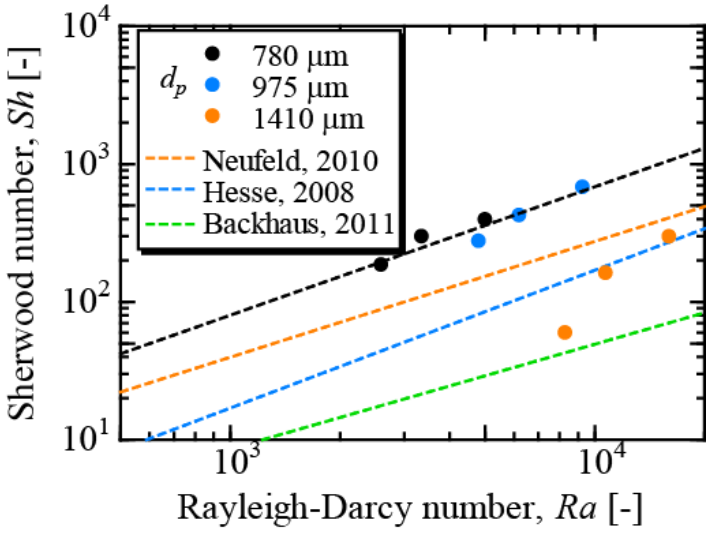

Fig. 3-10. Relationship between the Rayleigh number and the Sherwood number. Experimental measurements for porous media of permeability k = 2.63 × 10^{-10}, 4.87 × 10^{-10}, and 8.24 × 10^{-10} m^2 are shown by black, blue, and orange solid circles, respectively. The black dashed line denotes the power-law relationship [Eq. (3-11)]. Correlations proposed by Neufeld et al. (2010), Hesse (2008), and Backhaus et al. (2011) are also plotted.

As shown in Fig. 3-10, the dimensionless flux obtained in the porous media with permeability values k = 2.63 × 10^{-10} and 4.87 × 10^{-10} m^2 was correlated with the Rayleigh number by a power-law relationship:

$$Sh = 0.13 Ra^{0.93}, \; r^2 = 0.90. \tag{3-11}$$

However, the mass flux at a permeability of $k = 8.24 \times 10^{-10}$ m^2, which was used as a reference, deviated from the straight line [Eq. (3-11)] because the mass flux showed no clear peak until the interface between the MEG-NaI and NaCl solutions collapsed, as noted above. Moreover, enlargement of the permeability resulted in a decrease in the critical wavelength $\lambda_c = 96.23\, \varphi\mu D / k\Delta\rho g$ (Xu et al., 2006). At a high permeability of $k = 8.24 \times 10^{-10}$ m^2, the critical wavelength was estimated to be lower than the average particle diameter, suggesting that the onset of convective mixing may differ from that observed at low permeability.

The mass flux through the fingers into the lower cylindrical region is given by $c_f v_D A_D/(A_D+A_U)$, where A_D and A_U represent the area of the fingers and the NaCl flows, respectively, and c_f is the NaI concentration in downward fingers with velocity v_D ($v_D = v$) in the mixing layer. From the horizontal cross-sectional CT images, binarized into a visualization of the fingers and NaCl flows, the area of the descending fingers A_D and the area of upward NaCl solution flows A_U can be estimated. At the early stage, $c_f = \Delta c$, the ratios of $A_D/(A_D+A_U)$ were similar at all *Ra* values, in the range 0.33–0.38. Therefore, the increase in finger-extension velocity was attributed to an increase in mass flux. Since, as shown in Fig. 3-3, the finger-extension velocity increased in line with *Ra*, there is a power-law relationship between the dimensionless flux and *Ra*, as shown in Fig. 3-10.

Based on two-dimensional laboratory experiments and high-resolution numerical simulations, Neufeld et al. (2010) proposed that the dimensionless flux is related to the Rayleigh number by a power-law relationship with power of 4/5. Hesse (2008) and Pau et al. (2010) performed numerical analyses of two-dimensional and three-dimensional natural convection and suggested that the mass flux is given by $F = 0.017\, kC_0\Delta\rho g/\mu$. Backhaus et al. (2011), on the basis of two-dimensional experiments in Hele-Shaw cells using propylene glycol and water, suggested that the mass flux is proportional to the Rayleigh number by a power of 0.76. As shown in Fig. 3-10, the dimensionless flux (*Sh*) in the present experiments was higher than those previously reported (Backhaus et al., 2011; Hesse, 2008; Neufeld et al., 2010), but the gradient of the power law fitting the dashed line was in line with previous results.

Experimental studies using model fluids with a nonlinear density profile (Backhaus et al., 2011), including the present study, suggest that the dimensionless flux is strongly affected by the value of the concentration difference Δc and the molecular diffusion coefficient, which depends on the concentration. Most of the difference in the reported dimensionless fluxes may be attributed to the inaccurate evaluation of these parameters. In addition,

Hewitt et al. (2014) showed from Hele-Shaw cell experiments and numerical simulations that interfacial deformation can dramatically enhance the convective flux. Pau et al. (2010) also showed that the mass flux in three-dimensions is 25% higher than in a comparable two-dimensional simulation. Hidalgo et al. (2012) reported that the mixing rate exhibits a strong dependence on the shape of the density-concentration curve. In the case of numerical simulations of density-driven convection, because of the boundary condition $\vec{U} = 0$, $c = c_s$ at the top boundary $z = 0$, where c_s is the solubility of CO_2 in brine and the concentration difference Δc is constant, the boundary layer where the mass transport is limited by molecular diffusion is established on it.

3.7 Summary

A novel experimental scheme of three-dimensional imaging of density-driven natural convection in a porous medium was presented in this chapter. Several fluid pairs were used in the experiments to change the Rayleigh number over the range 2600–16000. The characteristics of fingering and the effect of the transverse dispersion on finger structure were investigated.

Slight fluctuations that appeared on the interface grew into large fingers, which interacted and merged with neighboring fingers. The fingers extended vertically downward without changing their locations, forming a columnar structure. The finger-extension velocity increased in line with the Rayleigh number and correlated with the characteristic velocity at a coefficient of 0.35. The transverse dispersion coefficient was estimated from the local concentration in the fingers provided by the three-dimensional images. The experimental results demonstrated that transverse dispersion was enhanced as the strength of density-driven natural convection increased. The decrease in figure-number density was related to the Rayleigh number and also affected by transverse dispersion. The finger-number density was in an exponential relationship with the transverse dispersion coefficient. The strength of transverse dispersion between the downward and upward flow regions significantly affected the decay of the finger-number density because of the interaction and merging of fingers.

The dimensionless mass flux, i.e., the Sherwood number, correlated with the Rayleigh number in a power-law relationship. The Sherwood number obtained by the model in this study was higher than that from two-dimensional experiments and high-resolution numerical simulations of density-driven natural convection, but the gradient of the power law fitting was consistent with previous results.

The findings, based on three-dimensional experiments in a porous medium, provide new insights, elucidating the behavior of CO_2 migration. They may contribute to the large-scale implementation of CO_2 storage and the evaluation of long-term security.

Chapter 4: Effect of layered heterogeneity on fingering structure

4.1 Experimental setup and procedures

In this chapter, density-driven natural convection between miscible fluids with a nonlinear density property in porous medium with homogeneous and heterogeneous layered structure was visualized. The plastic resin particle with different average diameter had been packed stratified as a heterogeneous porous medium. Plastic beads were packed in an acrylic resin tube with an inner diameter of 70 mm and height of 75 mm. To eliminate sorting of the particles on a tube wall resulting in a high porosity and permeability layer, fine particles with an average diameter of 215 μm (180−250 μm) were packed around the wall with a thickness of approximately 3 mm. Two difference sized particles were packed as layer 1 and layer 2 respectively, with a height of 22.5 mm for each layer. Then the two layers were saturated with NaCl solution by using a vacuum chamber. The particles, with the same size as layer 1, saturated with MEG-NaI were placed manually as layer 0 with a height of 30 mm on top of layer 1, as shown in Fig. 4-1.

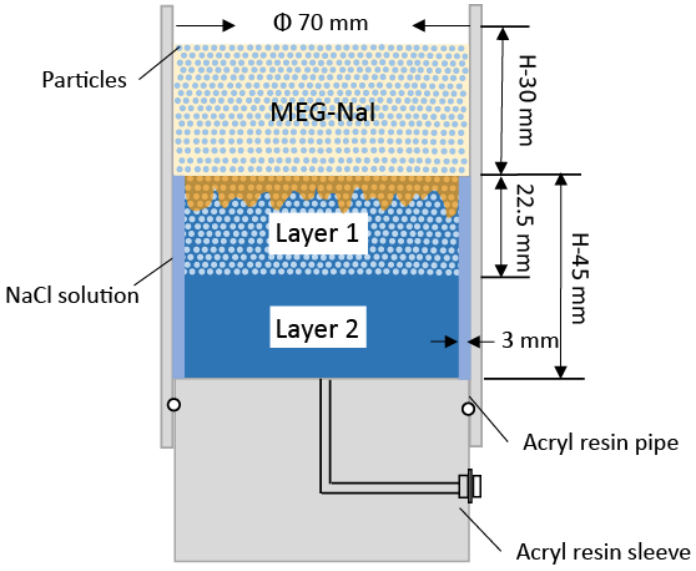

Fig. 4-1. Schematics of packed bed of particles

We used three average-diameter plastic beads, d_p = 975 μm, d_p = 780 μm, and d_p = 647 μm, to vary the permeability related to the Rayleigh number. The details of the layer structure are shown in Table 4-1. A certain weight of particles were packed in each layer

Note: This chapter has been published as: Wang Lei, Nakanishi Y., Hyodo A., Suekane, T., Three-dimensional finger structure of natural convection in homogeneous and heterogeneous porous medium, Energy Procedia, Vol. 114 (2017), 5048-5057.

for maintaining the same porosity and permeability in different experiments. Fluid pair A and B (the details in Table 2-1) were utilized for modeling the density-driven natural convection. The properties of the porous medium are summarized in Table 4-2.

During the convective mixing process, the entire packed beads' bed was scanned with the X-ray CT scanner. The reconstructed images consist of 496 image slices with a resolution of 496×496 pixels and 201 μm/pixel in all directions. Until the natural convection is completed, the scanning repeated every 75 s.

Table 4-1. Layer structure.

	Particle diameter, d_p [μm]	
	Layer 1	Layer 2
Homogeneous structure	975	975
	780	780
	647	647
Heterogeneous structure	975	647
	780	647
	647	975
	647	780

Table 4-2. Properties of the porous medium.

Average particle diameter d_p [μm]	Permeability k [m^2]	Porosity φ [-]	Fluid pair	Rayleigh number Ra [-]
647	9.51×10^{-11}	0.49	A	1810
			B	1210
780	2.63×10^{-10}	0.49	A	5010
			B	3360
975	4.87×10^{-10}	0.49	A	9290
			B	6220

4.2 Changing of fingering structure at different permeability layers

The development of fingers due to density difference in three-dimension is shown in Fig. 4-2. At the early stages, Fig. 4-2 (a) 75 s and (b) 150 s, slight fluctuations appear at the initial interface between MEG-NaI and NaCl solutions. With the growth of wavelength,

dense concentration fingers form and extend vertically downward and eventually reach the bottom of the packed bed at 1725 s for the layered structure in Fig 4-2 (a) and 2175 s for the layered structure in Fig 2 (b). During the convective mixing process, the same as the homogeneous porous medium, mentioned in chapter 2, fingers coalesce and merge with the adjacent fingers, growing in diameter, also shielding hinders the growth of short fingers, which are caught up in shielding fingers. When fingers pass through the interface between layer 1 and layer 2, in Fig. 4-2 (a), the particle diameter of layer 2 is smaller than that of layer 1, and the permeability becomes lower, the finger diameter increases. On the other hand, in Fig. 4-2 (b), the particle diameter of layer 2 is larger than that of layer 1, when fingers pass through the interface with an increasing permeability, the finger diameter decreases. After that, these fingers extend downward, the finger-extension velocity, the number of finger and the concentration in fingers change as well, the details are to be mentioned later.

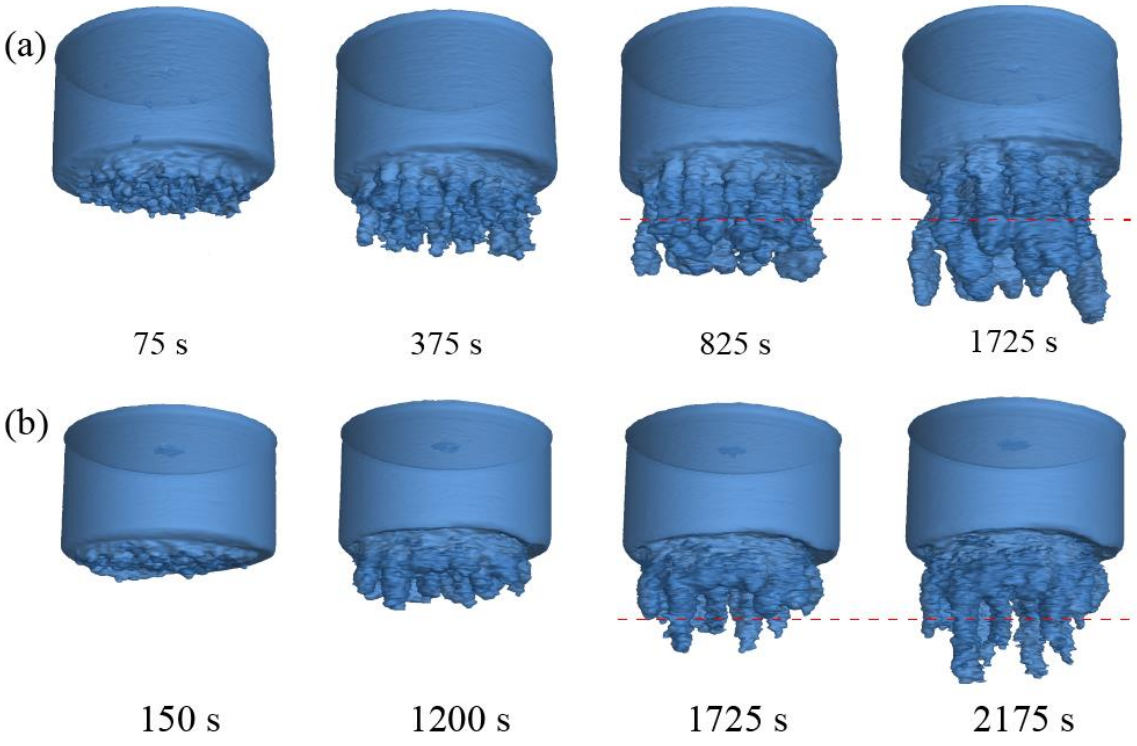

Fig. 4-2. Development of three-dimensional finger structure in the porous medium with the layered structure. (a) The particle diameter is d_p = 975 μm and 647 μm and the Rayleigh number is Ra = 9290 and 1810 for the layer 1 and the layer 2, respectively. (b) The particle diameter is d_p = 647 μm and 975 μm and the Rayleigh number is Ra = 1810 and 9290 for the layer 1 and the layer 2, respectively. Blue indicates the iso-contour surface at the concentration of 16.6 kg/m^3 of MEG-NaI solution. The red dashed line shows the interface between layer 1 and layer 2.

4.3 Finger-extension velocity

The finger-extension velocity can be estimated from the distance of proceeding finger tips over a certain time interval. During the process of natural convection, each finger may have different extension velocity, here, we choose a finger extending more quickly as the sample to estimate the finger-extension velocity. Fig. 4-3 plots the finger-extension velocity against the time both in homogeneous structure and heterogeneous layered structure. Note that Fig 3 does not show the finger-extension velocity at t < 75 s. Linear stability analysis (Ennis-King & Paterson, 2005; Xu et al., 2006) suggest that the onset time is related to the properties of fluid system. Under experimental conditions in present study, the onset time is in a range of 2.9-75.3 s, which is shorter than the time required to manually place the particles on layer 0 (about 70 s) and to complete a CT scan. So it is impractical to study the effect of onset time and we define the time at the starting of the first CT scan as t = 0 s.

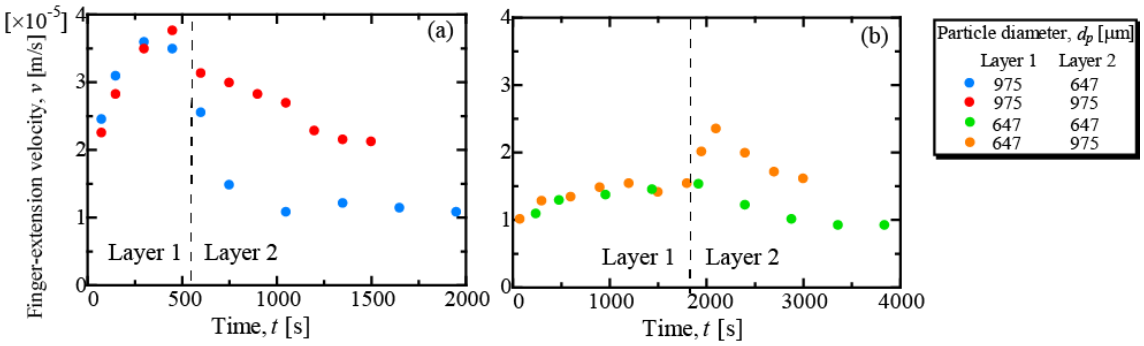

Fig. 4-3. Comparison of finger-extension velocity for each time steps in homogeneous and heterogeneous porous medium. (a) Homogeneous structure (layer 1, 975 μm; layer 2, 975μm) and heterogeneous layered structure (layer 1, 975 μm; layer 2, 647μm). (b) Homogeneous structure (layer 1, 647 μm; layer 2, 647 μm) and heterogeneous layered structure (layer 1, 647 μm; layer 2, 975μm).

In Fig. 4-3, the layered structure has no significant influence on the finger-extension velocity in layer 1. The finger-extension velocity has the same gradient for homogeneous structure and heterogeneous layered structure, increasing with time. When the finger passes through the interface and extends into layer 2 with a decreasing particle diameter, the finger-extension velocity decreases with time, then reaches to a fixed value of 1.08×10^{-5} m/s, as shown in Fig. 4-3(a). On the other hand, as seen in Fig. 4-3(b), when the finger extends into layer 2 with an increasing particle diameter, the finger-extension velocity increases because of the increase in permeability, then decreases gradually to the

value of 1.61×10^{-5} m/s, which is smaller than that of in homogeneous structure (the red points in Fig. 4-3a). The increasing of finger-extension velocity in layer 2 enhances the dispersion between downward convective fingers and upward flows. Therefore, the concentration in fingers is reduced due to the dispersion, making the finger-extension velocity decreases gradually with time.

4.4 The characteristics of fingers in heterogeneous layered structure

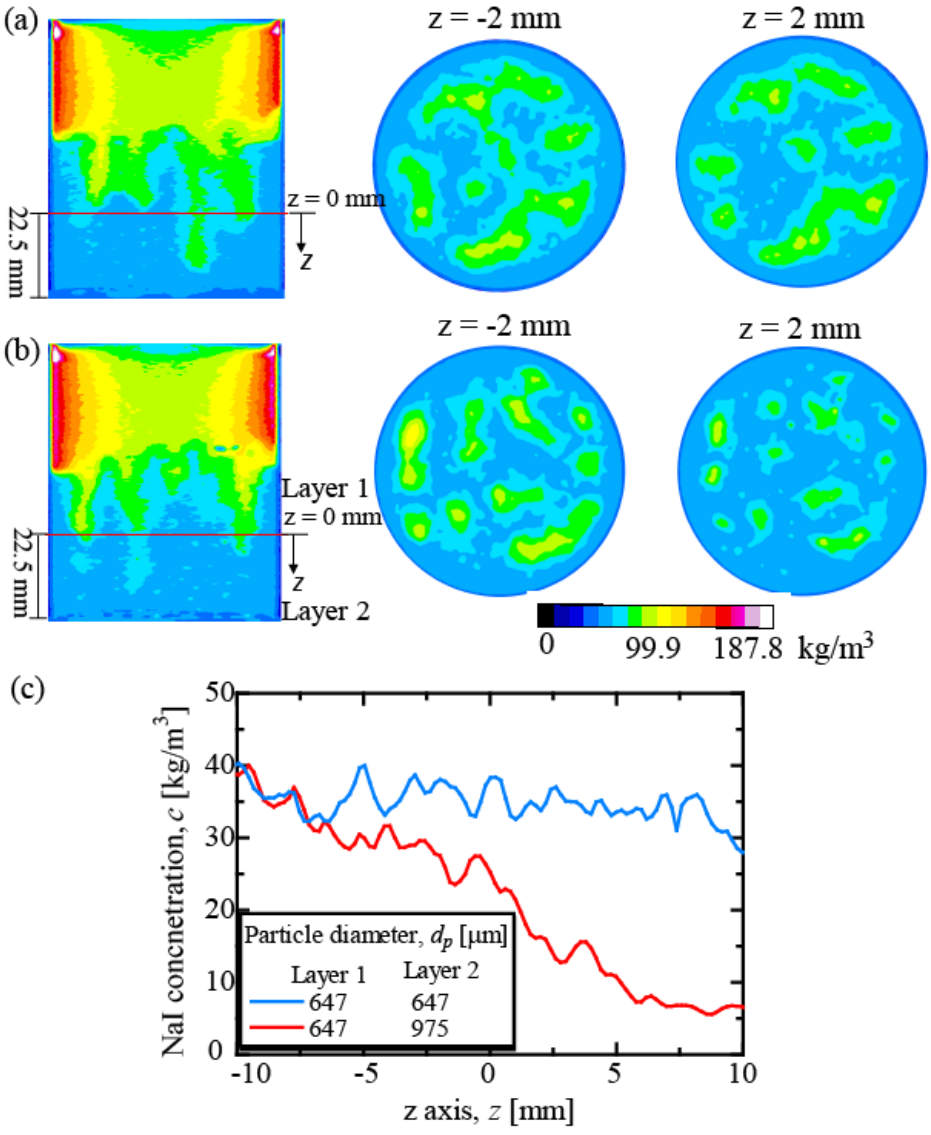

Fig. 4-4. Change in the properties of fingers passing the interface of layered structure. Distribution of NaI concentration in vertical cross-section and horizontal cross-section 2 mm above and below the interface for (a) homogeneous structure (Layer 1, 647 μm; Layer 2, 647 μm) and for (b) increasing particle diameter (Layer 1, 647 μm; Layer 2, 975 μm). (c) Distribution of NaI concentration along the axis of a representative finger passing the interface with an increasing particle diameter.

Fig. 4-4 shows distribution of NaI concentration in fingers passing through the interface of the layered structure with an increasing of particle diameter. Here *z*-axis runs in the direction of gravitational acceleration and z = 0 mm is the interface between layer 1 and layer 2. In the case of homogeneous structure (Fig. 4-4a), the fingers remain horizontal location and the diameter of fingers are almost the same at 2 mm above and below the interface. The NaI concentration in a finger remains the same as well as shown in Fig. 4-4(c). On the other hand, in the case of heterogeneous layered structure with an increasing permeability, when fingers pass through the interface, the horizontal location of fingers and the number of the finger are unchanged (Fig. 4-4b), while NaI concentration in a finger decrease as well as the diameter of fingers reduces (Fig. 4-4c and 4-4b).

With the assumption of a steady state, mass conservation for a finger is described as $c_f v_f A = const.$, where c_f is the NaI concentration in downward fingers with velocity v_f, A is the cross sectional area of fingers. When fingers pass through the interface with an increase in particle diameter, the permeability increases and finger-extension velocity increases, the increasing velocity of fingers enhances the dispersion between downward fingers and upward flow regions. In addition, regarding the mass conservation, when finger-extension velocity increases, the cross sectional area of fingers decreases. Meanwhile, for the same time interval, the side area along the z-direction increases compared with the changing of cross-sectional area of fingers. Much more fraction of the mass supplied by the downward convection in fingers is lost through the side area by dispersion. The dilution of concentration crossing the side area is enhanced. Therefore, the NaI concentration in fingers decreases when fingers pass through the interface to a higher permeability layer.

Fig. 4-5 shows the influence of layered structure with a decreasing of particle diameter on the characteristics of convective fingers. When fingers extend from layer 1 with particle diameter of 975 μm to layer 2 with particle diameter of 647 μm, namely with a decreasing permeability, the distribution of NaI concentration for different time steps has been shown in Fig. 4-5(a). The horizontal cross-sectional images on top of Fig. 4-5(a) show the finger structure at the interface (z = 0 mm) and suggest that after finger tips passing through the interface, the diameter of fingers increases with time. According to the mass conservation mentioned before, when fingers pass through the interface with a decreasing permeability, finger-extension velocity decreases while the concentration in fingers cannot increase at the moment, leading to an increase in cross sectional area of fingers. For the same time interval, the changing of side area along the z-direction is less

than the increasing of cross-sectional area of fingers. In addition, since the finger extension velocity decreases after extending into layer 2, the gradient of the velocity between downward fingers and upward flows decreases. Therefore, the weakened dispersion in shear flow has a limited influence on NaI concentration. The NaI concentration distribution is similar to homogeneous structure, remaining around 35 kg/m^3, as shown in Fig. 4-5(b).

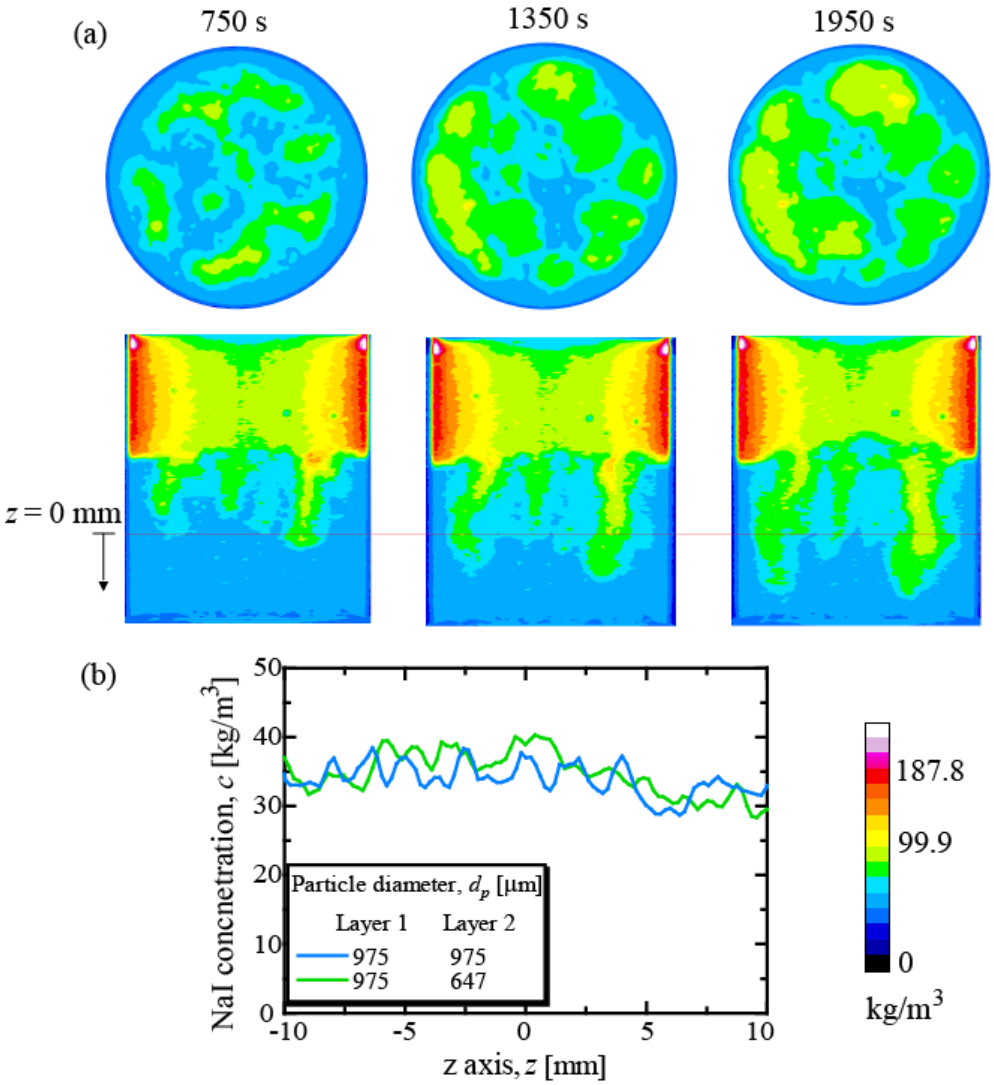

Fig. 4-5. Effect of the interface of the layered structure of a porous medium with a decreasing permeability along a finger extension direction on NaI concentration in fingers. (a) Evolution of distribution of the NaI concentration in a horizontal cross-section at the interface and a vertical cross-section (Layer 1, 975 μm; Layer 2, 647 μm). (b) Distribution of NaI concentration along the axis of a representative finger.

4.5 Summary

In reservoir, stratigraphic structure has a heterogeneity, which is composed of alternating layers, reflecting an isotropic property in the horizontal direction and different permeability in the vertical direction. In this study, the plastic resin particle with different average diameter has been packed stratified as a heterogeneous porous medium. Density-driven natural convection between miscible fluids with a nonlinear density property in porous medium with homogeneous and heterogeneous layered structure is visualized three-dimensionally by means of a micro-focused X-ray CT scanner. Three-dimensional finger structure and local NaI concentration in fingers can be obtained on the basis of CT images.

In the heterogeneous layered structure, when convective fingers pass through the interface to a higher permeability layer, the finger-extension velocity increases and the diameter of fingers decreases. The enhanced dispersion between downward fingers and upward flow regions leads to a decreasing of concentration in fingers. On the other hand, when fingers pass through the interface to a lower permeability layer, the finger-extension velocity decreases. The weakened dispersion has a limited influence on the distribution of concentration in fingers, thus, the concentration in fingers remains and the diameter of the fingers increases. These results suggest that the concentration in the finger changes nonlinearly against the permeability.

The layered heterogeneous structure hinders the development of natural convection. In the heterogeneous layered structure, as finger passing through the high permeability layer, finger-extension velocity is reduced by a dilution of finger concentration. Therefore, the development of natural convection in the layered heterogeneous structure becomes slower than that in the homogeneous structure.

Chapter 5: Gravitational fingering due to density increase by mixing at a vertical displacing

The density increase from CO_2 dissolution in oil creates an unstable high-density layer and leads to gravitational fingers, which may have a significant effect on the mixing and flow path. Although the viscosity ratio in CO_2 injection scenario is unstable, and the viscos fingering could occur when injection rate is higher than critical velocity, I focus on the effect of density increase on fingering structure in this work. Therefore, in these experiments, during the injection process, the viscosity ratio is stable, and the displacement front is always stable with respect to injection speed, having no effect of viscous fingering. In this chapter, the gravitational fingering during injection was modelled by a miscible fluid pair with nonlinear density property, and the properties of the fingering resulting from the density increase by mixing in porous media using three-dimensional X-ray CT was investigated. The key measures of gravitational fingering during the injection process — the finger extension velocity, finger number density, mixing length of fingers, and relative volume of fingers — were compared at different Péclet numbers by changing the permeability of the porous media and the injection speed.

5.1 Experimental method

The experiments were conducted using the following procedures. First, as a porous medium, plastic beads were packed in an acrylic resin tube with an inner diameter of 70 mm and height of 55 mm (Fig. 5-1). To eliminate sorting of the particles on a tube wall resulting in a high porosity and permeability layer, fine particles with an average diameter of 215 μm (180−250 μm) were packed around the wall with a thickness of approximately 1.5 mm. The packed beads were saturated with NaCl solution in a vacuum chamber. Next, after removing the top sleeve of the bed of packed beads, MEG–NaI saturated particles were manually placed on top of the tube, 15 mm above the particles saturated with the NaCl solution. Then, the sleeve was replaced again while inserting a distributor. A plastic filter plate was placed at the exit of the packed bed to facilitate uniform drainage. Then, MEG–NaI solution was injected into the packed bed vertically downward with respect to the gravitational acceleration at three different constant injection speeds using a syringe pump (KD Scientific, KDS100), and the entire packed bed was scanned by the X-ray CT scanner for a specific time interval. For each experiment, the Péclet number $Pe = (v_0 d_p/\varphi D)$

Note: This chapter has been published as: Wang Lei, Cai S., Suekane, T., Gravitational fingering due to density increase by mixing at a vertical displacing front in porous media, Energy and Fuels, Vol. 32(1), (2017), 658-669.

was varied from 0.71 to 3.59 (Table 5-1), where v_0 is the injection speed and D is the molecular diffusion coefficient of NaI.

Table 5-1. Range of Péclet number in experiments.

Run #	Average particle diameter d_p [μm]	Injection speed v_0 [m/s]	Péclet number Pe [-]	Rayleigh number Ra [-]
1 A	647	1.08×10^{-6}	0.71	1059
1 B		1.81×10^{-6}	1.19	
1 C		3.61×10^{-6}	2.38	
2 A	780	1.08×10^{-6}	0.86	2940
2 B		1.81×10^{-6}	1.44	
2 C		3.61×10^{-6}	2.87	
3 A	975	1.08×10^{-6}	1.07	5442
3 B		1.81×10^{-6}	1.80	
3 C		3.61×10^{-6}	3.59	

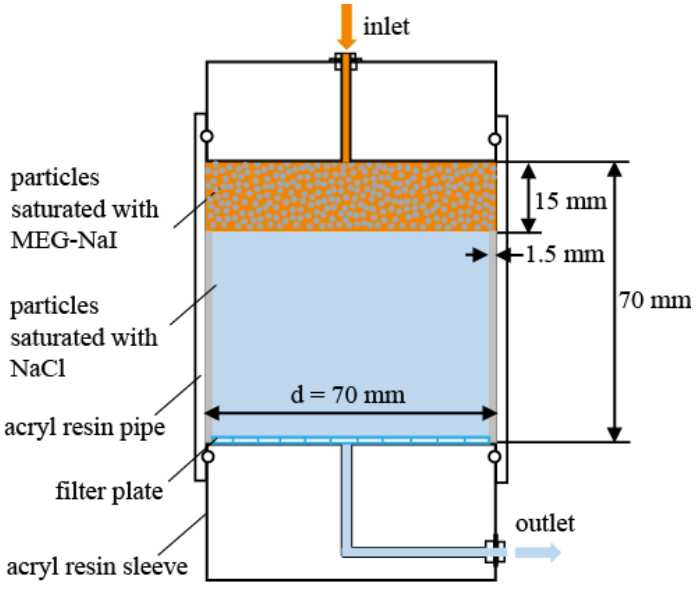

Fig. 5-1. Packed bed of melamine resin particles.

In these experiments, the reconstructed images comprised 496 image slices of 496 × 496 pixels with a resolution of 171 μm/pixel. It takes approximately 70 s to scan 496 images of the entire packed bed from all directions, and takes 60 s to turn back to its original

position for next scan, considering the packed bed was connected with the injection tube. During the injection process, the scans were repeated every 150 s until the extended fingers reached the bottom of the packed bed.

A number of other studies have been performed based on the assumption that when the injected CO_2 is lighter than the oil, the CO_2 injection is a stable gravity drainage process (Bangia et al., 1993; Cardenas et al., 1984; Moore, 1986; Palmer, Nute et al., 1984). To clarify the effect of density increase on the fingering structure during the injection process, the injection experiment using a fluid pair without density increase was performed, namely, the fluid mixture did not exhibit an increase in density upon mixing. The density effect describes that the density increase from CO_2 dissolution in oil creates an unstable high-density layer and leads to gravitational fingers, which may have a significant effect on the mixing and flow path of injected CO_2.

Table 5-2. Fluid properties.

	Fluid pair	Density [g/cm^3]	Viscosity μ [mPa·s]	Viscosity ratio [-]	Initial density difference $\Delta\rho$ [g/cm^3]
B	MEG–NaI solution (displacing fluid)	1.050	3.193	3.044	0.004
	NaCl solution (displaced fluid)	1.054	1.049		
D	Glycerine solution (displacing fluid)	1.073	2.698	3.076	0.005
	NaI + NaCl solution (displaced fluid)	1.078	0.877		

In this experiment, 31 wt. % glycerine solution and 1 wt. % of NaCl was added into 10 wt. % NaI solution (NaI+NaCl) to match the viscosity ratio and initial density difference of fluid pair D with that of fluid pair B, as shown in Table 5-2. Lighter glycerine solution was injected into a packed bed saturated with heavier NaI + NaCl solution under the same experimental conditions as fluid pair B. Without the density effect, there was no fingering (Fig. 5-2). The blue part at the top represents the particles that are saturated with 31 wt. % glycerine solution, while the green-yellow part at the bottom represents the particles that are saturated with 10 wt. % NaI solution doped with 1 wt. % NaCl. Fig. 5-2 illutrates the time evolution of the interface variation, when a lighter glycerine solution is injected into a packed bed saturated with heavier NaI + NaCl solution. During the injection process, no occurrence of fingering. Further, the interface moves downward in a piston-like

displacement manner without displaying any instability, which indicates that the injection process has no significant effect on the formation of fingers. However, the density increase from CO_2 dissolution in oil may have a significant effect on the mixing and flow path (Ahmed et al., 2012; Farajzadeh, n.d.; Firrozabadi & Cheng, 2010; Shahraeeni et al., 2015). In this chapter, the density increase effect during the injection process was examined using a fluid pair (MEG–NaI and NaCl solution) with a nonlinear density property.

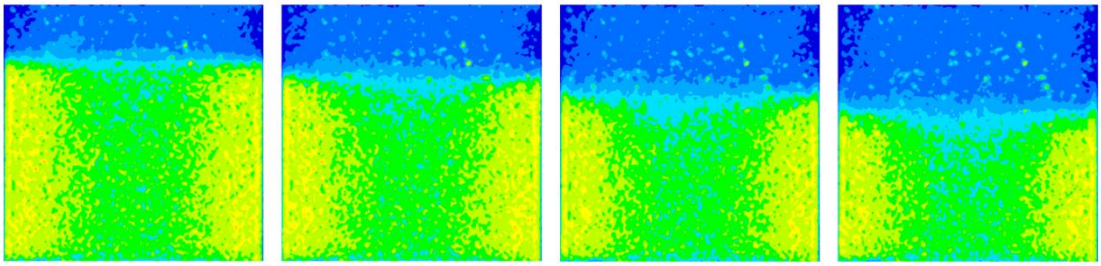

Fig. 5-2. Visualization of interface variation during the injection process without any increase in density at Péclet number of 3.59. The blue part represents the particles that are saturated with 31 wt. % glycerine solution, and the green-yellow part represents the particles that are saturated with 10 wt. % NaI solution doped with 1 wt. % NaCl.

5.2 Three-dimensional finger structure during injection process

Fig. 5-3 shows the different stages of the development of the fingering structure during the injection process in the packed bed that developed upon mixing the MEG–NaI solution in the NaCl solution. At the early stage immediately after injection, when the MEG–NaI solution started to mix with the NaCl solution, a thin mixing layer formed, became larger over time, and was destabilized in a few seconds, yielding nascent denser fingers sinking from the initial interface (left images in Fig. 5-3). Over time, the fingers grew and extended in the main flow direction with some nonlinear effects, such as merging between neighboring fingers. The diameters of these fingers increased with time via diffusion and coalesced with each other. At times after injection of 1800 s (Fig. 5-3a and 5-3b) and 1200 s (Fig. 5-3c), the tip of the most advanced finger reached the end of the packed bed.

From Fig. 5-3, it is clear that the extension and morphology of fingers differ for different Péclet numbers. The intensity of mixing of the displacement front affects the fingering.

Although the structure of the fingers was roughly the same for each Péclet number condition, the fingers extended much faster for higher Péclet numbers (Fig. 5-3c). In the higher Péclet number case, the fingers were thicker at the later stage and rapidly connected with neighboring fingers directly below the interface because of the enhanced mixing.

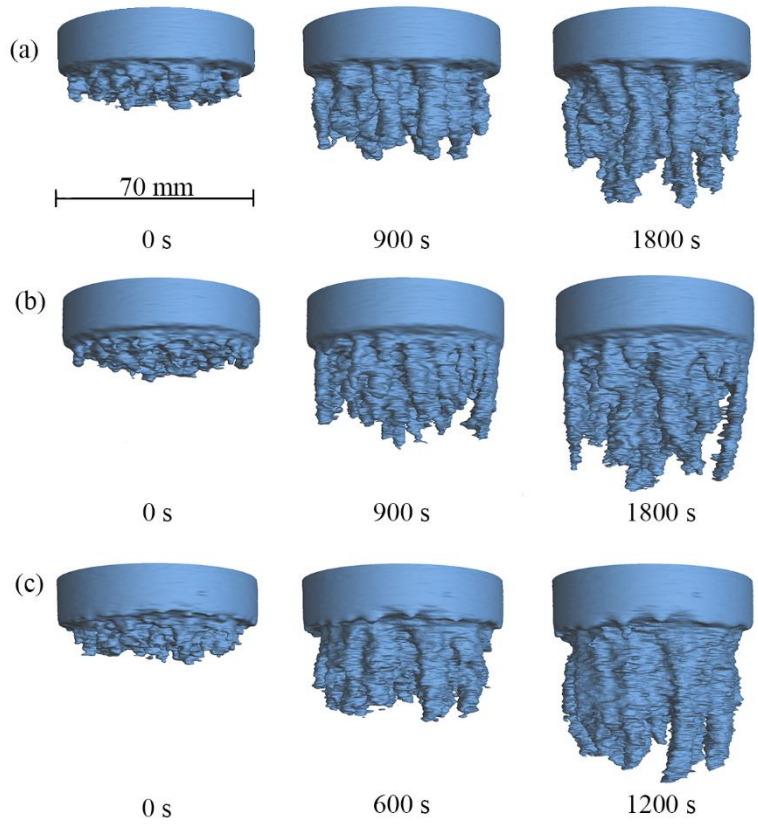

Fig. 5-3. Visualization of three-dimensional fingers at different time steps as a function of Péclet number: (a) Run # 3A, *Pe* = 1.07; (b) Run # 3B, *Pe* = 1.80; and (c) Run # 3C, *Pe* = 3.59. The blue color represents the iso-contour surface of an MEG–NaI concentration of 8.44 kg/m^3. The time shown at the bottom of each image is the starting time of each scan for different time steps.

5.3 Finger-extension velocity

The finger extension velocity (v) was estimated as a function of the distance of the finger front migration obtained from sequential CT images. Fig. 5-4 plots the finger extension velocity for all the experiments against Péclet number. With increasing Péclet number, the finger extension velocity increased. The finger extension velocity scales with Péclet number as $v = 1.8 \times 10^{-5} Pe^{0.71}$, $r^2 = 0.76$. For higher Péclet numbers, the mixing near the interface was enhanced, leading to an increase of the density difference between the heavy

fingers and surrounding water. The details of this investigation are described in section 5.4.

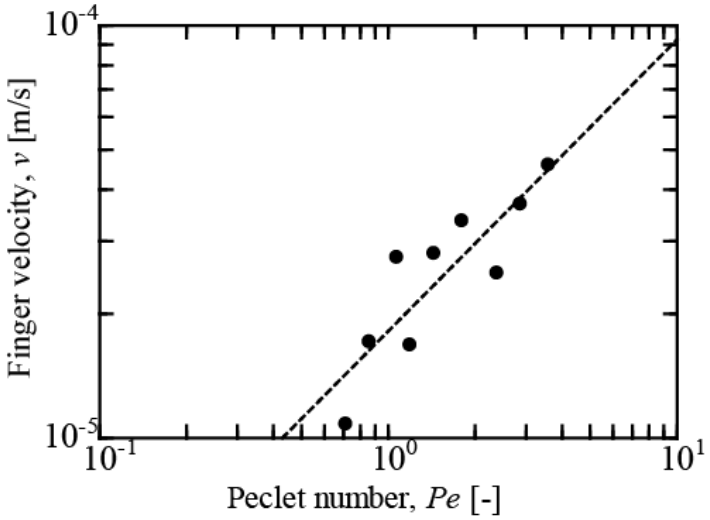

Fig. 5-4. Finger extension velocity as a function of Péclet number.

5.4 Distribution of NaI concentration in fingers

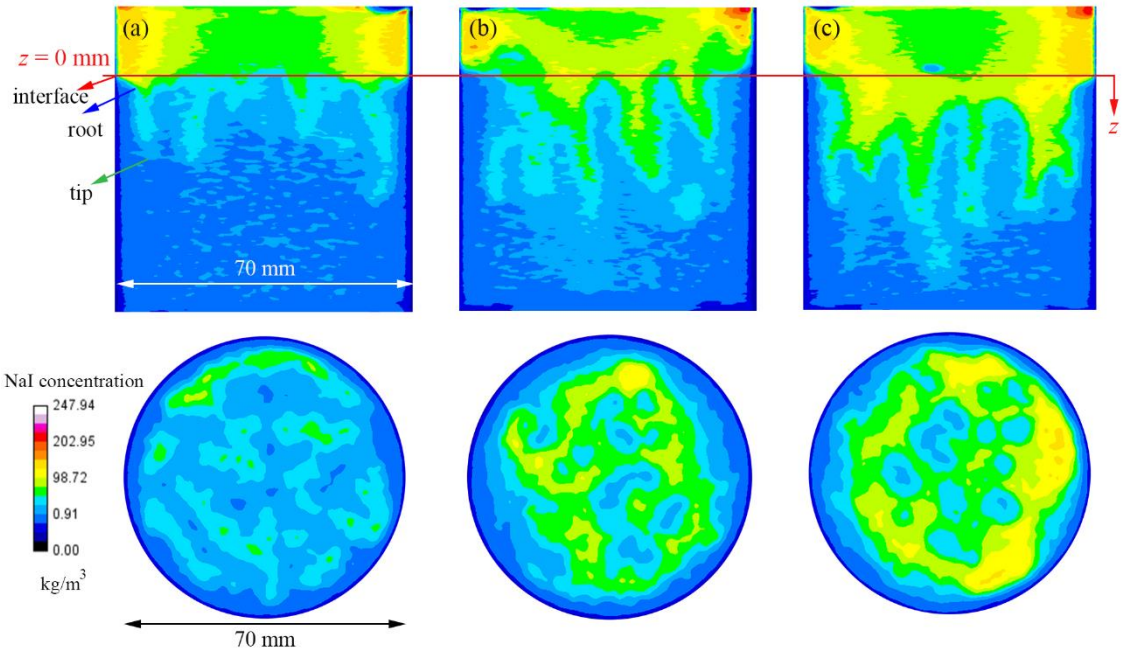

Fig. 5-5. Comparison of fingering structure and NaI concentration distribution in fingers at t = 1350 s for (a) Run # 2A, *Pe* = 0.86; (b) Run # 2B, *Pe* = 1.44; and (c) Run # 2C, *Pe* = 2.87. The bottom images show the fingering structures at *z* = 11 mm in horizontal cross-sectional images.

z = 0 is defined as the initial interface and the direction of gravitational acceleration is defined as the direction of the z-axis. Fig. 5-5 shows the distribution of the local concentration and fingering structure for different Péclet numbers at t = 1350 s for a vertical cross-section (top) and horizontal cross-section at 11 mm below the initial interface (z = 11 mm) (bottom). The red line represents the initial interface at z = 0 mm. For higher Péclet number, the finger penetration depth was larger at the same time. The local concentration in the fingers was relatively high because of enhanced mixing at higher injection speed. As observed in the bottom images in Fig. 5-5, at a low Péclet number of Pe = 0.86, fine fingers were scattered with a lower concentration. With increasing Péclet number, the fingers spread out and merged with neighboring fingers, resulting in a larger finger diameter; the local concentration at the center of the finger also increased.

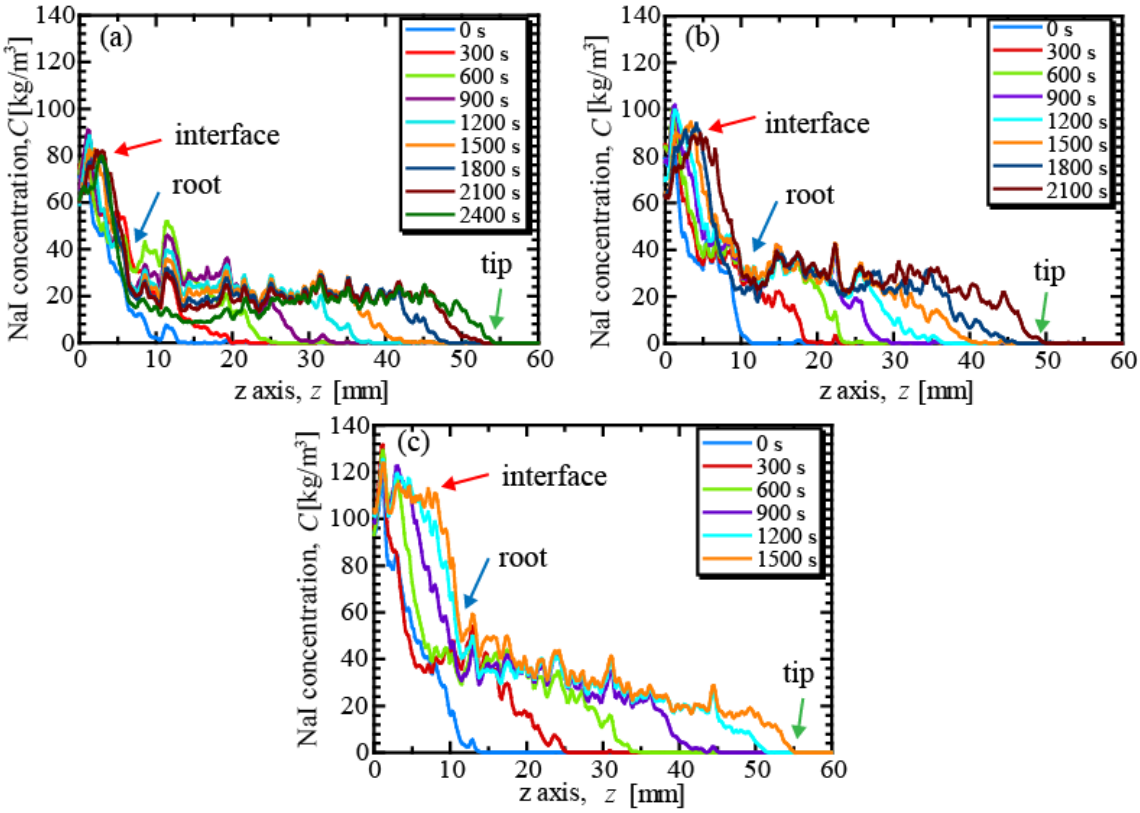

Fig. 5-6. NaI concentration distribution in an advanced finger: (a) Run # 3A, Pe = 1.07; (b) Run # 3B, Pe = 1.80; and (c) Run # 3C, Pe = 3.59.

Figure 5-6 shows the distribution of the NaI concentration along an advanced finger for different time steps. The interface is defined as the position, where NaI concentration in the finger begins to exhibit a sharp decline. The root of finger is defined as the turning

point at which the gradient of the distribution of NaI concentration is modified from a sharp decrease to a gradual one. The tip of the finger is defined as the furthest position where the finger extended along *z* axis. The NaI concentration decreased along the finger for different Péclet numbers; however, the gradient of the decrease became larger with increasing Péclet number. With increasing time, the tip of the finger descended downward and the initial interface moved downward. These changes became more significant at higher Péclet numbers.

Beam hardening can be reduced during the processing of the scanned data and image reconstruction, as mentioned in section 2. However, as depicted in Fig. 5-5, spurious concentration gradients occurred in the domain of displacing fluids above the interface, because of the beam hardening effect. Such an effect causes the edges of an object to be brighter than the center, even if the object consists of uniform material throughout. An X-ray beam contains polychromatic beams having a range of energy spectrum. When passing through an object, an X-ray beam is hardened since the low energy photons tend to be absorbed, which leaves only the high energy ones. Therefore, when an X-ray beam passes through a dense part, the low energy component of the X-ray spectrum is more easily attenuated or even completely adsorbed than its counterpart. In the reconstruction process, if a uniform attenuation is assumed for all the energy components of the X-ray spectrum, the edges of an object is reconstructed to be brighter than the center, resulting in a gradient in brightness in a radial direction (e.g. Fig. 5-7a).

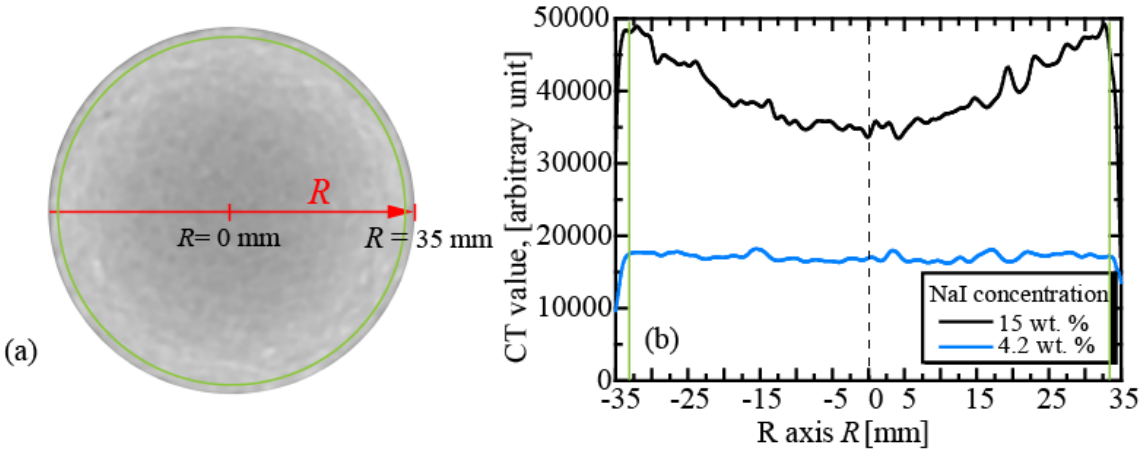

Fig. 5-7. (a) Horizontal cross-sectional image of packed bed with an average particle diameter of 975 μm saturated with 100 % MEG-NaI (15 wt. % NaI). (b) CT value distribution in *r*-direction along the red line in Fig. 9a. The black and blue lines present the cases of 15 and 4.2 wt. % of NaI concentrations, respectively. The green circle (a) and lines (b) denote the inner boundary of a fine particle layer.

The displacing fluid contains 15 wt. % of NaI, while the highest NaI concentration in the displaced fluid in the finger was observed to be 40 kg/m^3 (4.2 wt. % of NaI), as depicted in Figs. 5-5 and 5-6 among all experimental conditions. To estimate the beam hardening effect, the packed bed that was entirely saturated with 15 and 4.2 wt. % of NaI was scanned using an X-ray CT scanner having the same scanning parameters as depicted in Fig. 5-7. These concentrations of NaI are the most severe conditions, where the beam hardening effect is likely to occur for displacing and displaced liquids, respectively. Fig. 5-7a presents a horizontal cross-sectional image of the packed bed saturated using MEG–NaI, having a NaI concentration of 15 wt. %. The beam hardening effect induced the spurious concentration gradients in a radial direction. Fig. 5-7b depicts the CT value distribution in the *R*-direction, which is defined by the red line in Fig. 5-7a, for the NaI concentration of 15 wt. % and 4.2 wt. %. CT values range from 16300 to 18200 arbitrary units without a radial gradient, when the packed bed was saturated with 4.2 wt. % of NaI (blue line). The fluctuations in CT values originate from the particle impurities. In the displaced fluid region, the evaluation of local concentration of NaI with the CT value is justified because the beam hardening effect is negligible. Conversely, the beam hardening effect is not negligible in the region of the displacing fluid. The variation in the CT value is approximately 14000 arbitrary units from center to edge.

As mentioned above, in Fig. 5-6, the beam hardening effect affected only on the concentration distribution of the displacing fluids that were above the interface, while no effect on the concentration distribution of the fingers was observed.

Figure 5-8a compares the NaI concentration distributions in an advanced finger for different Péclet numbers at t = 1500 s. The concentrations in the root of the fingers for Pe = 1.07, 1.80, and 3.59 were approximately (green) 20, (red) 30, and (blue) 40 kg/m^3. The concentration of fingers above the interface as well as the concentration in the root of fingers increased with increasing Péclet number. The ratio of the concentration of the finger-root to that of the interface was estimated to be 0.25, 0.32, and 0.36 for Pe = 1.07, 1.80, and 3.59, respectively. Corresponding to the results in Fig. 5-8, based on the calibration curve (Fig. 2-3), the density difference of the root of fingers were estimated, as shown in Fig. 5-8b. The density differences between the finger and surrounding NaCl solution at the root of the fingers were 0.003, 0.007, and 0.02 g/cm^3, increasing with increasing Péclet number because of the change of the injection speed. This result is consistent with the previous observation in Fig. 5-5 and provides evidence of an increased finger extension velocity with increasing Péclet number as a result of the large density difference between the fingers and surroundings.

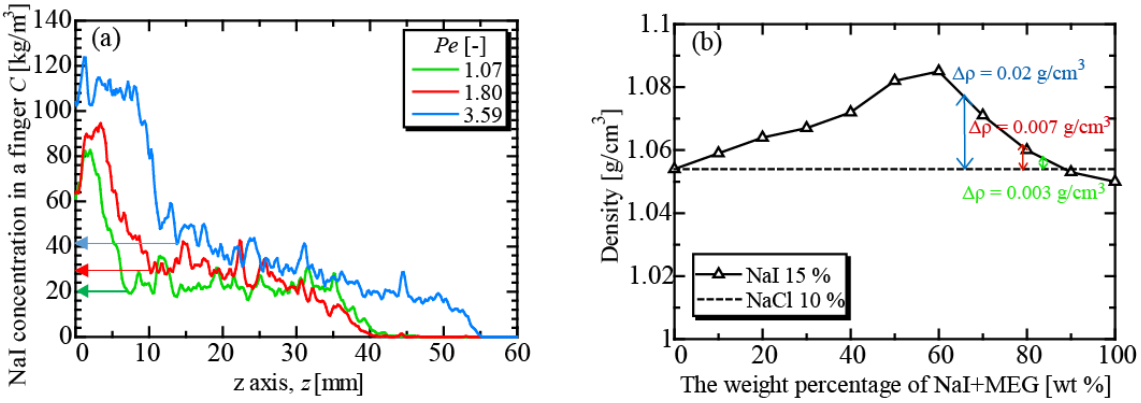

Fig. 5-8. (a) Comparison of NaI concentration distribution in an advanced finger for different Péclet numbers. (b) Nonlinear density profile of the mixture of MEG–NaI and NaCl solutions.

A characteristic velocity U is defined as $U = \frac{k}{\mu}\Delta\rho g$, representing the ideal Darcy velocity driven by gravity force with an initial density difference of Δρ between the MEG–NaI and NaCl solutions. There are two factors affecting the finger extension velocity, the permeability and density difference. The finger extension velocity increases with increasing Péclet number by increasing the permeability. For the case of a higher Péclet number by increasing the injection speed while keeping the permeability constant, the mixing near the interface is enhanced and high-concentration fingers form because of the density increase. These heavier fingers extend downward due to gravitational force, whereas the surrounding lighter NaCl solution floats upward. With increasing Péclet number, the density difference between the fingers and surroundings becomes larger, resulting in an increase of the finger extension velocity. In turn, the velocity of upward flow increases. As a result, the mixing near the interface become stronger.

The interface moves downward and travels by the distance $z^{'} = (v_0/\varphi)t$ for piston-like displacement without instability. The position of the traveling interface can be estimated based on the slice-averaged concentration of NaI (Fig. 5-9a), and the results are plotted as a function of time for different Péclet numbers in Fig. 5-9b. We define the position of the traveling interface z' for each time step as the position at which the average concentration c_w is equal to $0.5c_0$ (c_0 is the initial average concentration of the MEG–NaI solution). In Fig. 5-9b, the position of the traveling interface linearly increases with time associated with a coefficient (a) of 0.88, 0.85, and 0.85 for different Péclet numbers, which are almost the same. Without an increase in density during injection, there is no fingering. The interface should travel downward related to $(v_0/\varphi)t$ with a coefficient of 1.

However, the formation of fingering due to the density increase by mixing impedes the traveling of the interface, resulting in a <1. As discussed above, because of the enhanced mixing between downward-moving fingers and upward-moving surroundings by injection, the interface traveling for higher Péclet number is much faster and finally reaches a value twice or three times larger than that at lower Péclet number.

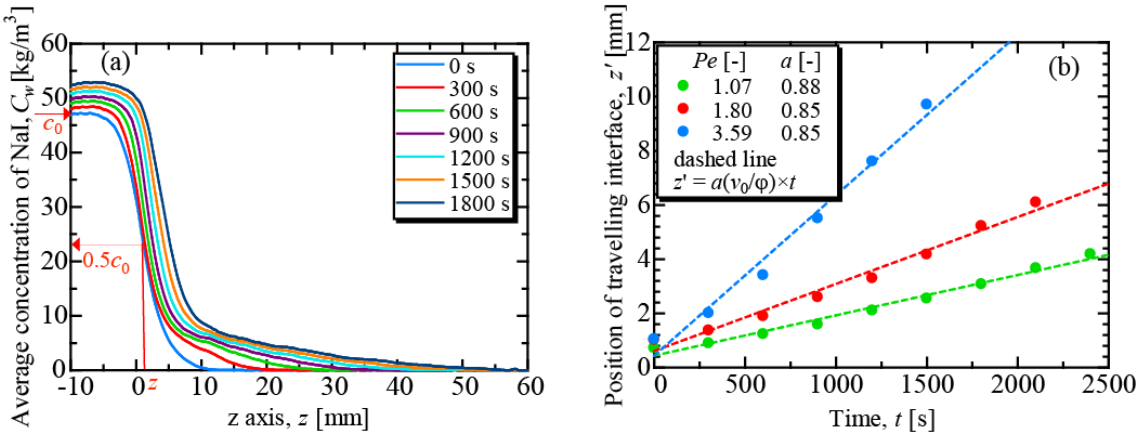

Fig. 5-9. (a) Slice-averaged concentration of NaI for different time steps at Pe = 1.80. (b) Effect of injection speed on the interface traveling vs. time.

5.5 Mixing layer

Neufeld et al. (2010) described dynamic regimes using numerical and two-dimensional experimental results. In this three-dimensional experimental study, the gravitational unstable convective flow can be divided into three regions: the downward-moving fingers, the upward-moving NaCl solution flow, and the mixing layer which is located below the MEG–NaI layer (the schematic of the flow regions are shown in Appendix Fig. A4). The upward-moving NaCl solution flowing with velocity v_U transforms the flow direction into downward-moving fingers having velocity v_D ($v_D = v$) in the mixing layer with a thickness of δ_m. Numerical simulation studies have depicted that nascent fingers are formed at the interface between MEG–NaI and NaCl solutions (Fu et al., 2013; Neufeld et al., 2010; Pau et al., 2010). Besides, the flow along the interface sweeps and merges the nascent fingers into descending ones.

To evaluate the thickness of the mixing layer roughly, I consider mass balance among the descending fingers, ascending NaCl solution flows, and the mixing layer:

$$A_D v_D \approx A_U v_U \approx v_m \delta_m \sum_{i=1}^{i=n} P_i \quad , \tag{5-1}$$

where A_D and A_U is the area of fingers and NaCl solution flows, respectively; v_m is the horizontal flow velocity in the mixing region, which is defined as the velocity when the flow sweeps along the interface and passes through the mixing layer horizontally; P_i is the perimeter of the fingers; and n is the number of fingers. The sum ΣP_i corresponds to the total length of the fingers and NaCl solution flows. The first term on the left-hand side denotes the mass flux of the downward fluids, the middle term denotes the mass flux of the upward fluids, and the right-hand side denotes the mass flux of the horizontal movement in mixing layer. From the horizontal cross-sectional CT images, which are binarized into a visualization of the fingers and NaCl solution flows, the perimeter of each finger, P_i, the area of descending fingers, A_D, and the area of upward NaCl solution flows, A_U, can be estimated. Assuming $v_m \approx v_U$, the thickness of the mixed layer, δ_m, can also be evaluated.

The thickness of the mixing layer δ_m was evaluated as 4.33, 3.91, and 4.20 mm for Péclet numbers of 1.07, 1.80, and 3.59, respectively. The estimated mixing-layer thickness is thin compared to the distance between the fingers (Fig. 5-5).

The mixing between the MEG-NaI and NaCl solutions is enhanced at the stagnation point, where upward moving fluid collides with the MEG-NaI layer, and in the shear layer, where the horizontal flow of NaCl solution drags the MEG-NaI layer down. As depicted in Fig. 5-5, the interface between the MEG-NaI and NaCl layers is deformed with the development of convection. The balance between the momentum force of the upward moving flows and gravitational force is expressed as

$$\frac{1}{2}\rho v_U^2 = \Delta\rho' g h_0 \quad , \tag{5-2}$$

where ρ is the density of the NaCl solution, $\Delta\rho'$ is the initial density difference between the MEG-NaI and NaCl solutions, and h is the deformation of the interface. The lifting up of the interface by the pushing action of the upward flow of the NaCl solution is estimated as $h_0 = 2.56 \times 10^{-9}$, 2.27×10^{-9} and 7.94×10^{-9} m for Péclet numbers of 1.07, 1.80, and 3.59, respectively, which is much lower than the particle diameter of the packed bed. This result suggests that the shape change of the interface is not attributable to the balance of forces, but rather to the localized mixing between MEG–NaI and NaCl solutions. The nonuniform distribution in mixing induces the interface deformation. Even if the interface shifts upward locally, it is observed to be several magnitudes smaller than the downward travelling distance of the interface. (Fig.5-9b).

5.6 Finger-number density

The finger number density is defined as the concentration of fingers on a horizontal image. The individual finger was computed from horizontal cross-sectional images. After applying noise removal and Gaussian filters, a local maximum in MEG-NaI concentration, which is 2% higher than the surroundings, is detected as a finger by the Local Maxima command in the image analysis software, Image J. The details of the method for detecting fingers are presented in section 3.4 and Appendix 2. The temporal evolution of the finger number density for each position along the *z*-axis is shown in Fig. 5-10. Immediately after injection, the maximum finger number density appeared near the initial interface. The fine fingers accumulated in a relatively small region and produced a sharp peak. Over time, the maximum finger number density decreased as the fingers extended downward while merging with neighboring fingers. The enhanced coalescence between fingers led to the range of the peak of the curve becoming flatter compared with that of comparable prior time steps.

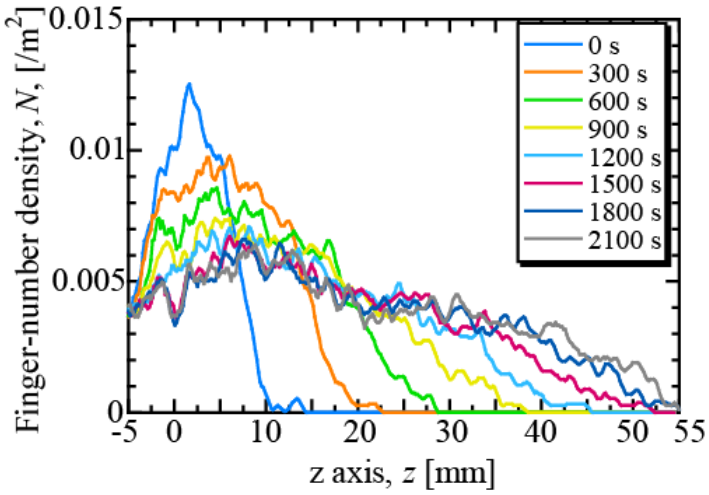

Fig. 5-10. Finger number density as a function of position along the z-axis for various time steps at *Pe* = 1.80 (Run # 3B).

The maximum finger number densities as a function of time for different Péclet numbers are summarized in Fig. 5-11a. The maximum finger number density decreased with time during the injection process for different Péclet numbers. With increasing Péclet number, the decay of the finger number density increased. Therefore, injection at a higher speed may result in an improvement in the transverse dispersion, which governs the progression of merging between fingers. Details of this occurrence will be discussed later.

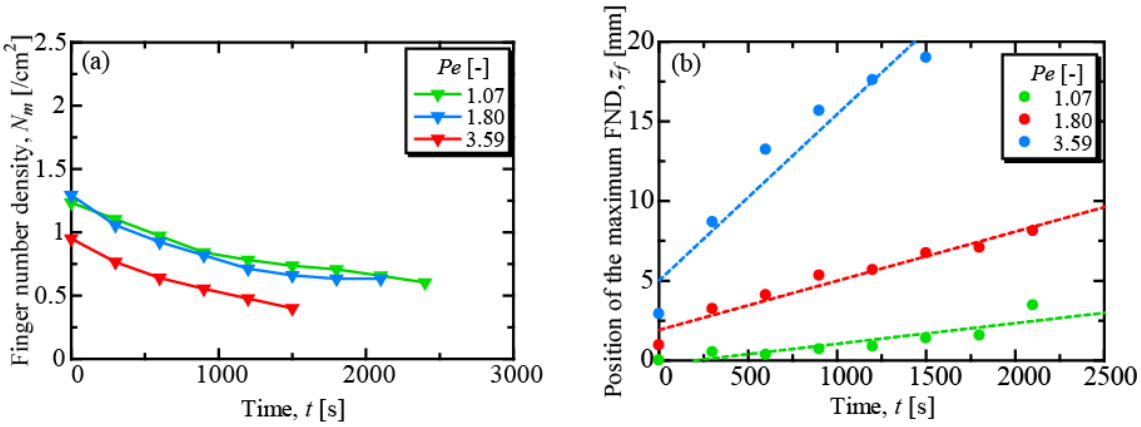

Fig. 5-11. Temporal evolution of (a) maximum finger number density N_m and (b) position of maximum finger number density z_f in a porous medium with average particle diameter of 975 µm. Each color represents a different injection speed.

We observed from Fig. 5-11b that with the development of fingers, the position of the maximum of finger number density (z_f) shifted downward along the z-axis for different Péclet numbers and significantly increased with time under higher injection speed. For higher injection speed, the downward movement of fingers was very pronounced with a faster extension velocity, which is consistent with the result in Fig. 5-4. The fastest progression was observed for the highest Péclet number, most likely because of the increase in the density difference between the fingers and surroundings by vertical displacement and enhanced lateral movement, leading to merging with nearest neighbors.

From Fig. 5-10 and Fig. 5-11, it is apparent that the finger number density monotonically decreases with time at the experimental scale. For a larger scale under reservoir conditions, after CO_2 injection into an oil reservoir, gravitational fingers extend downward and expand laterally. With the progress of time and vertical extension, the finger number density decreases and the finger diameter increases. Fingers spread to a larger field and finally reach an equilibrium state where no density difference appears between the fingers and surroundings and no flow occurs.

5.7 Mixing length

Thomas et al.(2016) investigated the effect of chemical reactions on the mixing length of fingers generated by the dissolution of CO_2 in water and in various alkaline solutions in a Hele–Shaw cell. They reported that the mixing length increases with time and has a larger value in CsOH solutions. Manickam and Homsy (1994) discussed the growth of

the mixing length of viscous fingering in miscible displacement flows in two-dimensional porous media. They defined forward and reverse mixing lengths to characterize the growth of the mixing zone in the direction of fluid penetration and in the reverse direction and reported that both the forward and reverse mixing lengths grew linearly with time. In this study, the mixing length was computed as the length of the most advanced finger growing from the interface. First, the position of the interface between the MEG–NaI and NaCl solutions was defined on the image for each experiment at t = 0 s, as indicated by the red horizontal line in Fig. 5-6. Then, the position of the tip of the longest fingers was computed from the concentration distribution in the finger by finding the position at which the concentration was smaller than 0.2 kg/m^3. For each time, the mixing length l_m was computed as the distance between this position and that of the initial interface.

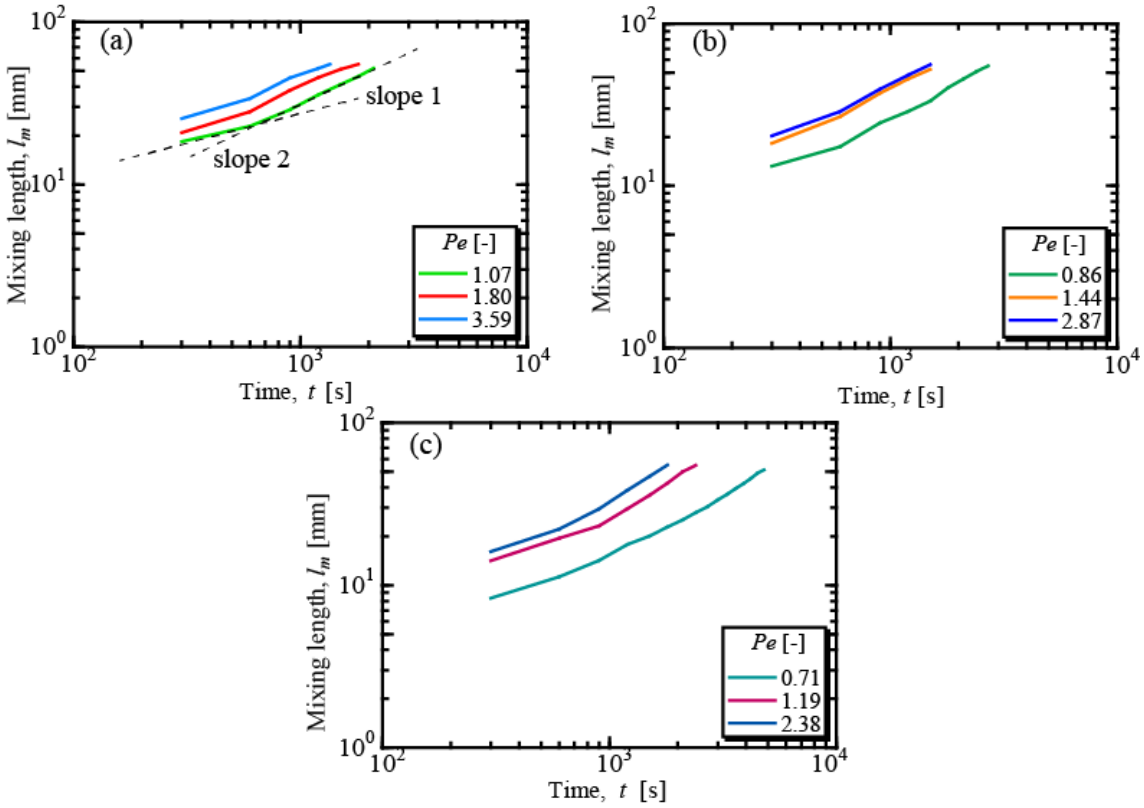

Fig. 5-12. Change of mixing length for different Péclet numbers as a function of time.

A log–log plot of the temporal evolution of l_m for different Péclet numbers is presented in Fig. 5-12. Upon dissolution of MEG–NaI in the NaCl solution, a thin denser layer developed below the interface, and slight fluctuations appeared and grew into downward-moving fingers. The formation of fingers sinking from the interface accelerated the penetration of mixed MEG–NaI with the NaCl solution, and l_m then increased faster until

the end of the experiment. The mixing length of fingers for higher Péclet number was larger than that for lower Péclet number at a given time. For the higher Péclet number case, the fingers developed faster than that in the other cases. For example, in Fig. 5-12a, the fastest evolution was observed for *Pe* = 3.59, where the final mixing length of the fingers was up to 17 mm larger than that for *Pe* = 1.07 at t = 1350 s. As observed in Fig. 5-12, there was a turning point of each curve for different Péclet numbers. The change of the mixing length was characterized by a lower slope at early times and a higher slope at later times.

Ghesmat et al. (2011) conducted two-dimensional numerical simulations of CO_2 dissolution in brine. They distinguished three different zones for mixing length variation for *Ra* = 500 and 1000. The mixing length changed with a smaller slope associated with $t^{0.5}$ in zone 1, and faster growth appeared in zone 2. Then, the mixing length changes became quicker, corresponding to strong convection. Farajzadeh et al. (2007) performed experiments and numerical simulations to investigate the mass transfer of density-driven natural convection. The results indicated that the progress of the tip position of the most advanced finger changed from square-root to linear behavior. Riaz et al. (2006) performed numerical simulations to analyze the long-term evolution of the finger density using linear stability theory. They reported that the front of the fastest finger initially moved proportional to $t^{0.5}$ and then switched to linear growth for large times at *Ra* = 500. Wooding (1969) investigated the growth of fingers at an unstable free interface with Rayleigh–Taylor instability in a Hele–Shaw cell and suggested that fingers grow approximately as a function of t^2 at early time, followed by growth proportional to *t*. Bacri et al. (1991) treated the growth of viscous fingers using an acoustic technique and profile analysis. They noted that a crossover occurred between a diffusive regime with $t^{0.5}$ growth and a convective regime with *t* growth.

Based on previous studies, it was assumed that the mixing length was proportional to time with coefficients of *m* and *n* as $l_m = mt^n$. The coefficients *m* and *n* at all Péclet numbers are listed in Table 5-3. At early times, on average, $l_m \propto t^{0.45\pm0.13}$, $r^2 = 0.98$ and at later times, $l_m \propto t^{0.74\pm0.16}, r^2 = 0.98$. Immediately after injection, the fingers formed because of the density increase by mixing and then started to extend downward. Therefore, the mixing length changed with a smaller slope in the early stage. With the progress of injection, the enhanced mixing near the interface was strong enough at longer times to result in a larger finger extension velocity and a larger velocity of upward-moving flows. These large velocities resulted in the nonlinear interaction of fingers, faster growth of the fingers, and

faster growth of the mixing length. However, in these three-dimensional experiments, the transverse dispersion had a significant effect on the fingering during the injection process. The fingers not only extended downward but also expanded along the radial direction of the fingers, which was perpendicular to the gravitational direction. The mixing length grew proportional to $t^{0.74}$ at later times, which is smaller than the t growth of previous studies.

Table 5-3. Slopes in Fig. 5-12.

Particle diameter	Péclet number	Slope 1		Slope 2	
d_p [μm]	Pe [-]	m	n	m	n
	0.71	0.49	0.49	0.05	0.81
647	1.19	1.10	0.45	0.05	0.90
	2.38	1.18	0.46	0.09	0.86
	0.86	1.35	0.40	0.12	0.78
780	1.44	0.82	0.55	0.28	0.72
	2.87	1.18	0.50	0.30	0.72
	1.07	3.03	0.32	0.32	0.68
975	1.80	1.80	0.43	0.54	0.60
	3.59	2.45	0.41	0.86	0.60

5.8 Evolution of the relative volume V of the mixing fingers

Kneafsey and Pruess (2010) and Thomas et al. (2015) computed the relative area of convective fingers in two-dimensional CO_2 convective dissolution. In the present study, the relative volume was defined as the ratio of the finger volume to the total cylindrical volume under the initial interface, which can be interpreted as an approximate measure of CO_2 mixing. A larger relative volume indicates a larger amount of CO_2 mixing with oil. For this measure, the CT images were binarized to black and white images by applying a certain threshold value, such that the fingers appeared black on a white background. The area of the fingers A(z) was calculated for each slice. Along the z-axis, the entire packed bed consisted of 496 slices. The black volume was calculated as $V = \int_0^z A(z)dz$, where z ranged from 0 to 55 mm; A(z) was equal to 0 for the white background and 1 for the black fingers.

The time evolution of the relative volume for different Péclet numbers is plotted in Fig. 5-13. The relative volume increased linearly with time for different Péclet numbers and increased with increasing Péclet number by increasing the injection speed. The distance

of the finger extension and interaction between fingers contributed to the increase of the relative volume of the fingers. With time, the fingers extended downward while spreading laterally because of the mixing between the downward-moving fingers and upward-moving flows.

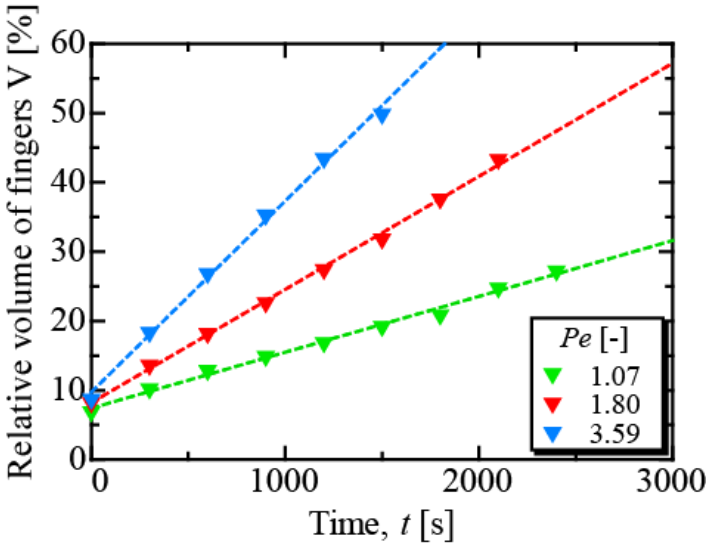

Fig. 5-13. Time evolution of relative volume V of mixing fingers in porous media with particle diameter of 975 μm. Each curve represents different injection speeds: Run # 3A (green), Run # 3B (blue), and Run # 3C (red).

The gradient of each curve was defined as the growth rate. The growth rate of the relative volume for higher Péclet number was larger than that for lower Péclet number. During the early stage of the injection, the relative volume of fingers was almost the same for the different Péclet numbers. As the mixing progressed, the evolution of the relative volume at higher Péclet number was much faster and reached a value twice as large as that for the lower Péclet number case in the later stage when the advanced fingers reached the bottom of the packed bed. The significant difference in the gradient for different Péclet numbers is most likely due to the dispersion, which was more pronounced under high Péclet number conditions. These observations agree well with the results presented in Fig. 5-3, where more fingers merged with nearest neighbors with a rapid extension velocity for gravitational downward flow.

Based on the results in Fig. 5-13, the growth rate (σ) could be estimated from the gradient of each curve. For all the experiments, the growth rate is plotted against the Péclet number in Fig. 5-14. The growth rate of the relative volume of the fingers is associated with the Péclet number following a power law relationship, $\sigma_V = 0.01 Pe^{0.94}$, $r^2 = 0.88$,

suggesting that the growth rate of the relative volume increases rapidly with increasing Péclet number. On one hand, with increasing Péclet number, the mixing near the initial interface becomes stronger, resulting in a larger finger extension velocity and velocity of upward-moving flows; therefore, the growth of the mixing length of fingers is faster. On the other hand, during the injection process, the fingers dominantly extend downward while coalescing with neighboring fingers. The enhanced interaction of fingers may have a significant effect on fingering development, which governs the merging of fingers with neighboring fingers, leading to increasing finger diameter. Therefore, for higher Péclet number, the area that the fingers occupy is enlarged, and the relative volume exhibits a rapid increase.

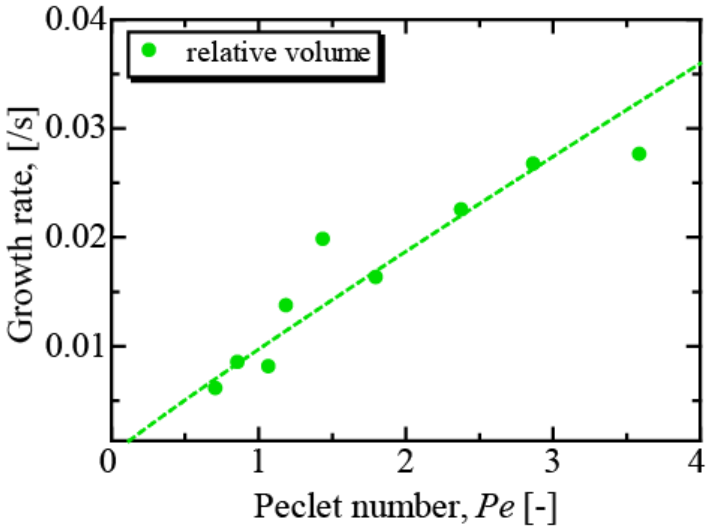

Fig. 5-14. Relationship between growth rate and Péclet number

5.9 Dispersion

As discussed above, the enhanced dispersion during the injection process affects the broadening of the fingers and reduces the finger number density. In this chapter, the transverse dispersion coefficient (D_T) in the shear flow between the downward-moving fingers and upward-moving NaCl solution was estimated from the concentration gradient of the fingers for each injection speed and permeability based on the method of mass conservation for a finger presented in Wang et al. (2016) and Nakanishi et al. (2016). Here, a new Péclet number (Pe^*) was defines as $Pe^* = (v d_p/\varphi D)$, where v is the finger extension velocity. In these experiments, Pe^* ranges from 7.1 to 40.8. The results for all the experiments are plotted against Pe^* as blue dots in Fig. 5-15. The results in this part,

evaluated in the shear flow during the injection process, showed good agreement with D_T previously presented in uniform flow (Bijeljic & Blunt, 2007; Sahimi, 2011) as well as shear flow in three-dimensional porous media (mentioned in section 3.5) (Wang et al., 2016). In these experiments, the finger extension was accelerated by the increased density difference from injection. The fingering structure is related to both downward extension and transverse dispersion.

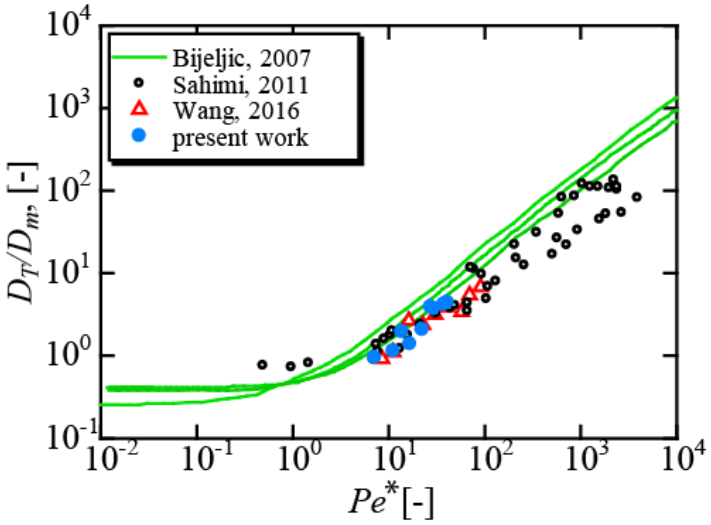

Fig. 5-15. Relationship between transverse dispersion and Pe^*. The black circles denote the experimental results for uniform flow (Sahimi, 2001), the lines are the results from pore-scale modeling (Bijeljic and Blunt, 2007), and the red triangles are 3D experimental results for shear flow (Wang et al., 2016).

From Fig. 5-15, it is clear that the transverse dispersion coefficient increases with increasing Pe^*. The transverse dispersion coefficient is related to Pe^* as $D_T/D_m = 0.13Pe^{*0.97}$, $r^2 = 0.90$. The more pronounced transverse dispersion at higher Pe^* enhances the merging of gravitational fingers and increases the decay of the finger number density. This phenomenon also explains the rapid increase of the relative volume of fingers at higher Péclet numbers.

5.10 Summary

The three-dimensional characteristics of fingering resulting from an increase in density during injection were investigated using X-ray CT. A fluid pair of MEG–NaI and NaCl solutions with nonlinear density property was used to model the density increase from

mixing upon CO_2 injection into an oil reservoir. Three particles with different average diameters and three injection speeds were used to vary the Péclet number in a range of 0.71–3.59. The effect of the Péclet number on the characteristics of gravitational fingering were investigated.

Immediately after injection, the density of the injected MEG–NaI solution was less than that of the NaCl solution. The density increase from the mixing resulted in unstable gravity drainage. During the injection process, the mixing near the interface was enhanced and fine fingers appeared at the interface and then grew into large fingers, which interacted and merged with neighboring fingers and extended vertically downward. With increasing of Péclet number, a larger density difference between the downward-moving fingers and upward-moving surroundings was observed at the root of the fingers, resulting in an increase of the finger extension velocity and velocity of upward flow. Furthermore, the mixing near the interface became stronger. In the fingers, the local NaI concentration decreased linearly and the initial interface traveled downward because of the enhanced dispersion resulting from the increase in the injection speed. Over time, the mixing length of the fingers and the relative volume of the fingers increased. The growth of the mixing length of the fingers was proportional to time with a smaller slope at early times and switched to a larger slope growth at later times. A rapid increase of the relative volume of the fingers occurred at higher Péclet number. The enhanced dispersion with increasing injection speed affected the broadening of the fingers and reduced the finger number density.

The findings based on three-dimensional displacement experiments describe the characteristics of gravitational fingering resulting from the density increase during the injection process. The experimental results indicate that the density increase from mixing of CO_2 and oil has a crucial effect on fingering development and recovery performance.

Chapter 6: Conclusions and outlook

6.1 Conclusions

The three-dimensional fingering structure of gravitationally unstable convective flows in a porous medium was investigated using a micro-focused X-ray CT scanner. In this work, the focus was to study the characteristics of density-driven mixing and fingering patterns relevant to CO_2 dissolution in aquifer and CO_2 enhanced oil recovery, and to quantify the effect of Rayleigh number and Péclet number on the fingering behaviors.

Experimentally, a novel miscible fluid pair of MEG–NaI and NaCl solutions with nonlinear density property was presented to model the density increase from mixing upon CO_2 injection into the deep saline formation or oil reservoir. MEG-NaI solution is less dense than the NaCl solution, however, with mixing, the density of the mixture increases and exceeds that of the NaCl solution, and the degree to which it exceeds that of NaCl solution depends on the fraction of MEG-NaI. In this manner, three fluid pairs were suitable for the three-dimensional observation of gravitational unstable convection in porous medium using X-ray CT. Four different plastic particles with the average diameter in a range of 647 μm to 1410 μm were packed in a cylinder with a diameter of 70 mm as a porous media for varying the permeability and porosity related to Rayleigh number and Péclet number.

In this study, three parts of experiments were performed. According to the results of each part, conclusions can be drawn as following:

For the part the density-driven natural convection between MEG-NaI and NaCl solutions, nine experimental runs were conducted for the combination of three fluids pairs and three particle diameters in a Rayleigh number range between 2600 and 16000. The characteristics of fingering and the effect of the transverse dispersion on finger structure were investigated.

With the dissolution of MEG-NaI solution into NaCl solution, the density of the mixture increased, leading to a gravitational unstable layer at the initial interface. Slight fluctuations that appeared on the interface grew into large fingers, which interacted and merged with neighboring fingers. The fingers extended vertically downward without changing their locations, forming a columnar structure. The finger-extension velocity increased in line with the Rayleigh number and correlated with the characteristic velocity at a coefficient of 0.35.

The three-dimensional images provided the local concentration of NaI in fingers for each unit time, therefore, the transverse dispersion coefficient can be estimated. The experimental results demonstrated that transverse dispersion was enhanced as the strength of density-driven natural convection increased. The decrease in figure-number density was related to the Rayleigh number and also affected by transverse dispersion. For all Rayleigh number cases, the finger-number density decreased with time and was in an exponential relationship with the transverse dispersion coefficient. The strength of transverse dispersion between the downward and upward flow regions significantly affected the decay of the finger-number density because of the interaction and merging of fingers. The dimensionless mass flux, i.e., the Sherwood number, correlated with the Rayleigh number in a power-law relationship.

For the part the density-driven natural convection in a layered heterogeneous porous medium, the plastic particle with three different average diameter has been packed stratified as a heterogeneous porous medium. Two fluid pairs were used to perform the density-driven natural convection. The effect of the heterogeneity on fingering structure, finger-extension velocity and the concentration distribution in fingers were discussed.

In the heterogeneous layered structure, when convective fingers pass through the interface to a higher permeability layer, the finger-extension velocity increases and the diameter of fingers decreases. The enhanced dispersion between downward fingers and upward flow regions leads to a decreasing of concentration in fingers. On the other hand, when fingers pass through the interface to a lower permeability layer, the finger-extension velocity decreases. The weakened dispersion has a limited influence on the distribution of concentration in fingers, thus, the concentration in fingers remains the same and the diameter of the fingers increases. These results suggest that the concentration in the finger changes nonlinearly against the permeability.

The layered heterogeneous structure hinders the development of natural convection. In the heterogeneous layered structure, as finger passing through the high permeability layer, finger-extension velocity is reduced by a dilution of finger concentration. Therefore, the development of natural convection in the layered heterogeneous structure becomes slower than that in the homogeneous structure.

For the part of gravitational fingering due to density increase by mixing during injection process, the fluid pair B was used to model the density increase from mixing upon CO_2 injection into an oil reservoir. Three particles with different average diameters and three

injection speeds were used to vary the Péclet number in a range of 0.71–3.59. The effect of the Péclet number on the characteristics of gravitational fingering were investigated.

As the injection progresses, the density increase from the mixing resulted in unstable gravity drainage. During the injection process, the mixing near the interface was enhanced and fine fingers appeared at the interface and then grew into large fingers, which interacted and merged with neighboring fingers and extended vertically downward. With increasing Péclet number, a larger density difference between the downward-moving fingers and upward-moving surroundings was observed at the root of the fingers, resulting in an increase of the finger extension velocity and velocity of upward flow. Furthermore, the mixing near the interface became stronger.

In the fingers, the local NaI concentration decreased linearly and the initial interface travelled downward because of the enhanced dispersion resulting from the increase in the injection speed. Over time, the mixing length of the fingers and the relative volume of the fingers increased. The growth of the mixing length of the fingers was proportional to time with a smaller slope at early times and switched to a larger slope growth at later times. A rapid increase of the relative volume of the fingers occurred at higher Péclet number. The enhanced dispersion with increasing injection speed affected the broadening of the fingers and reduced the finger number density.

The findings based on three-dimensional experiments describe the characteristics of gravitational fingering resulting from the density increase. The results of natural convection provide new insights, elucidating the extension velocity of CO_2 fingers and the amount of CO_2 migration after injection into deep saline formation, which may contribute to the large-scale implementation of CO_2 storage and the evaluation of long-term security.The experimental results of the displacement indicate that the density increase from mixing of CO_2 and oil has a crucial effect on fingering development and recovery performance.

6.2 Outlook

The findings attained in this work on laboratory experiments can be take into account for estimation of the time of natural convection in reservoir and the amount of CO_2 dissolved in deep saline aquifers, which contribute to the larger-scale implementation of CO_2 storage and evaluation of long-term security. It also provides the basic data for defining a budget of the CO_2 injection project.

In terms of CO_2 sequestration, after injection, CO_2 will move upward because of the buoyancy. During the upward-moving process, CO_2 can be trapped at the relative small pore spaces as a separated phase by capillary force, which is called capillary trapping. However, the details about how the capillary trapping occurs, what is the effect of trapped CO_2 bubbles on upward-moving CO_2, and how does the capillary trapping interact with solubility trapping, are still not clear and need to do further study.

In this work, although the effect of heterogeneity of the porous media on fingering behaviors was presented, it was limited in simplify model and only focused on fingering structure, finger extension velocity, and concentration distribution in fingers. A comprehensive research is required for presenting the characteristics of CO_2 fingers in heterogeneous reservoir during convective mixing process.

After CO_2 injection process is stopped, it is very important to confirm and detect that if the CO_2 has been stored safely without any potential risk of leakage. The monitoring of stored CO_2 is crucial to estimate the long-term security of CO_2 geological storage. Since the migration of injected CO_2 is very slow and might be continued for several hundred years, how long the monitoring should be performed necessarily, how much it will cost and who will pay for it, become the major problems before performing the stored CO_2 monitoring. To this end, it is necessary to carry out some preliminary studies to make clear the implementation period and the cost.

Monitoring can occur near surface wellbores to see if injected CO_2 coming up from below, and also occur in the subsurface by using a seismic method. In reservoir, the groundwater flows depending on the movement of dissolved CO_2, therefore, streaming potential phenomena occurs. In terms of the seismic method, the monitoring of stored CO_2 can be achieved by measuring the potential difference at the surface or seabed. However, it is costly and inaccurate. In order to perform the monitoring in a low cost and high accuracy way, some numerical simulation works performed in measuring streaming potential by setting a measurement equipment in the injection well could be the further step in the future. Therefore, the CO_2 saturation, the velocity field of the ground water and the distribution of streaming current can be obtained by measuring the streaming current. Then, the CO_2 flowing behaviors in reservoir can be figured out.

References

Ahmed, T., Nasrabadi, H., & Firoozabadi, A. (2012). Complex flow and composition path in CO 2 injection schemes from density effects. *Energy and Fuels*, 26(7), 4590–4598. https://doi.org/10.1021/ef300502f

Alam, M. M., Hjuler, M. L., Christensen, H. F., & Fabricius, I. L. (2014). Petrophysical and rock-mechanics effects of CO_2 injection for enhanced oil recovery: Experimental study on chalk from South Arne field, North Sea. *Journal of Petroleum Science and Engineering*, 122, 468–487. https://doi.org/10.1016/j.petrol.2014.08.008

Arts, R., Chadwick, A., Eiken, O., Thibeau, S., & Nooner, S. (2008). Ten years' experience of monitoring CO_2 injection in the Utsira Sand at Sleipner offshore Norway. *First Break*, 26(1), 65–72.

Bachu, S. (2003). Screening and ranking of sedimentary basins for sequestration of CO_2 in geological media in response to climate change. *Environmental Geology*, 44(3), 277–289. https://doi.org/10.1007/s00254-003-0762-9

Backhaus, S., Turitsyn, K., & Ecke, R. E. (2011). Convective instability and mass transport of diffusion layers in a Hele-Shaw geometry. *Physical Review Letters*, 106(10), 1–4. https://doi.org/10.1103/PhysRevLett.106.104501

Bacri, J.-C., Salin, D., & Woumeni, R. (1991). Three-Dimensional Miscible Viscous Fingering in Porous Media, 67(15), 2005–2008.

Bandara, U. C., Tartakovsky, A. M., & Palmer, B. J. (2011). Pore-scale study of capillary trapping mechanism during CO_2 injection in geological formations. *International Journal of Greenhouse Gas Control*, 5(6), 1566–1577. https://doi.org/10.1016/j.ijggc.2011.08.014

Bangia, V. K., Yau, F. F., & Hendricks, G. R. (1993). Reservoir Performance of a Gravity-Stable, Vertical CO_2 Miscible Flood: Wolfcamp Reef Reservoir, Wellman Unit. *Spere*, 8(4), 261–269. https://doi.org/10.2118/22898-PA

Bayat, M., Lashkarbolooki, M., Hezave, A. Z., & Ayatollahi, S. (2016). Investigation of gas injection flooding performance as enhanced oil recovery method. *Journal of Natural Gas Science and Engineering*, *29*, 37–45. https://doi.org/10.1016/j.jngse.2015.12.047

Benson, S., Gale, J., R, I. E. A. G. G., Programme, D., Puyvelde, D. Van, Wright, B.,

Tinto, R. (2008). Geological Storage of Carbon Dioxide.

Bijeljic, B., & Blunt, M. J. (2007). Pore-scale modeling of transverse dispersion in porous media. *Water Resources Research*, 43(12), 1–8. https://doi.org/10.1029/2006WR005700

Bon, J., Emera, M. K., & Sarma, H. K. (2006). An Experimental Study and Genetic Algorithm (GA) Correlation to Explore the Effect of nC5 on Impure CO_2 Minimum Miscibility Pressure (MMP). *SPE Journal*, SPE101036.

Bon, J., & Sarma, H. (2005). An Investigation of Minimum Miscibility Pressure for CO_2-Rich Injection Gases with Pentanes-Plus Fraction. *SPE International Improved Oil Recovery Conference*, SPE97536.

Cardenas, R. L., Alston, R. B., Nute, A. J., & Kokolis, G. P. (1984). Laboratory design of a gravity-stable miscible CO_2 process. *Journal of Petroleum Technology*, 36(January), 2–9. https://doi.org/10.2118/10270-PA

Chaudhary, K., Bayani Cardenas, M., Wolfe, W. W., Maisano, J. A., Ketcham, R. A., & Bennett, P. C. (2013). Pore-scale trapping of supercritical CO_2 and the role of grain wettability and shape. *Geophysical Research Letters*, 40(15), 3878–3882. https://doi.org/10.1002/grl.50658

Chevalier, S., Faisal, T. F., Bernabe, Y., Juanes, R., & Sassi, M. (2015). Numerical sensitivity analysis of density driven CO_2 convection with respect to different modeling and boundary conditions. *Heat and Mass Transfer/Waerme- Und Stoffuebertragung*, 51(7), 941–952. https://doi.org/10.1007/s00231-014-1466-2

Chuoke, R. L., van Meurs, P., & van der Poel, C. (1959). The instability of slow, immiscible, viscous liquid-liquid displacements in permeable media. *Petroleum Transactions, AIME*, 216, 188–194. https://doi.org/SPE-1141-G

Cooper, C. A., Crews, J. B., Schumer, R., Breitmeyer, R. J., Voepel, H., & Decker, D. L. (2014). Experimental Investigation of Transient Thermal Convection in Porous Media. *Transport in Porous Media*, 104(2), 335–347. https://doi.org/10.1007/s11242-014-0337-0

Cross, M. C., & Hohenberg, P. C. (1993). Pattern formation outside of equilibrium. *Reviews of Modern Physics*, 65(3), 851–1112. https://doi.org/10.1103/RevModPhys.65.851

Ehyaei, D., & Kiger, K. T. (2014). Quantitative velocity measurement in thin-gap Poiseuille flows. *Experiments in Fluids*, 55(4). https://doi.org/10.1007/s00348-014-

1706-8

Emami-Meybodi, H., Hassanzadeh, H., Green, C. P., & Ennis-King, J. (2015). Convective dissolution of CO_2 in saline aquifers: Progress in modeling and experiments. *International Journal of Greenhouse Gas Control*, 40, 238–266. https://doi.org/10.1016/j.ijggc.2015.04.003

Ennis-King, J., & Paterson, L. (2005). Role of convective mixing in the long-term storage of carbon dioxide in deep saline formations. *Spe Journal*, 10, 349–356. https://doi.org/10.2118/84344-pa

Faisal, T. F., Chevalier, S., Bernabe, Y., Juanes, R., & Sassi, M. (2015). Quantitative and qualitative study of density driven CO_2 mass transfer in a vertical Hele-Shaw cell. *International Journal of Heat and Mass Transfer*, 81, 901–914. https://doi.org/10.1016/j.ijheatmasstransfer.2014.11.017

Faisal, T. F., Chevalier, S., & Sassi, M. (2013). Experimental and numerical studies of density driven natural convection in saturated porous media with application to CO_2 geological storage. *Energy Procedia*, 37, 5323–5330. https://doi.org/10.1016/j.egypro.2013.06.450

Farajzadeh, R. (2009.). Enhanced transport phenomena in CO_2 sequestration and CO_2 EOR.

Farajzadeh, R., Salimi, H., Zitha, P. L. J., & Bruining, H. (2007). Numerical simulation of density-driven natural convection in porous media with application for CO_2 injection projects. *International Journal of Heat and Mass Transfer*, 50 (25–26), 5054–5064. https://doi.org/10.1016/j.ijheatmasstransfer.2007.08.019

Firrozabadi, A., & Cheng, P. (2010). Prospects for subsurface CO_2 sequestration. *AIChE Journal*, 56, 1398–1405. https://doi.org/10.1002/aic

Fu, X., Cueto-Felgueroso, L., & Juanes, R. (2013). Pattern formation and coarsening dynamics in three-dimensional convective mixing in porous media. *Philosophical Transactions. Series A, Mathematical, Physical, and Engineering Sciences*, 371(2004), 20120355. https://doi.org/10.1098/rsta.2012.0355

Gaus, I. (2010). Role and impact of CO_2-rock interactions during CO_2 storage in sedimentary rocks. *International Journal of Greenhouse Gas Control*, 4(1), 73–89. https://doi.org/10.1016/j.ijggc.2009.09.015

Ghesmat, K., Hassanzadeh, H., & Abedi, J. (2011). The Effect of anisotropic dispersion on the convective mixing in long-term CO_2 Storage in Saline Aquifers. *AIChE*

Journal, 57(3), 561–570. https://doi.org/10.1002/aic

Gilfillan, S. M. V., Lollar, B. S., Holland, G., Blagburn, D., Stevens, S., Schoell, M., Ballentine, C. J. (2009). Solubility trapping in formation water as dominant CO_2 sink in natural gas fields. *Nature*, 458(7238), 614–618. https://doi.org/10.1038/nature07852

Global CCS Institute. (2011). *The global status of CCS: 2011*. https://doi.org/978-0-9944115-2-5

Gong, Y., & Gu, Y. (2015). Miscible CO_2 simultaneous water-and-gas (CO_2 -SWAG) injection in the Bakken formation. *Energy & Fuels*, 29(9), 5655–5665. https://doi.org/10.1021/acs.energyfuels.5b01182

Gopalakrishnan, S. S., Carballido-Landeira, J., De Wit, A., & Knaepen, B. (2017). Relative role of convective and diffusive mixing in the miscible Rayleigh-Taylor instability in porous media. *Physical Review Fluids*, 2(1), 12501. https://doi.org/10.1103/PhysRevFluids.2.012501

Gozalpour, F., Ren, S. R., & Tohidi, B. (2005). CO_2 EOR and storage in oil reservoirs. *Oil and Gas Science and Technology*, 60(3), 537–546. https://doi.org/10.2516/ogst:2005036

Graf, F., Meiburg, E., Haertel, C. (2002). Density-driven instabilities of miscible fluids in a Hele-Shaw cell: linear stability analysis of the three-dimensional Stokes equations, *Journal of Fluid Mechanics*, 451, 261–282. https://doi.org/10.1017/S002211200100651

Grigg, R. (1995). Dynamic phase composition, density, and viscosity measurements during CO_2 displacement of reservoir oil. *SPE International Symposium on Oilfield Chemistry*.

Hassanzadeh, H., Pooladi-Darvish M., & Keith D. W. (2007). Scaling behavior of convective mixing, with appplication to geological storage of CO_2. *AIChE Journal*, 53(5), 1121-1131. https://doi.10.1002/aic.11157.

Heller, J. P. (1966). Onset of instability patterns between miscible fluids in porous media. *Journal of Applied Physics*, 37(4), 1566–1579. https://doi.org/10.1063/1.1708569

Hesse, M. A. (2008). Mathematical modeling and multiscale simulation of CO_2 storage in saline aquifers. *Doctoral dissertation,Stanford University*, (May).

Hewitt, D. R., Neufeld, J. A., & Lister, J. R. (2012). Ultimate regime of high Rayleigh

number convection in a porous medium. *Physical Review Letters*, 108(22), 879–895. https://doi.org/10.1103/PhysRevLett.108.224503

Hewitt, D. R., Neufeld, J. A., & Lister, J. R. (2013). Convective shutdown in a porous medium at high Rayleigh number. *Journal of Fluid Mechanics*, 719, 551–586. https://doi.org/10.1017/jfm.2013.23

Hewitt, D. R., Neufeld, J. A., & Lister, J. R. (2014). high Rayleigh number convection in a three-dimensional porous medium. *Physical Review Letters*, 748, 879–895. https://doi.org/10.1103/PhysRevLett.108.224503

Hidalgo, J. J., & Carrera, J. (2009). Effect of dispersion on the onset of convection during CO_2 sequestration. *Journal of Fluid Mechanics*, 640, 441. https://doi.org/10.1017/S0022112009991480

Hidalgo, J. J., Fe, J., Cueto-Felgueroso, L., & Juanes, R. (2012). Scaling of convective mixing in porous media. *Physical Review Letters*, 109(26), 1–5. https://doi.org/10.1103/PhysRevLett.109.264503

Hoteit, H. (2009). Numerical modeling of diffusion in fractured media for gas injection and recycling schemes. *SPE Annual Technical Conference and*, (June), 1–15. https://doi.org/10.2118/103292-ms

Huppert, H. E., & Neufeld, J. A. (2014). The Fluid Mechanics of Carbon Dioxide Sequestration. *Annual Review of Fluid Mechanics*, 46(1), 255–272. https://doi.org/10.1146/annurev-fluid-011212-140627

Huppert, H. E., Turner, J. S., Carey, S. N., Sparks, R. S. J., & Hallworth, M. A. (1986). A laboratory simulation of pyroclastic flows down slopes. *Journal of Volcanology and Geothermal Research*, 30, 179–199.

Hussen, C., Amin, R., Madden, G., & Evans, B. (2012). Reservoir simulation for enhanced gas recovery: An economic evaluation. *Journal of Natural Gas Science and Engineering*, 5, 42–50. https://doi.org/10.1016/j.jngse.2012.01.010

Iglauer, S. (2011). Dissolution Trapping of Carbon Dioxide in Reservoir Formation Brine A Carbon Storage Mechanism. *Mass Transfer - Advanced Aspects*, 836. https://doi.org/10.5772/20206

Intergovernmental Panel on Climate Change. (2005). IPCC, 2005: IPCC special report on carbon dioxide capture and storage.

International Energy Agency. (2010). World Energy Outlook 2009. https://doi.org/10.1049/ep.1977.0180

International Energy Agency. (2014). Energy Technology Perspectives 2014 Energy Technology Perspectives 2014 Harnessing Electricity's Potential Explore the data behind ETP. https://doi.org/10.1787/energy_tech-2010-en

Jadhawar, P. S., & Sarma, H. K. (2010). Numerical simulation and sensitivity analysis of gas-oil gravity drainage process of enhanced oil recovery. *Journal of Canadian Petroleum Technology*, 49(2), 64–70. https://doi.org/10.2118/133373-PA

Jensen, M. D., Pei, P., Snyder, A. C., Heebink, L. V., Botnen, L. S., Gorecki, C. D., Harju, J. A. (2013). Methodology for phased development of a hypothetical pipeline network for CO_2 transport during carbon capture, utilization, and storage. *Energy and Fuels*, 27(8), 4175–4182. https://doi.org/10.1021/ef302042p

Jiang, F., & Tsuji, T. (2016). Numerical investigations on the effect of initial state CO_2 topology on capillary trapping efficiency. *International Journal of Greenhouse Gas Control*, 49, 179–191. https://doi.org/10.1016/j.ijggc.2016.03.006

Johannsen, K., Oswald, S., Held, R., & Kinzelbach, W. (2006). Numerical simulation of three-dimensional saltwater-freshwater fingering instabilities observed in a porous medium. *Advances in Water Resources*, 29(11), 1690–1704. https://doi.org/10.1016/j.advwatres.2005.12.008

Ju, B., Fan, T., & Jiang, Z. (2013). Modeling asphaltene precipitation and flow behavior in the processes of CO_2 flood for enhanced oil recovery. *Journal of Petroleum Science and Engineering*, 109, 144–154. https://doi.org/10.1016/j.petrol.2013.08.029

Karimnezhad, M., Jalalifar, H., & Kamari, M. (2014). Investigation of caprock integrity for CO_2 sequestration in an oil reservoir using a numerical method. *Journal of Natural Gas Science and Engineering*, 21, 1127–1137. https://doi.org/10.1016/j.jngse.2014.10.031

Klein, E., De Lucia, M., Kempka, T., & Kühn, M. (2013). Evaluation of long-term mineral trapping at the Ketzin pilot site for CO_2 storage: An integrative approach using geochemical modelling and reservoir simulation. *International Journal of Greenhouse Gas Control*, 19, 720–730. https://doi.org/10.1016/j.ijggc.2013.05.014

Kneafsey, T. J., & Pruess, K. (2010). Laboratory flow experiments for visualizing carbon dioxide-induced, density-driven brine convection. *Transport in Porous Media*, 82(1), 123–139. https://doi.org/10.1007/s11242-009-9482-2

Kolditz, O., Ratke, R., Diersch, H. J. G., & Zielke, W. (1998). Coupled groundwater

flow and transport: 1. Verification of variable density flow and transport models. *Advances in Water Resources*, 21(1), 27–46. https://doi.org/10.1016/S0309-1708(96)00034-6

Lansangan, R. M., & Smith, J. L. (1993). Viscosity, Density, and Composition Measurements of CO_2/West Texas Oil Systems. *SPE Reservoir Engineering*, 8(3), 175–182. https://doi.org/10.2118/21017-PA

Lashkarbolooki, M., Vaezian, A., Hezave, A. Z., Ayatollahi, S., & Riazi, M. (2016). Experimental investigation of the influence of supercritical carbon dioxide and supercritical nitrogen injection on tertiary live-oil recovery. *Journal of Supercritical Fluids*, *117*, 260–269. https://doi.org/10.1016/j.supflu.2016.07.004

Lei, H., Yang, S., Zu, L., Wang, Z., & Li, Y. (2016). Oil Recovery Performance and CO_2 Storage Potential of CO_2 Water-Alternating-Gas Injection after Continuous CO_2 Injection in a Multilayer Formation. *Energy and Fuels*, 30(11), 8922–8931. https://doi.org/10.1021/acs.energyfuels.6b01307

Li, Y., Wu, P., Xia, Z., Yang, Q., Flores, G., Jiang, H., … Yu, B. (2014). Changes in residual air saturation after thorough drainage processes in an air-water fine sandy medium. *Journal of Hydrology*, 519(PA), 271–283. https://doi.org/10.1016/j.jhydrol.2014.07.019

Li, Z., & Firoozabadi, A. (2009). Modeling and simulation of the polymeric nanocapsule formation process. *IFAC Proceedings Volumes (IFAC-PapersOnline)*, *7*(PART 1), 405–410. https://doi.org/10.1002/aic

Lindeberg, E., & Begmo, P. (2003). The long-term fate of CO_2 injected into an aquifer. *Greenhouse Gas Control Technologies*, 1, 489–494.

Lindeberg, E., & Wessel-Berg, D. (1997). Vertical convection in an aquifer column under a gas cap of CO_2. *Energy Conversion and Management*, 38, S229–S234. https://doi.org/10.1016/S0196-8904(96)00274-9

MacMinn, C. W., Neufeld, J. A., Hesse, M. A., & Huppert, H. E. (2012). Spreading and convective dissolution of carbon dioxide in vertically confined, horizontal aquifers. *Water Resources Research*, 48(11), 1–11. https://doi.org/10.1029/2012WR012286

Manickam, O., & Homsy, G. (1994). Simulation of viscous fingering in miscible displacements with nonmonotonic viscosity profiles. *Physics of Fluids*, 1356, 95–107. https://doi.org/10.1063/1.868049

Moore, J. S. (1986). Design Installation and Early Operation of the Timbalier Bay S-2B

(RA) SU Gravity-Stable Miscible CO_2-Injection Project. *SPE Production Engineering*, *1* (5)(SPE 14287), 369–378.

Nakanishi, Y., Hyodo, A., Wang, L., & Suekane, T. (2016). Experimental study of 3D Rayleigh-Taylor convection between miscible fluids in a porous medium. *Advances in Water Resources*, 97, 224–232. https://doi.org/10.1016/j.advwatres.2016.09.015

Neufeld, J. A., Hesse, M. A., Riaz, A., Hallworth, M. A., Tchelepi, H. A., & Huppert, H. E. (2010). Convective dissolution of carbon dioxide in saline aquifers. *Geophysical Research Letters*, 37(22), 2–6. https://doi.org/10.1029/2010GL044728

Nordbotten, J. M., Celia, M. A., & Bachu, S. (2005). Injection and storage of CO_2 in deep saline aquifers: Analytical solution for CO_2 plume evolution during injection. *Transport in Porous Media*, 58(3), 339–360. https://doi.org/10.1007/s11242-004-0670-9

Olea, R. A. (2015). CO_2 retention values in enhanced oil recovery. *Journal of Petroleum Science and Engineering*, 129, 23–28. https://doi.org/10.1016/j.petrol.2015.03.012

Ouakad, H. M. (2013). Modeling the CO_2 sequestration convection problem using the lattice Boltzmann method. *Mathematical Problems in Engineering*, *2013*. https://doi.org/10.1155/2013/846854

Palmer, F. S., Nute, A. J., & Peterson, R. L. (1984). Implementation of a Gravity-Stable Miscible CO_2 Flood in the 8000 Food Sand, Bay St. Elaine Field. *J. Pet. Techol.*, 36(January), 101–110.

Pau, G. S. H., Bell, J. B., Pruess, K., Almgren, A. S., Lijewski, M. J., & Zhang, K. (2010). High-resolution simulation and characterization of density-driven flow in CO_2 storage in saline aquifers. *Advances in Water Resources*, 33(4), 443–455. https://doi.org/10.1016/j.advwatres.2010.01.009

Pentland, C. H., El-Maghraby, R., Iglauer, S., & Blunt, M. J. (2011). Measurements of the capillary trapping of super-critical carbon dioxide in Berea sandstone. *Geophysical Research Letters*, 38(6), 2007–2010. https://doi.org/10.1029/2011GL046683

Pope, G. A. (2011). Recent Developments and Remaining Challenges of Enhanced Oil Recovery. *Journal of Petroleum Technology*, (July), 65–68.

https://doi.org/10.2118/0711-0065-JPT

Rao, D. N., Ayirala, S. C., Kulkarni, M. M., & Sharma, A. P. (2004). Development of gas assisted gravity drainage (GAGD) process for improved light oil recovery. *SPE Fourteenth Symposium on Improved Oil Recovery*. https://doi.org/10.2523/89357-MS

Riaz, A., & Cinar, Y. (2014). Carbon dioxide sequestration in saline formations: Part I-Review of the modeling of solubility trapping. *Journal of Petroleum Science and Engineering*, 124, 367–380. https://doi.org/10.1016/j.petrol.2014.07.024

Riaz, A., Hesse, M., Tchelept, H. A., & Orr, F. M. (2006). Onset of convection in a gravitationally unstable diffusive boundary layer in porous media. *Journal of Fluid Mechanics*, 548, 87–111. https://doi.org/10.1017/S0022112005007494

Ruith, M., & Meiburg, E. (2000). Miscible rectilinear displacements with gravity override. Part 1. Homogeneous porous medium. *Journal of Fluid Mechanics*, 420, 225–257. https://doi.org/10.1017/S0022112000001543

Saffman, P. ., Taylor, S. G., & F.R.S. (1958). The penetration of a fluid into a porous medium or Hele-Shaw cell containing a more viscous liquid. *Proc. Royal Soc. London A*, 245, 312–329.

Sahimi, M. (2011), Dispersion in flow through porous media, in Flow and Transport in Porous Media and Fractured Rock, Wiley-VCH, pp.341-413, Weinheim Germany.

Shahraeeni, E., Moortgat, J., & Firoozabadi, A. (2015). High-resolution finite element methods for 3D simulation of compositionally triggered instabilities in porous media. *Computational Geosciences*, 19(4), 899–920. https://doi.org/10.1007/s10596-015-9501-z

Sharp, D. H. (1984). An overview of Rayleigh-Taylor instability. *Physica D*, 12, 3–18. https://doi.org/10.1016/0167-2789(84)90510-4

Slim, A. C., Bandi, M. M., Miller, J. C., & Mahadevan, L. (2013). Dissolution-driven convection in a Hele – Shaw cell , and some implications for CO_2 sequestration. *Phys. Fluids*, 24101, 1–20. https://doi.org/10.1063/1.4790511

Suekane, T., Nobuso, T., Hirai, S., & Kiyota, M. (2008). Geological storage of carbon dioxide by residual gas and solubility trapping. *International Journal of Greenhouse Gas Control*, 2(1), 58–64. https://doi.org/10.1016/S1750-5836(07)00096-5

Taku Ide, S., Jessen, K., & Orr, F. M. (2007). Storage of CO_2 in saline aquifers: Effects of gravity, viscous, and capillary forces on amount and timing of trapping. *International Journal of Greenhouse Gas Control*, 1(4), 481–491. https://doi.org/10.1016/S1750-5836(07)00091-6

Thomas, C., Lemaigre, L., Zalts, A., D'Onofrio, A., & De Wit, A. (2015). Experimental study of CO_2 convective dissolution: The effect of color indicators. *International Journal of Greenhouse Gas Control*, 42, 525–533. https://doi.org/10.1016/j.ijggc.2015.09.002

Thomas, C., Loodts, V., Rongy, L., & De Wit, A. (2016). Convective dissolution of CO_2 in reactive alkaline solutions: Active role of spectator ions. *International Journal of Greenhouse Gas Control*, 53, 230–242. https://doi.org/10.1016/j.ijggc.2016.07.034

Touvet, T., Balmforth, N. J., Craster, R. V., & Sutherland, B. R. (2011). Fingering instability in buoyancy-driven fluid-filled cracks. *Journal of Fluid Mechanics*, 672, 60–77. https://doi.org/10.1017/S0022112010005860

Wang, J. H., & Kennedy, I. W. (1950). Self-diffusion coefficients of sodium ion and iodide ion in aqueous sodium iodide solutions. *J. Am. Chem. Soc.*, 72(5), 2080–2083.

Wang, L., Nakanishi, Y., Hyodo, A., & Suekane, T. (2016). Three-dimensional structure of natural convection in a porous medium: Effect of dispersion on finger structure. *International Journal of Greenhouse Gas Control*, 53, 274–283. https://doi.org/10.1016/j.ijggc.2016.08.018

Wang, L., Nakanishi, Y., Teston A. D., & Suekane, T. (2018). Effect of diffusing layer thickness on the density-driven natural convection of miscible fluids in porous media: Modeling of mass transport. *Journal of Fluid Science and Technology*, 13(1). https://doi. 10.1299/jfst.2018jfst000x.

Wo, S., Yin, P., Blakeney-DeJarnett, B., & Mullen, C. (2008). Simulation Evaluation of Gravity Stable CO_2 Flooding in the Muddy Reservoir at Grieve Field, Wyoming. *SPE Symposium on Improved Oil Recovery*, SPE 113482. https://doi.org/10.2118/113482-MS

Wooding, R. a. (1969). Growth of fingers at an unstable diffusing interface in a porous medium or Hele-Shaw cell. *Journal of Fluid Mechanics*, *39*(3), 477–495. https://doi.org/10.1017/S002211206900228X

Xie, Y., Simmons, C. T., & Werner, A. D. (2011). Speed of free convective fingering in porous media. *Water Resources Research*, 47(11), 1–16. https://doi.org/10.1029/2011WR010555

Xu, R., Li, R., He, D., & Jiang, P. (2017). E ff ect of Mineral Dissolution/Precipitation and CO_2 Exsolution on CO_2 transport in Geological Carbon Storage. *Acc. Chem. Res.*, 50, 2056–2066. https://doi.org/10.1021/acs.accounts.6b00651

Xu, X., Chen, S., & Zhang, D. (2006). Convective stability analysis of the long-term storage of carbon dioxide in deep saline aquifers. *Advances in Water Resources*, 29(3), 397–407. https://doi.org/10.1007/s11432-006-0397-z

Yang, C., & Gu, Y. (2006). Accelerated mass transfer of CO_2 in reservoir brine due to density-driven natural convection at high pressures and elevated temperatures. *Industrial and Engineering Chemistry Research*, 45(8), 2430–2436. https://doi.org/10.1021/ie050497r

Zhang, H., Hou, D., & Li, K. (2015). An Improved CO_2-Crude Oil Minimum Miscibility Pressure Correlation. *Journal of Chemistry*, *2015*, 1–10. https://doi.org/10.1155/2015/175940

Zheng, S., Li, H., & Yang, D. (2013). Pressure maintenance and improving oil recovery with immiscible CO_2 injection in thin heavy oil reservoirs. *Journal of Petroleum Science and Engineering*, 112, 139–152. https://doi.org/10.1016/j.petrol.2013.10.020

Acknowledgements

First of all, I would like to thank my supervisor Prof. Suekane Tetsuya. He helps me so much both on academic and life in Japan through the entire Ph. D period. When I just been Japan and with poor Japanese communication skills, he kindly arranged a Japanese student picked me up from the Narida airport to the dormitory. At the same time, he was waiting for me with some lab mates at the Suzukakedai station with beddings because the shopping mall nearby was closed at that late time. It was an unforgettable start of the life in Japan. My Japanese improved a lot from the daily conversation with him because of his patient listening and slow speaking.

Under his supervision and guidance, my research headed the correct direction and went smoothly. The topic, originalities, and method were all from the fruitful discussion with Prof. Suekane. Thanks to the frequently discussion, I was into my research deeper and deeper, step by step. He encouraged me to join in the academic conference held in Japan and overseas, and offered me the chance to learn the skills how to introduce my research to others in a comprehensible way, and to enlarge my horizon. More important thing I learned from Prof. Suekane is how to think logically. To predict, detect and define a problem, and find a way to solve it, is the essential of being a qualified researcher.

Beyond a supervisor, Prof. Suekane showed me the way to enjoy life. Do not just focus on research, but also focus on the wonderful surroundings. He introduced us some beautiful places to visit and traditional food to taste, and even guided us some hiking routes at the weekend, which was a good way to know more about Japan and enjoy my research.

I also would like to thank Prof. Okamura Tetsuji and Prof. Okuno Yoshihiro. Many thanks for your comments on my research and the help for my job-hunting. The time spend with you at the Nomikai and the barbeque party will be the good memories.

Dr. Jiang Lanlan, Mr. Saito Yusuke, and Mr. Ando Sinnosuke gave a lot of help when I just came to Japan. Their considerate introduction and experiment experience helped me to join Suekane lab and to know the new research field at a very short time.

Many thanks to Mr. Hyodo Akimitsu and Mr. Nakanishi Yuji, the two lab mates who do the research related to mine. During the two and half years, with their help, I was familiar with the software Image J to process the data. We always discussed about the experimental method and results, which help me a lot to progress the research.

The one and half year spent with Mr. Sakai Shigeki, Mr. Nagai Yuta, Mr. Nakano Ryouta, and Mr. Kawarada Takao was full of joy. Thank for teaching me Japanese in a light-hearted way. “圧倒的成長”becomes popular in Suekane lab that we cheer each other up by saying it.

The help from Mr. Egami Masahiro, Mr. Minokawa Kosuke, Mr. Ono J, and Mr. Higuchi Fukunaga, who are the job-hunting fellows, also be great appreciated. With their help, I learned how to write an email and other documents in a correct Japanese style. They suggested me how to show my potential in an interview, which helped me to find a job in Japan finally. I will never forget the time we enjoying barbeque party together and your facial expression when you were on the roller coaster.

The Chinese girls, Ms. Liu Yao, Ms. Huang Yaxiao, are easy-going. The time spend with them, walking in the campus, doing the lucky draw ice-cream game, and having boxed lunch, make the research life relaxing. Thanks for your tolerance to my complaints at the time when I was upset. Ms. Cai Shitong and Ms. Ran Zixin, the little sisters who share happiness and upset with me. They always remind me the days when I was the same age as them.

I am grateful to Mr. Patmonoaji Anindityo and Mr. Mushilin Muharrik. They increased the diversity of dishes in barbeque party and hotpot party. I also would like to thank Mr. Tsuji Kento, Mr. Fujiura Shori, Mr. Sin Sotheavuth, Mr. Wang Weicen, Mr. Gao Qian, Mr. Muhammad Narsir, and Ms. Thamsiriprideeporn Chanakarn. Although a short time spend with you, it is still hard to say goodbye.

Last, I would like to thank my parents, for the unceasing encouragement, support and attention. Thank you for reducing the frequency of video calls because you worried about the effect on this dissertation writing. I will be grateful forever for your love. Additionally, I owe thanks to my husband Mr. Gong Bo for his love and care. I could never be brave enough to start a new life in Japan without you. Because of your sense of humor, optimism, and childish curiosity, the life is full of sunshine.

Appendix

1. Experimental setup

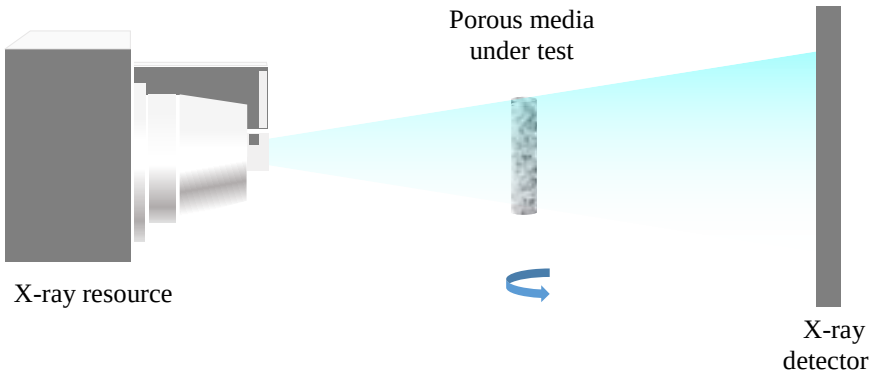

Figure A1. Experimental setup

Experiment apparatus are connected as shown in Fig. A1. The experiments are performed under the statics mode of the CT scanner, that is, the porous medium under observation rotates for 360 ° during scanning, while the x-ray source and detector are still. High positional reproducibility in the three-dimensional images could be achieved.

2. Finger number density

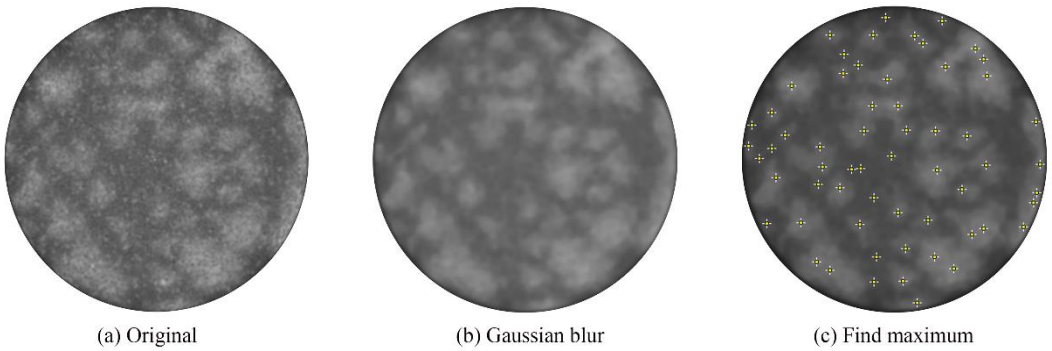

Figure A2. Sequences in process to detect a finger in horizontal cross-sectional images. From (a) original CT image, after removing noise, (b) a Gaussian blur filter is applied, and (c) the peak of concentration is then detected as fingers, denoted with the cross symbols.

The finger-number density was computed from horizontal cross-sectional images by the following procedure: first, high-concentration pixels with a radius lower than a certain value (dependent on the specific particles) are removed from the images as noise

associated with the impurity of the packed particles (Fig. A2a). Then, a Gaussian blur filter is applied to the images (Fig. A2b). Finally, a local maximum in MEG-NaI concentration, which is 2% higher than the surroundings, is detected as a finger (Fig. A2c) by the Local Maxima command in the image analysis software, Image J.

3. Mass transfer rate

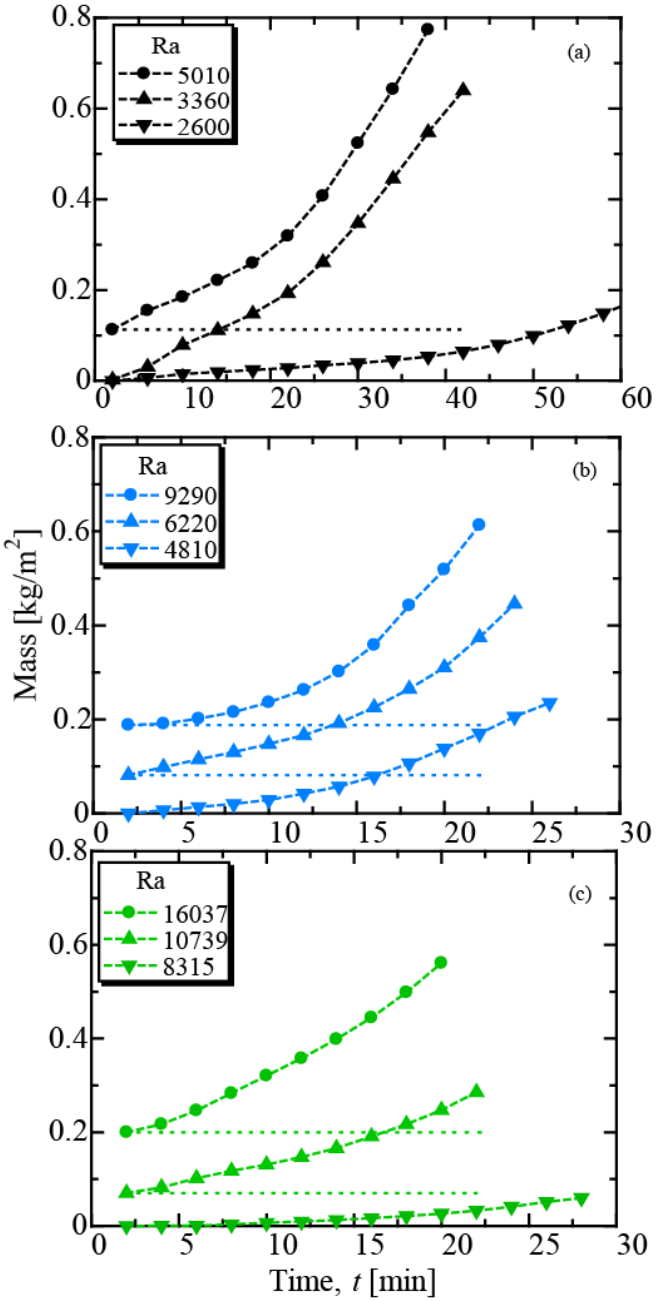

Figure A3. The change in mass of NaI per unit area for the porous medium of (a) d_p = 780 μm, k = 2.63 × 10^{-10} m^2; (b) d_p = 975 μm, k = 4.87 × 10^{-10} m^2; and (c) d_p = 1410 μm, k = 8.24 × 10^{-10} m^2.

To estimate the mass transfer rate, a cylindrical region is created in the porous medium as a control volume where the NaCl solution initially locates. Based on the local concentration of NaI, the mass of NaI in the bottom cylindrical regions has been evaluated for each time step as shown in Fig. A3. Over time, the observable increase in mass tends to be large and constant. From the change in the mass, the mass flux F is estimated for each Rayleigh number. The maximum mass flux is observed for the porous medium with permeability $k = 2.63 \times 10^{-10}$ m^2 (Fig. A3a) and $k = 4.87 \times 10^{-10}$ m^2 (Fig. A3b) when the fingers reach the bottom surface of the porous medium, because after that point the intensity of the convection is slowed down. In the case of the porous medium with permeability $k = 8.24 \times 10^{-10}$ m^2 (Fig. A3c), the mass flux does not show a clear peak until the interface between MEG-NaI and NaCl solutions collapses. Therefore, for reference, the mass flux is estimated using the time the fingers reach the bottom surface of the porous medium.

4. The schematic of the flow regions of gravitational unstable convective flows

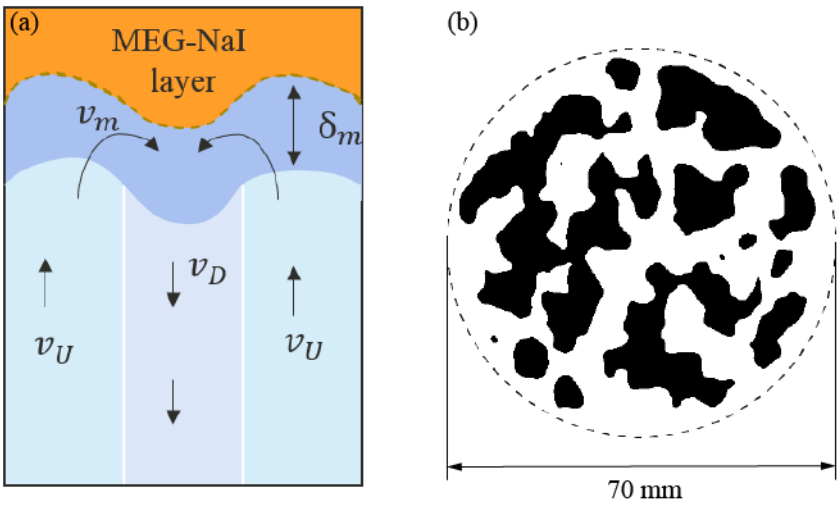

Figure A4. (a) Sketch of three regions of the gravitational unstable convective flow: the descending fingers, ascending NaCl solution flow, and the mixing layer that lies below the MEG-NaI layer. (b) Horizontal cross-sectional image binarized into a visualization of fingers (black) and NaCl (white) (*Pe* =1.80, Run # 3B).